

Spectroscopic investigation of defects and their impact on the physical properties of transition-metal-oxide heterostructures

Von der Fakultät für Mathematik und Physik der Universität Stuttgart zur
Erlangung der Würde eines Doktors der Naturwissenschaften (Dr. rer. nat.)
genehmigte Abhandlung

Vorgelegt von
Gideok Kim
aus Incheon, Korea

Hauptberichter: Prof. Dr. Bernhard Keimer

Mitberichter: Prof. Dr. Harald Giessen

Prüfungsvorsitzende: Prof. Dr. Maria Daghofer

Tag der mündlichen Prüfung: 22.05.2020

Universität Stuttgart
Max-Planck-Institut für Festkörperforschung

2020

ABSTRACT

In this thesis, we present the synthesis of complex metal-oxide heterostructures with carefully tuned chemical composition via oxide molecular beam epitaxy and reactive sputtering. The physical properties of the heterostructures were investigated using various spectroscopic techniques such as confocal Raman spectroscopy, spectroscopic ellipsometry, polarized neutron reflectometry (PNR), X-ray magnetic circular dichroism (XMCD), and X-ray absorption spectroscopy (XAS) in combination with standard characterizations.

In oxide heterostructures, it has been a challenge to determine the presence of defects with atomically small sizes, e.g. atomic vacancies and interstitial atoms, and the significance of such defects for the interpretation of physical phenomena has hence been under intense discussion. The majority of studies on the topic has concentrated on structural and microscopic properties to determine the concentration of defects, which has been difficult due to their small spatial extent and low concentration. We discovered that spectroscopic techniques, especially Raman spectroscopy, are highly sensitive to such defects, and we studied several cases: oxygen vacancies in $\text{La}_{2-x}\text{Sr}_x\text{CuO}_4$ thin films, and ruthenium vacancies in Sr_2RuO_4 and SrRuO_3 thin films. In all systems, we identified defect-related Raman signals, where the atomic defects change the local lattice structure and allow more Raman-active modes

due to the reduced local symmetry. These modes show strong correlations with macroscopic properties such as magnetization and resistivity. It turned out that the new peaks are present even in samples that exhibit excellent structures from X-ray diffractometry and electron microscopy, which suggests that Raman spectroscopy is extremely sensitive to the local disturbances.

Oxide heterostructures exhibit unique magnetic phenomena owing to various types of electronic correlation, which can be tuned by the distribution of defects. Here we studied two magnetic phenomena that are crucial to magnetism-based devices: exchange bias in cuprate/manganate superlattices and the anomalous Hall effect in SrRuO₃ thin films. We controlled the concentration and the distribution of defects in the heterostructures, and modified the magnetic properties. We discovered perpendicular exchange bias in cuprate/manganate interfaces, and elucidated the influence of interfacial magnetic interactions and charge transfer on this effect. In SrRuO₃ thin films, we clarified the origin of anomalies in the Hall effect as a hallmark of inhomogeneous ferromagnetism due to ruthenium vacancies.

In oxides with Ruddlesden-Popper structures (A_{n+1}B_nO_{3n+1}), the partial substitution of A-site cations with aliovalent cations is a popular method to tune the population of the valence electrons while leaving the average BO₆ network undisturbed. However, the influence of local lattice distortions generated by the dopant-host radii mismatch (DHRM) on the macroscopic phase behavior of chemically doped compounds has been a matter of significant debate. In particular, the role of the DHRM in suppressing superconductivity in highly overdoped copper oxide superconductors has recently been intensely discussed. In order to minimize the DHRM, we epitaxially stabilized Ca-doped La₂CuO₄ films over a wide concentration range. Because of the limited solubility of Ca in the bulk, the properties of this system had not been investigated before. Our La_{2-x}Ca_xCuO₄ thin films show a largely extended doping-range for superconductivity, consistent with theoretical predictions in the framework of the Hubbard model, and with the previously reported persistence of magnetic correlations that are presumed to mediate Cooper pairing in the cuprates. The results highlight the importance of the DHRM in determining the physical properties of metal-oxide compounds.

ZUSAMMENFASSUNG

Diese Dissertation beschreibt die Synthese von Heterostrukturen komplexer Metalloxide mit sorgfältig justierter chemischer Zusammensetzung mittels Oxid-Molekularstrahlepitaxie und reaktivem Sputtern. Die physikalischen Eigenschaften dieser Heterostrukturen wurden durch spektroskopische Techniken (wie z.B. konfokale Raman-Spektroskopie, spektroskopische Ellipsometrie, Röntgen-Zirkulardichroismus und Röntgen-Absorptionsspektroskopie) bestimmt, in Verbindung mit Standard-Charakterisierungsmethoden.

In Oxid-Heterostrukturen war es bisher eine besondere Herausforderung, Defekte mit atomaren Dimensionen (wie z.B. atomare Fehlstellen und Atome auf Zwischenpositionen des Kristallgitters) zu detektieren, und der Einfluss solcher Defekte auf die physikalischen Eigenschaften wurde daher intensiv diskutiert. Die Mehrheit der Untersuchungen zu diesem Thema verwendete strukturelle und mikroskopische Eigenschaften zur Bestimmung der Defekt-Konzentration, stieß dabei jedoch wegen der geringen räumlichen Ausdehnung und niedrigen Konzentration der Defekte an Grenzen. Unsere Untersuchungen ergaben, dass spektroskopische Techniken – insbesondere die Raman-Spektroskopie – solche Defekte mit hoher Empfindlichkeit nachweisen können. In diesem Zusammenhang untersuchten wir mehrere Fälle: Sauerstoff-Fehlstellen in $\text{La}_{2-x}\text{Sr}_x\text{CuO}_4$ -Dünnschichten sowie Ruthenium-Fehlstellen in Sr_2RuO_4 - und SrRuO_3 -Filmen. In allen Systemen fanden wir

defektinduzierte Raman-Signale, die durch eine Verzerrung der lokalen Gitterstruktur verursacht werden. Die Defekte reduzieren die lokale Symmetrie des Kristallgitters und erzeugen auf diese Weise zusätzliche Raman-aktive Moden, welche eine starke Korrelation mit makroskopischen Eigenschaften (wie z.B. der Magnetisierung und dem elektrischen Widerstand) aufweisen. Dabei stellte sich heraus, dass solche Moden selbst in Proben zu finden sind, deren Struktureigenschaften anhand von Experimenten mit Röntgendiffraktometrie und Elektronenmikroskopie exzellent sind, was die Empfindlichkeit der Raman-Spektroskopie auf lokale Verzerrungen unterstreicht.

Oxid-Heterostrukturen zeigen aufgrund einer Vielfalt elektronischer Korrelationen einzigartige magnetische Eigenschaften, welche durch die Defektkonzentration durchstimmt werden können. Wir untersuchten zwei magnetische Phänomene von zentraler Bedeutung für magnetische Bauelemente: den sogenannten „Exchange Bias“-Effekt in Cuprat-Manganat-Übergittern sowie den anomalen Hall-Effekt in SrRuO_3 -Dünnschichten. Durch Kontrolle der Konzentration und der räumlichen Verteilung der Defekte gelang es uns, die magnetischen Eigenschaften gezielt zu verändern. Insbesondere entdeckten wir Exchange-Bias für Magnetfelder senkrecht zur Filmebene an Cuprat-Manganat-Grenzflächen und untersuchten den Einfluss von magnetischen Wechselwirkungen und Ladungstransfer an den Grenzflächen auf diesen Effekt. In SrRuO_3 -Dünnschichten ergaben unsere Untersuchungen, dass Ruthenium-Fehlstellen und der damit verbundene inhomogene Ferromagnetismus für Anomalien in dem Hall-Effekt solcher Proben verantwortlich sind.

In Oxiden mit Ruddlesden-Popper-Strukturen ($\text{A}_{n+1}\text{B}_n\text{O}_{3n+1}$) ist die partielle Substitution von A-Kationen eine herkömmliche Methode, um die Konzentration der Valenzelektronen zu durchstimmen, ohne die durchschnittliche Struktur des BO_6 -Netzwerk zu stören. Allerdings entstehen durch das Missverhältnis der Ionenradien der Substituenten und der Gitterionen (Dopant-Host Radii Mismatch, DHRM) lokale Gitterverzerrungen, deren Einfluss auf das makroskopische Phasenverhalten chemisch dotierter Verbindungen Anlass zu vielen Diskussionen gegeben hat. Insbesondere wurde die Rolle des DHRM bei der Verringerung der supraleitenden Übergangstemper-

atur in stark überdotierten Cupraten intensiv diskutiert. Um den DHRM zu minimieren, machten wir uns die epitaktische Stabilisierung Ca-dotierter La_2CuO_4 -Dünnschichten über einen weiten Bereich von Ca-Konzentrationen zunutze. Da die Löslichkeit von Ca in Volumenmaterialien begrenzt ist, konnten die Eigenschaften dieses Systems bisher nicht untersucht werden. Unsere $\text{La}_{2-x}\text{Ca}_x\text{CuO}_4$ -Filme zeigen einen stark vergrößerten Stabilitätsbereich für die Supraleitung, im Einklang mit theoretischen Vorhersagen im Rahmen des Hubbard-Modells und mit der zuvor experimentell festgestellten Fortdauer magnetischer Korrelationen, welche die Cooper-Paarbildung in den Cupraten vermutlich verursachen. Diese Ergebnisse bezeugen die wichtige Bedeutung des DHRM für die physikalischen Eigenschaften von Metalloxid-Verbindungen.

CONTENTS

1 Introduction & Overview	13
2 Transition metal oxides and metal-oxide heterostructures	17
2.1 Point defects	17
2.1.1 Hole doping La_2CuO_4 via aliovalent cation substitution	18
2.1.2 Oxygen vacancies in hole doped La_2CuO_4	19
2.1.3 Ruthenium vacancies in strontium ruthenates	20
2.2 Spectroscopic properties	22
2.2.1 Raman spectra of K_2NiF_4 type structures	22
2.2.2 Electronic structure of Sr_2RuO_4	24
2.2.3 Electronic structure of hole doped La_2CuO_4	25
2.2.4 Spectroscopic techniques	27
2.3 Synthesis of ruthenate thin films	28
2.3.1 Off-axis reactive sputtering	29
2.3.2 Synthesis of Sr-113 and Sr-214 thin films via dual target ablation	31
3 Point defects and spectroscopic responses	33
3.1 Selective formation of apical oxygen vacancies in $\text{La}_{2-x}\text{Sr}_x\text{CuO}_4$	34
3.1.1 Abstract	34

3.1.2	Introduction	34
3.1.3	Experimental methods	36
3.1.4	Results and discussion	37
3.1.5	Conclusion	44
3.2	Electronic and vibrational signatures of ruthenium vacancies in SRO thin films	45
3.2.1	Abstract	45
3.2.2	Introduction	45
3.2.3	Experimental details	48
3.2.4	Results and discussion	50
3.2.5	Conclusion	59
4	Tailoring magnetic properties via defect control	61
4.1	Tunable perpendicular exchange bias in oxide heterostructures	62
4.1.1	Abstract	62
4.1.2	Introduction	62
4.1.3	Experimental details	64
4.1.4	Results and discussion	67
4.1.5	Conclusion	74
4.2	Inhomogeneous ferromagnetism mimics signatures of the topological Hall effect in SrRuO ₃ films	75
4.2.1	Abstract	75
4.2.2	Main text	76
4.2.3	Methods	86
5	Overcoming the solubility limit via epitaxial stabilization	89
5.1	Persistent superconductivity in highly overdoped cuprates via minimizing the dopant-host radii mismatch	90
5.1.1	Abstract	90
5.1.2	Introduction	90
5.1.3	Results	93
5.1.4	Methods	98

INTRODUCTION & OVERVIEW

Point defects have long been known to be of central importance for the functionality of solids, and are gaining prominence in a wide spectrum of disciplines ranging from quantum technology to catalysis. In order to isolate individual defects and to understand their structure and electronic properties in a quantitative fashion, one needs to start from a host lattice that is as perfect as possible, and introduce the defects in a controlled manner. This requires a heroic effort even for elemental solids, as demonstrated by research on defect centers in diamond [CGT+06; VSR+14] or Pt surfaces [Ert08]. Complex metal oxides that comprise multiple atomic species exhibit fascinating physical properties in bulk form, including, for instance, high-temperature superconductivity and multiferroicity, but are susceptible to various types of defects. Yet very little is known about point defects in complex metal oxides, their electronic structure, and their influence on the bulk properties. During my doctoral studies, I aimed to make a contribution to the exploration of this largely unknown research field.

Several systems were studied during my doctoral work, namely cuprates that exhibit high temperature superconductivity, strontium ruthenates that host ferromagnetism and superconductivity, and cuprate/manganate super-

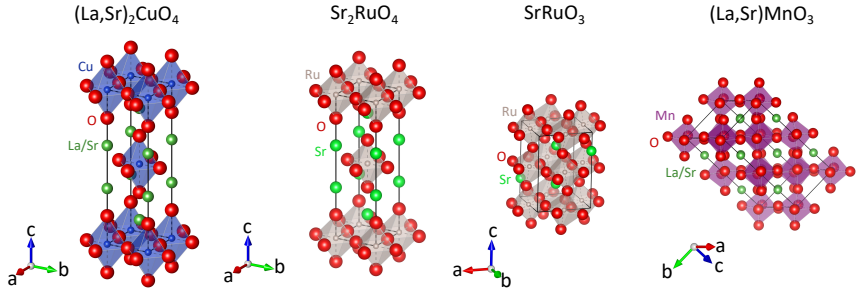


Figure 1.1: Lattice structure of the materials studied in the thesis. Black solid line indicates the boundary of the single unit cell.

lattices that show perpendicular exchange bias and charge transfer (Fig. 1.1). This thesis is focused on the synthesis of oxide heterostructures with various techniques. We used ozone-assisted molecular-beam epitaxy to synthesize thin films and superlattices that comprise cuprate and manganate layers. For conducting ruthenate thin films, we developed a reactive-sputtering chamber equipped with a Ru/Sr₂RuO₄ co-deposition setup to overcome the high volatility of RuO_x precursors and the high evaporation-temperature of Ru.

The thesis is written in a cumulative form based on five complete reports, therefore each section is a manuscript that has been either published or submitted to a journal. This presentation is preceded by **Chapter 2 - Concepts in solids**, where we elaborate fundamental concepts that are omitted in the manuscripts. Firstly, the chemistry of common point defects in oxides is reviewed, which is not widely considered in physics. We then summarize the fundamental aspects of vibrational and electronic properties of materials that are studied in the thesis. We close the chapter with a review of the dual-target reactive sputtering method that we developed to grow metallic ruthenate thin films.

The first step to obtain a perfect sample is to find out about possible imperfections. We therefore made an intense effort to find appropriate methods to measure point defects in oxide heterostructures, which is challenging

due to the small volume of nano-scale-thick samples. The results are summarized in **Chapter 3 - Point defects and spectroscopic responses**. This chapter contains two sections that show spectroscopic signatures of point defects such as oxygen vacancies and ruthenium vacancies in cuprates and ruthenates, respectively. We found that Raman spectroscopy combined with confocal microscopy is a powerful tool to characterize point defects in oxide thin films, because defects reduce the degree of local symmetry, and result in distinct peaks in the Raman spectra. Within the chapter, consequences of chemical modifications for the electronic structure were studied using various techniques that include X-ray absorption spectroscopy and electrical resistivity measurements.

A defect is not just an imperfection, but also a tuning parameter to obtain desirable physical properties. Especially magnetic properties of transition metal oxides can be controlled by the concentration of defects. We studied two such phenomena, namely the exchange bias and the anomalous Hall effect, and the results are presented in **Chapter 4 - Tailoring magnetic properties via defect control**. We discovered that perpendicular exchange bias exists in cuprate/manganate superlattices, and tuned the magnitude of this technologically important effect using atomic-layer-by-layer control of cations exploiting the magnetic phase diagram of $\text{La}_{2-x}\text{Sr}_x\text{CuO}_4$. In order to understand the origin of the perpendicular exchange bias, the magnetic structure at the interface was investigated using X-ray magnetic circular dichroism, polarized neutron reflectometry, and SQUID magnetometry. Another prominent phenomenon, the anomalous Hall effect in SrRuO_3 , is receiving great attention due to the recent discovery of unusual features in Hall resistivity curves, which suggested the presence of topological defects called skyrmions. We scrutinized the anomalies in the Hall resistivity curves of SrRuO_3 thin films, and clarified the relation between the distribution of Ru vacancies in the sample and the seemingly novel Hall signal based on comprehensive examinations of magnetic inhomogeneity.

Layer-by-layer deposition enables the synthesis of phases that do not exist in bulk samples. This phenomenon is called epitaxial stabilization, which has been routinely used to overcome the solubility limit of dopants in semi-

conductors. In doped La_2CuO_4 , the impact of doping-induced disorder on superconductivity has been controversial, and recent attention to the overdoped regime stimulated studies on the impact of cation-induced disorder. The dopant-host radii mismatch (DHRM) is at the center of this debate, because the local distortions caused by substitutional defects are considered to be particularly important for the physical properties in the overdoped regime. In **Chapter 5 - Overcoming the solubility limit via epitaxial stabilization**, we studied the effect of the reduced DHRM on the phase diagram of highly overdoped cuprate superconductors via adopting Ca as a dopant instead of Sr, which was inaccessible due to the solubility limit. We demonstrated that the lattice and electronic structures of the Ca doped La_2CuO_4 films evolve systematically upon doping until $x = 0.5$. The investigation of the superconducting properties revealed an extended stability range of superconductivity, highlighting the importance of the DHRM for the phase behavior and physical properties of the cuprates.

CHAPTER
2

TRANSITION METAL OXIDES AND METAL-OXIDE HETEROSTRUCTURES

2.1 Point defects

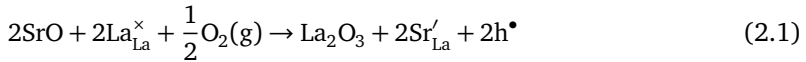
A defect is a deviation from the ideal crystal structure or chemical composition of a solid. A point defect is a defect with the dimensions of an atom such as substituted ions, interstitial atoms, and oxygen vacancies, which can be used to tune the materials properties as well. For instance, aliovalent cation substitution is a common way to adjust the carrier concentration of transition metal oxides, and modification of the oxygen stoichiometry is widely used for the same purpose in copper oxide superconductors such as $\text{La}_2\text{CuO}_{4+\delta}$ and $\text{YBa}_2\text{Cu}_3\text{O}_{7-\delta}$. Within this section we will discuss three types of point defects in the context of specific materials that are investigated in this thesis: the aliovalent cations and the oxygen nonstoichiometry in cation substituted La_2CuO_4 (LCO), and the metal vacancy in ternary ruthenium oxides. Here

we review point defects in the framework of defect chemistry, and their influence on the electrical transport properties.

2.1.1 Hole doping La_2CuO_4 via aliovalent cation substitution

Doping is a concept adopted from semiconductor physics, where the conducting carriers are introduced by chemical impurities. Therefore, it normally refers to situations where carriers are added to semiconducting parent compounds via chemical means. The doping concentration of semiconductors is usually limited to small values, $< 5 \times 10^{20} \text{ cm}^{-3}$, however the flexible valence states of many transition metal oxides allow the aliovalent substitution until complete replacement of the original atoms, provided that the structure remains stable.

One of the most important examples is cation-substituted LCO, which exhibits rich physical phenomena upon hole doping such as high temperature superconductivity, the pseudogap and spin-density waves. In order to introduce holes to a compound, cations with lower valence states are substituted for the original cations. In LCO, trivalent La^{3+} ions are replaced by bivalent ions of alkaline earth metals such Ca^{2+} , Sr^{2+} , and Ba^{2+} leaving the Cu sites intact. As a representative case, the reaction for the chemical substitution of Sr in LCO can be written as follows [MP91]:



Here, we used the Kröger-Vink notation for imperfections in crystals [KV56]. According to the equation, one Sr substitution (Sr'_{La}) results in a free hole to the system (h^{\bullet}), which is valid when the concentration of dopants is moderate. The straightforward cation chemistry has been used to derive the hole concentration (p) following a simple relation, $p = x$.

Stoichiometric LCO is a Mott insulator with a band gap of ~ 2 eV. Upon hole doping, $\text{La}_{2-x}\text{Sr}_x\text{CuO}_4$ (LSCO) becomes a metal above $x=0.06$, and exhibits high-temperature superconductivity with a maximum superconducting transition temperature (T_c) of 40 K at $x=0.16$. In case of LCO, the

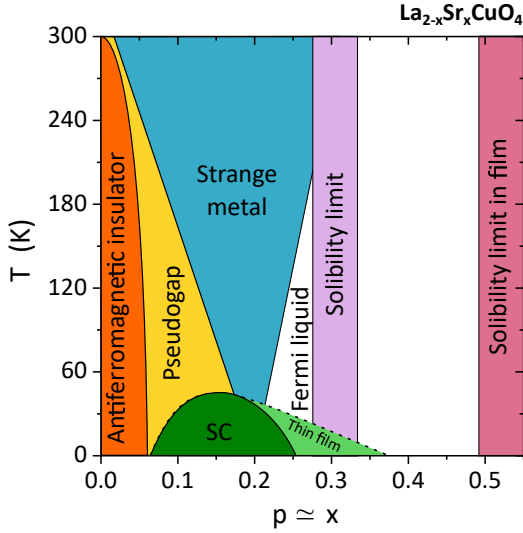


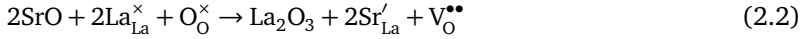
Figure 2.1: Schematic phase diagram of $\text{La}_{2-x}\text{Sr}_x\text{CuO}_4$.

dopant concentration is limited to lower values than in many other transition metal oxides: the reported solubility limits of Ca, Sr, and Ba in bulk samples are 0.12, 0.24, and 0.16, respectively, and a competing reaction emerges approaching the solubility limit [MSX+92; TYM+94]. Epitaxial stabilization is one of the methods to overcome the limited solubility, where the structure is clamped by epitaxial constraints from substrates. This technique is routinely used in the field of oxide heterostructures and also for LSCO thin films to grow samples with an extended doping range [GSGK02; LSB07].

2.1.2 Oxygen vacancies in hole doped La_2CuO_4

As demonstrated in equation (2.1), hole doping via cation substitution is essentially an oxidation, therefore an oxidizing environment is needed to dissolve an excess concentration of dopants. In the highly overdoped regime, bivalent dopants of LCO do not necessarily provide mobile charge carriers. Instead, charged oxygen vacancies ($V_{\text{O}}^{\bullet\bullet}$) form, which trap the

doped holes and generate scattering centers in electrical transport. Close to the solubility limit, this reaction becomes dominant, therefore the nominal dopant concentration is not directly transferred to the carrier concentration, $p \neq x$. The chemical reaction is written as follows [MP91]:



However, using a reactive oxidizing atmosphere prevents the formation of oxygen vacancies, and enhances the solubility, which was demonstrated in LSCO as extension of the so-called superconducting dome to higher doping concentrations via high pressure oxygen treatments [TTN+88]. Therefore cation-substituted LCO thin films are usually grown in reactive oxidizing environments such as ozone or oxygen plasma, and single crystals need post annealing in high pressure oxygen in order to minimize the number of oxygen defects. There have been numerous studies on the negative influence of oxygen vacancies on the desired physical properties of transition metal oxides such as metallicity, ferromagnetism, ferroelectricity, and superconductivity. However, the detection and systematic study of oxygen defects have been largely elusive due to their atomically small size.

2.1.3 Ruthenium vacancies in strontium ruthenates

Strontium ruthenates such as SrRuO_3 (Sr-113) and Sr_2RuO_4 (Sr-214) are good conductors unlike many other transition metal oxides that are predominantly insulating or semiconducting, therefore they are considered as electrode-materials in oxide electronics. In addition, Sr-113 exhibits ferromagnetism and the anomalous Hall effect, and can thus be a potential component of spintronic devices. Sr-214 is an unconventional superconductor with maximum $T_c \sim 1.5$ K, whose pairing mechanism is still under debate.

Obtaining stoichiometric ruthenate thin films has been a challenge due to the volatility of some ruthenium oxide species, which induces ruthenium

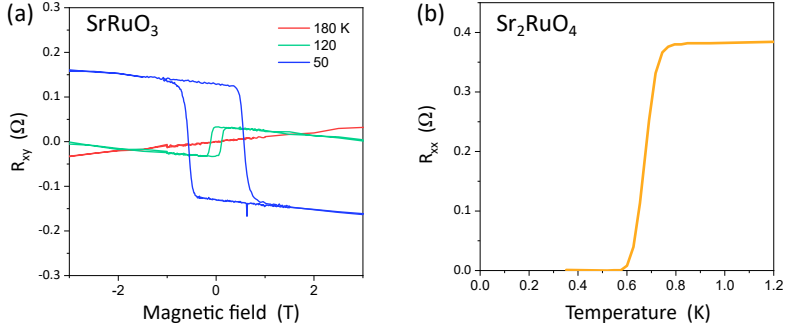


Figure 2.2: Representative electrical transport behaviors of SrRuO_3 and Sr_2RuO_4 thin films. (a) Hall Resistance curves that show hysteresis loops originated from the anomalous Hall effect. (b) Resistance curve of a Sr-214 thin film that shows the superconducting transition.

deficiencies. The main volatile species are RuO_3 and RuO_4 , and ruthenium vacancies, V_{Ru}'''' , form according to the reaction:



Ruthenium vacancies in strontium ruthenates are reported to suppress ferromagnetism and superconductivity in Sr-113 and Sr-214, respectively. In order to obtain stoichiometric ruthenate thin films, overabundant ruthenium should be provided during deposition, and excess ruthenium is removed from the sample as a form of ruthenium oxide gas, which is called the adsorption-controlled growth [NLR+18; NRS+18].

A typical measure of the concentration of ruthenium deficiency is the residual resistivity ratio (RRR), i.e. the ratio of resistivities at 300 and 4 K, which is a conventional indicator for the concentration of impurities in metals and alloys. Impurities in metals cause additional scattering and carrier localization that can enhance the resistivity as $T \rightarrow 0$ K. The RRR in clean samples is therefore usually high [Ber84; KM93]. Experimental studies on Sr-113 and Sr-214 have shown that a high RRR can be obtained

when a large concentration of ruthenium is provided during thin film growth. [NLR+18; NRS+18; SBG+16; SKV+07].

2.2 Spectroscopic properties

Photon-based spectroscopies have been invaluable tools in revealing the origin of the phase behavior and transport properties of solids, where the spectroscopic response of the light illumination reflects the vibrational and electronic structure of the sample. Owing to state-of-art optical instruments including the confocal Raman microscope, the synchrotron light source, and the Fourier-transform ellipsometer, we could investigate the spectroscopic responses of nanometer-scale-thick films. Within this section we will review the mechanisms underlying the spectroscopic responses we investigated.

2.2.1 Raman spectra of K_2NiF_4 type structures

Raman scattering is an inelastic process, during which photons lose or gain energy. The transferred energy corresponds to the frequency of quantized lattice vibrations called phonons with energies of tens of meV, which is determined by the eigen-frequencies of atoms in the electrostatic potentials around them. In analogy with classical oscillators, phonons with higher frequencies tend to involve lighter atoms.

Raman spectroscopy measures the intensity of scattered light as a function of the energy transferred to the photon, where Raman-active phonons show up as peaks. The Raman-activity of a phonon is determined by the local crystal symmetry, hence Raman spectroscopy can be used to determine the local structure of solids in combination with the polarization analysis. Thus, Raman spectroscopy can be more sensitive to point defects than other popular structural characterization methods, such as X-ray diffraction and transmission electron microscopy (TEM); we found clear differences in Raman spectra among samples that showed identical X-ray diffraction patterns and TEM images. In addition, the locally degraded symmetry around a defect site may lead to leakage of IR-active (*ungerade*) modes to Raman

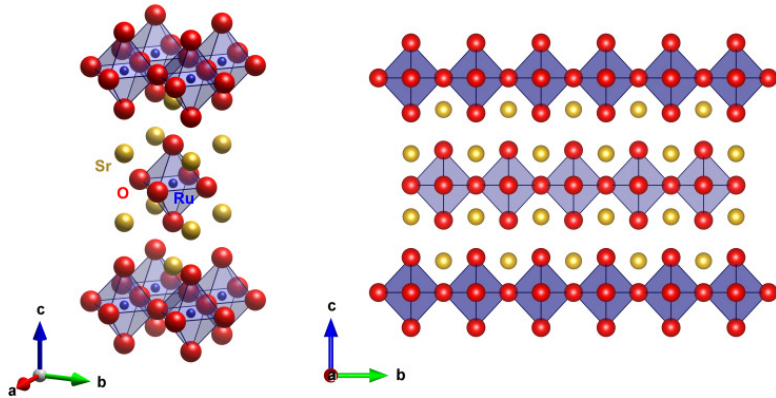


Figure 2.3: (left panel) The three-dimensional model of Sr-214 that has the K_2NiF_4 -type structure. (right panel) the projection of the structure into the bc plane. Yellow, blue, and red spheres represent Sr^{2+} , Ru^{4+} , and O^{2-} ions, respectively.

spectra (*gerade*) mediated by the the Fröhlich interaction, in which IR-active phonons interact with electrons through the electrostatic potential [Gin98]. Using this ability of Raman spectroscopy, we studied point defects in ternary transition metal oxides with K_2NiF_4 -type structure presented in Fig. 2.3 such as LSCO and Sr-214.

The selection rule for the Raman-active peaks is determined by group theory: the K_2NiF_4 -type structure has a space group called $I4/mmm$ (no. 139), and belongs to the point group D_{4h} . Once the crystal structure and the group representation are known, the normal modes can be determined using tables in the literature [RBP81]. A straightforward way of performing this analysis is to use a toolkit in the Bilbao crystallographic server, where all group theoretical analyses are done automatically using full crystallographic data [KAP+03]. According to the group analysis, the Raman-active modes, IR-active modes, and acoustic modes of the K_2NiF_4 are $2A_{1g} + 2E_g + 3A_{2u} + 4E_u$, and $A_{2u} + E_u$, respectively, and all Raman-active modes are associated with the apical oxygen atoms. In the case of Sr-214, three peaks, two A_{1g} and one E_g modes, were observed in polarization-resolved Raman spectroscopy,

where phonons with lower energy ($\sim 200 \text{ cm}^{-1}$) are associated with Sr, and high energy phonons ($\sim 550 \text{ cm}^{-1}$) are with the apical oxygen atoms [IPL+05]. In order to obtain a more complete set of phonon modes including both Raman- and IR-active modes, inelastic neutron scattering can be utilized, where momentum resolved data can be obtained. For example, all phonon modes including four Raman-active phonon modes ($2A_{1g} + 2E_g$) can be identified from phonon dispersion curves of Sr-214 obtained by inelastic neutron spectroscopy [BRS+07].

2.2.2 Electronic structure of Sr_2RuO_4

Ruthenium oxides, due to delocalized $4d$ electrons, were considered to display weak correlation effects in comparison to $3d$ transition metal compounds. However, recent investigations have demonstrated that ruthenates exhibit unexpected physical properties, and the origin of them has been attributed to the interplay of electronic correlation and spin-orbit coupling. Even the simplest ruthenium oxide, RuO_2 , which has long been considered a band metal, shows satellites in core-level spectra and itinerant antiferromagnetism that are inexplicable with the conventional band theory [BSD+17; KNKO04; ZSR+19]. The emergent phenomena in complex ruthenates have been motivated the development of new synchrotron-based beamlines for $4d$ compounds [JKP+17; SGI+19].

The Ru ion in Sr-214 has a charge of +4 and an electron configuration of $4d^4$. Its octahedral coordination in the oxygen network that envelops the ruthenium ions breaks the degeneracy of the $4d$ manifold into e_g and t_{2g} levels, where t_{2g} has lower energy due to reduced overlap with oxygen ions [EFLP61]. Naturally the four valence electrons occupy the t_{2g} orbitals, and form a low spin state with $S = 1$, however, Sr-214 does not show long-range magnetic order. As the t_{2g} orbitals are partially occupied, Sr-214 is a metal that exhibits a typical Fermi-liquid behavior at low temperatures ($\rho \sim T^2$). The detailed electronic configuration of Sr-214 is further complicated by spin-orbit coupling that lifts the degeneracy and mixes the orbital character

of t_{2g} through additional terms in the Hamiltonian:

$$\lambda_{so}\mathbf{L}\cdot\mathbf{S} + \frac{\Delta_{CF}}{3}\langle L_z \rangle^2 \quad (2.4)$$

where λ_{so} is the spin-orbit coupling constant, and \mathbf{S} and \mathbf{L} are spin and orbital angular-momentum operators, respectively [FDF+15]. The Δ_{CF} in the second term represents the intra- t_{2g} crystal field splitting, which separates the d_{xy} level further from the d_{xz} and d_{yz} levels [FDF+15; HET+08; VZR+14].

Experimentally the electronic structure of Sr-214 has been commonly studied via O K-edge core-level spectroscopy, because Ru-4d electrons in Sr-214 strongly hybridize with O-2p electrons thanks to the delocalized 4d electrons. The X-ray absorption near edge structure (XANES) and the resonant inelastic X-ray scattering (RIXS) at the O K-edge are appropriate methods to exploit this possibility, which revealed a value of $\lambda_{so} \sim 200$ meV, which is comparable to the crystal-field energy Δ_{CF} [FDF+15; HLG+00; MKK+06; PNP+07].

The strong spin-orbit coupling in d^4 ruthenates makes the system susceptible to the lattice degrees of freedom through a combined parameter, $\frac{\Delta_{CF}}{\lambda_{so}}$, thus the energy hierarchy can be dramatically modified with the lattice distortion: In Sr-214 the state with d_{xy} character has higher energy than states with d_{xz} and d_{yz} , on the other hand d_{xy} lies in the bottom among t_{2g} derived orbitals in Ca_2RuO_4 due to the opposite sign of $\frac{\Delta_{CF}}{\lambda_{so}}$. [FDF+15; HET+08; VZR+14].

2.2.3 Electronic structure of hole doped La_2CuO_4

The electronic phase diagram of superconducting cuprates is currently a puzzle to be solved, and also one of the most challenging problems in solid state physics, therefore a complete review of the topic would be out of scope of the thesis [KKN+15]. Instead, we will briefly introduce the orbital character of the band structure of hole doped LCO at high temperatures,

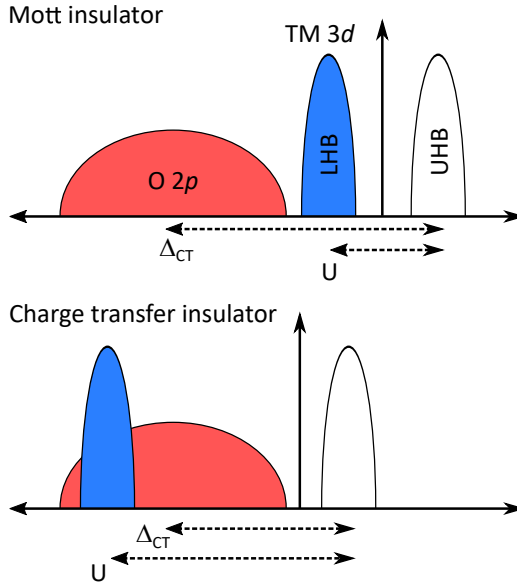


Figure 2.4: Schematic band diagrams of a Mott insulator and a charge transfer insulator. LHB and UHB stand for the lower- and the upper-Hubbard band, respectively.

which will be discussed in depth later in the context of optical spectra.

The insulating state of LCO is induced by strong Coulomb repulsion of the 3d electrons in the electron configuration of $3d^9$. In Mott insulators, the 3d-band is split into upper- and lower-Hubbard bands and generates a band gap, therefore the orbital characters of the highest occupied band (HOB) and the lowest unoccupied band (LUB) are predominantly 3d (see Fig. 2.4). LCO is categorized as a charge-transfer insulator which is closely similar to a Mott insulator, because the O-2p that is hybridized with Cu-3d plays the role of the HOB [ZSA85].

The role of the HOB becomes important when LCO is hole-doped, because mobile holes that superconduct below T_c have the orbital character of the HOB. The O-2p character of holes in doped LCO was confirmed by numerous XANES and RIXS measurements, where the holes appeared as a peak at the O

K-pre-edge, and the peak grows upon hole-doping [ARS+05; CSM+91]. The orbital character of the carriers is an essential input for models to describe the physics of copper oxide superconductors, hence the ligand-driven nature of holes has been considered in the models. Zhang and Rice built the earliest model that properly treats the complicated nature of the conduction band, which is called the Zhang-Rice singlet (ZRS) model, because the holes in in-plane oxygen networks form single state with the spins at copper sites [ZR88]. The ZRS model is the basis for the single-band effective Hamiltonian which has been successful to interpret the band structure and its spectroscopic responses. We studied the validity of the ZRS model over an unprecedentedly wide doping range using optical spectroscopy, and found that the ZRS model is valid up to very high Sr concentration, validity of which was challenged [PHS+09].

2.2.4 Spectroscopic techniques

We conclude this section by introducing the experimental setups we used in this thesis. The thin films we studied are only a few tens of nanometers thick, which is typically $10^{-5} \sim 10^{-4}$ of the volume of the substrate. In order to exclude the enormous contribution from the substrate and to extract the spectra from the thin film, spectroscopic methods that are specialized for thin films are needed, such as confocal Raman microscopy and spectroscopic ellipsometry.

In a Raman microscope, an optical microscope is integrated with a Raman spectrometer, such that samples with microscopic dimensions can be measured in a backscattering geometry. The confocal Raman microscope comprises additional optics including a confocal pin hole (see Fig. 2.5(a)), which greatly enhances the spatial resolution by rejecting signals out of the focal point. The confocality allowed us to obtain the Raman spectra of thin films, which are usually dominated by the signal from substrates in non-confocal setups.

Spectroscopic ellipsometry is one of the most widely-used techniques to obtain the optical conductivity of thin films, especially in semiconductor

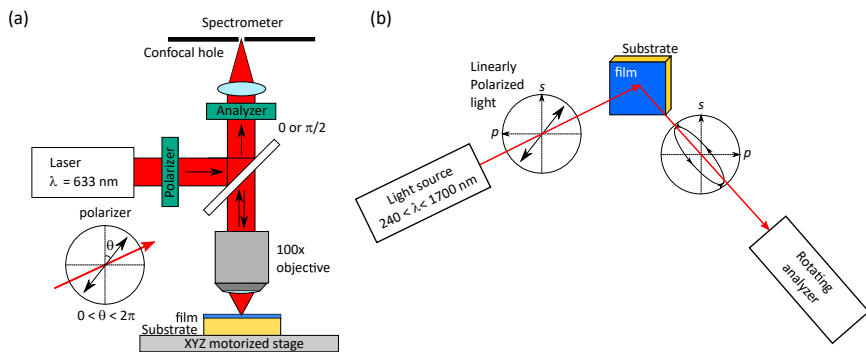


Figure 2.5: Schematic diagrams of experimental setups. (a) The confocal Raman microscope with the full polarization analysis capability. (b) The spectroscopic ellipsometer equipped with a rotating analyzer.

industry. It analyzes the polarization of the reflected light from thin film surfaces in the form of ψ and Δ , which are the ratio and the phase difference between p and s components of the light, respectively (see Fig. 2.5(b)), from which one can compute optical constants such as $\epsilon_1(\omega)$ and $\epsilon_2(\omega)$ [Fuj07]. Measurements are typically done in a reflection geometry with an incident angle close to the Brewster angle of the substrate $\theta \sim 70^\circ$. Spectroscopic ellipsometry has poor lateral resolution due to the large incident angle, nevertheless it has excellent vertical resolution that reaches down to sub-unit-cell regime, which makes it a perfect technique for thin films.

2.3 Synthesis of ruthenate thin films

Metallic ruthenates, Sr-113 and Sr-214, have played an important role in oxide electronics as electrodes owing to their good metallicity and chemical stability. Moreover, the large growth window of strontium ruthenates allowed them to be easily integrated into oxide-based devices with various synthesis conditions. Achieving high-quality ruthenates with ideal physical properties has been a challenge due to the volatility of ruthenium oxide precursors as mentioned in the previous section. In order to obtain stoichio-

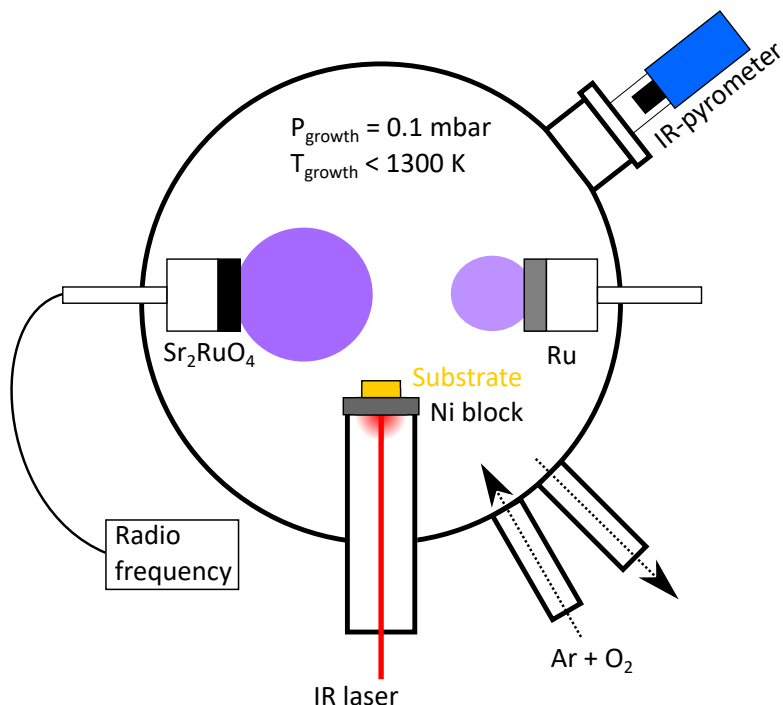


Figure 2.6: Schematic diagram of the reactive sputtering chamber that we used to grow ruthenate thin films.

metric ruthenate films, we developed an off-axis reactive sputtering chamber equipped with an infrared-laser heating system. Here we introduce the principles of the reactive sputtering method, and elaborate the advantages of our method in growing metallic ruthenates.

2.3.1 Off-axis reactive sputtering

Reactive sputtering is a physical-vapor-deposition (PVD) method, in which reactive gas ions are accelerated toward a target surface guided by magnetic fields, and ablate the target to transfer the target-materials to substrates. In case of oxide thin films Ar and O₂ are used as sputter and reactive gas,

respectively, where oxygen plasma oxidizes particles sputtered by the Ar ions. The word "off-axis" indicates the geometry of the sputtering process, where substrates are located away from the axis of the target in order to reduce the energy of impinging particles as described in the Fig. 2.6.

When it comes to deposition of metals with high evaporation temperatures, sputtering has a clear advantage over thermal-evaporation-based PVD methods such as pulsed laser deposition (PLD) and molecular beam epitaxy (MBE), because the ablation is done by the collision of ions with the target. Especially for ruthenates, sputtering is beneficial, because the ablation by physical collisions prevents overheating of the target, which is a problem in case of PLD: overheating of the target by the focused laser results in decomposition of the metal-oxide into the metal and oxygen, which happens in ruthenium-, rhodium-, and iridium-oxides that contain metals with high evaporation temperatures. The decomposed metal stays on the surface of the target, and makes the target reflective to the laser causing the off-stoichiometric ablation of the target. In case of MBE, thermal evaporation of such metals, which is the most stable way to provide an atomic beam, is currently not possible, instead, electron-beam evaporation is used to evaporate ruthenium [NRS+18; UIW+17].

Reactive sputtering has been eclipsed by PLD and MBE in solid-state physics, because of some disadvantages: re-sputtering of the deposited thin film, rough morphology due to the fast growth-rate, and difficulties in layer-by-layer control. Yet, the off-axis geometry solves many of the disadvantages of sputtering such as re-sputtering and surface morphology. The layer-by-layer control is still difficult in sputtering, because the magnetic fields from sputtering guns prohibit the adoption of reflection high energy electron diffraction (RHEED), however RHEED is not necessary in thin films with a single composition, for which it suffices to do *ex-situ* characterizations after growths. Nevertheless, several studies showed that sputtering is capable of growing superlattices with atomic precision using *ex-situ* characterization[GZS+12], and some efforts have been made to integrate RHEED to sputtering chambers by optimizing the distribution of magnetic fields inside the chamber [PPDE16].

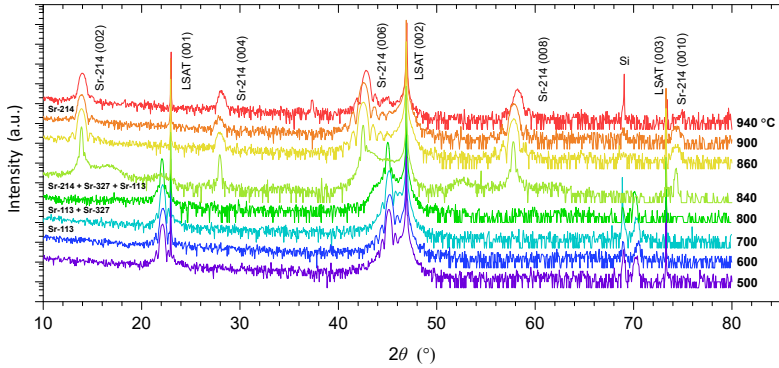


Figure 2.7: The temperature dependence of the Sr-Ru-O phases in thin films grown with a Sr-214 target.

2.3.2 Synthesis of Sr-113 and Sr-214 thin films via dual target ablation

There are two essential conditions of growing high-quality ruthenate thin films using a sputtering system. One is the high-temperature, $T_{substrate} > 850\text{ }^{\circ}\text{C}$, which is necessary to obtain the pure Sr-214 phase, and the other is an additional Ru target that provides an excess amount of ruthenium in order to prevent ruthenium deficiency. For these purposes, we introduced an infrared laser heating system to heat substrates to high temperatures, and a dual-target configuration, a Sr-214 target and a pure Ru target, to avoid the formation of ruthenium vacancies at high temperatures (see Fig. 2.6).

The importance of the growth temperature was demonstrated by XRD θ - 2θ scans from thin films with different $T_{substrate}$ (Fig. 2.7). The temperature dependence clearly shows that $T_{substrate}$ higher than $850\text{ }^{\circ}\text{C}$ is needed to destabilize the other phases such as Sr-113 and Sr-327. Temperatures higher than $900\text{ }^{\circ}\text{C}$ resulted in high ruthenium deficiency that drove the film into an insulating state, therefore it is important to keep the $T_{substrate}$ lower than $940\text{ }^{\circ}\text{C}$. In fact, the best samples were obtained at temperatures around $860\text{ }^{\circ}\text{C}$, which is slightly above the temperature that destabilizes the other Sr-Ru-O compounds.

As previously reported, at elevated temperatures achieving the Sr-214

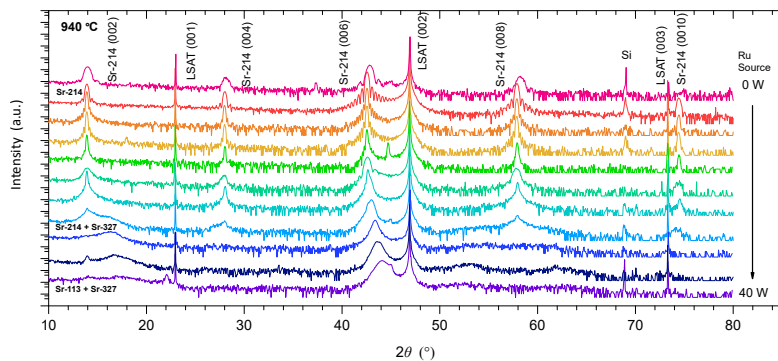


Figure 2.8: XRD θ - 2θ curves of thin films grown at 940 °C and with the fixed Sr-214 flux of 30 W and varied Ru flux as indicated in the plot.

phase is not difficult, but obtaining good conductivity is challenging due to the formation of ruthenium vacancies [NRS+18]. In order to prevent ruthenium deficiency an additional Ru flux is needed, and this has been done via excess supply of Ru using MBE or via using a Ru-rich target in PLD. In our system, we used a Ru-metal target in addition to the stoichiometric Sr-214 target to compensate the high volatility of ruthenium oxides. The extra ruthenium influx preserved the Sr-214 phase and improved the conductivity, however the superabundant amount of Ru resulted in parasitic phases such as Sr-113 and Sr-327 that are not stable at elevated temperatures (see Fig. 2.8). Therefore, it is important to find the optimal amount of excess Ru, which is at the border between Ru-rich and Ru-poor phases.

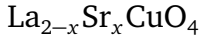
CHAPTER
3

POINT DEFECTS AND SPECTROSCOPIC RESPONSES

This chapter presents publication manuscripts that are published.
They are reprinted with the licenses from publishers.

- (1) Gideok Kim *et al.*, *Physical Review Materials* **1**, 054801 (2017) [[KCL+17](#)].
- (2) Gideok Kim *et al.*, *Physical Review Materials* **3**, 094802 (2019) [[KSH+19a](#)]

3.1 Selective formation of apical oxygen vacancies in



3.1.1 Abstract

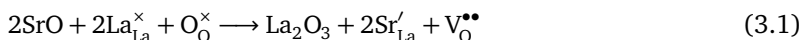
The superconducting properties of high- T_c materials are functions of the concentration of charge carriers, which is controlled by the concentration of defects including heterovalent cations, interstitial oxygen ions, and oxygen vacancies. Here we combine low-temperature thermal treatment of $\text{La}_{2-x}\text{Sr}_x\text{CuO}_4$ epitaxial thin films and confocal Raman spectroscopy to control and investigate oxygen vacancies. We demonstrate that the apical site is the most favorable position to accommodate oxygen vacancies under low-temperature annealing conditions. Additionally we show that in high-quality films of overdoped $\text{La}_{2-x}\text{Sr}_x\text{CuO}_4$, oxygen vacancies strongly deform the oxygen environment around the copper ions. This observation is consistent with previous defect-chemical studies, and calls for further investigation of the defect-induced properties in the overdoped regime of the hole-doped lanthanum cuprates.

3.1.2 Introduction

One of the greatest challenges in research on high-temperature superconductivity is separating the effect of chemical disorder and electronic correlations on the physical properties of the superconducting cuprates. All cuprates share two substructures [KKN+15; OM00]: the copper oxide (CuO_2) planes, which host the valence electron system, and the so-called charge reservoir, whose chemical composition is modulated by introducing impurities such as heterovalent cations, excess oxygens, or oxygen vacancies. The CuO_2 layers are insulating and antiferromagnetic if the Cu ions are in the valence state Cu^{2+} . The imbalance between the valence of dopant and host ions in the charge reservoir results in extra charges which are transferred into the neighboring CuO_2 sheets via apical oxygens. As a result, the CuO_2 planes are populated with charge carriers and become metallic and superconducting while preserving shorter antiferromagnetic correlations.

Among the superconducting copper oxides, $\text{La}_{2-x}\text{Sr}_x\text{CuO}_4$ (LSCO) is unique due to the fact that the carrier concentration can be finely tuned by varying the Sr concentration, unlike other cuprates with higher T_c that are doped by oxygen off-stoichiometry. A solid solution can be formed over a wide range of Sr concentration $0 < x < 1.3$ [STNM00]. This allows one to cover the full phase diagram across the whole superconducting dome from the undoped parent compound La_2CuO_4 to the highly overdoped regime where eventually superconductivity is lost.

Recent work on LSCO thin films has revealed an unusual temperature dependence of the superfluid density in highly overdoped LSCO [BHWB16], triggering a controversial discussion about the role of disorder in this regime of doping [BHWB16; LDB17b]. In this context, it is important to realize that Sr doping modifies not only the carrier concentration but also the defect concentration [MP91; SRF+87]. Indeed from a defect chemistry point of view, LSCO may also contain oxygen vacancies ($\text{V}_\text{O}^{\bullet\bullet}$) according to the equation [MP91]:



Here $\text{La}_{\text{La}}^\times$ and O_O^\times are neutral La and O atoms at La and O sites, respectively. According to equation (2.1), the two Sr atoms at the La site (charged with -1: Sr'_{La}) may generate an oxygen vacancy (charged with +2: $\text{V}_\text{O}^{\bullet\bullet}$) instead of two holes. The number of oxygen vacancies in bulk and thin films (δ) can be reduced by means of annealing under high-pressure oxygen or during epitaxial growth under a reactive oxidant atmosphere such as ozone or oxygen plasma [BAL+11; STNM00; TTN+88]. These treatments, as has been reported, extend the superconducting dome to higher doping levels both in bulk crystals and epitaxial thin films. The crystal structure of LSCO without interstitial oxygen (Figure 3.1(a)) shows that there are two different oxygen positions: (i) apical oxygen O(2) and (ii) basal oxygen O(1). The role of these two inequivalent oxygens has been the subject of many studies aimed at understanding their influence on the physical and chemical properties such as superconductivity and oxygen vacancy formation, respectively [PDM+16;

PDS+01; SUK+10; WHK10].

During the last decade it was demonstrated that high-quality LSCO epitaxial thin films and heterostructures can be grown by using ozone-assisted atomic layer-by-layer molecular beam epitaxy (ALL-MBE) [BHWB16; BLG+15]. Samples are generally fully oxidized over a wide range of doping, since the films are grown under high purity ozone atmosphere that even results in excessive interstitial oxygen staging in underdoped LSCO [STNM00]. Typically the concentration of carriers (holes) p in these films has been estimated as the concentration of Sr dopants, x ($p = x$) even in the overdoped regime [BHWB16]. However, the oxygen deficiency induced by Sr dopings in LSCO has not been widely studied, and is thus not well understood. One practical difficulty is that the presence of oxygen deficiency is difficult to detect.

Here we show that it is possible to selectively change the oxygen vacancy concentration and control it via *ex situ* postannealing. We also demonstrate that the $p = x$ assumption has a progressively more limited validity upon moving towards the overdoped regime. This information could be essential for further understanding the physics and chemistry of high temperature superconducting cuprates.

3.1.3 Experimental methods

Our tool of choice to study this issue is Raman scattering from LSCO thin films. Raman spectroscopy is an extremely sensitive probe of local symmetry changes, and oxygen occupancies in thin films can be more easily controlled than in the bulk form via the annealing process [IZHC97; LLP06]. We grew high quality LSCO epitaxial thin films each with four different Sr doping concentrations ($x = 0.16, 0.25, 0.35$ and 0.5) on LaSrAlO_4 (001) single crystalline substrates (Crystal GmbH) by using the ozone-assisted ALL-MBE system (DCA Instruments) [BLG+15]. Each film is 100 unit cells thick and all growths were controlled by using *in situ* reflection high energy electron diffraction (RHEED). The film quality was confirmed by using atomic force microscopy (AFM) and high resolution X-ray diffraction (XRD). During growth the substrate temperature was kept at 630°C according

to the radiative pyrometer, the pressure was $\sim 1 \times 10^{-5}$ Torr. A series of postannealing treatments was carried out in the growth chamber of MBE system: the base pressure was $\sim 1 \times 10^{-8}$ Torr for each vacuum annealing and $\sim 1 \times 10^{-5}$ for annealing in ozone. During each growth and ozone annealing run, ozone was supplied from a dedicated delivery system by evaporating liquid ozone. The diamagnetic response and resistance were measured simultaneously as a function of temperature in the range of 4.2-300 K using a motorized dip-stick. The temperature was varied by inserting the dip-stick into the transport helium dewar. The Raman spectra were measured with a Jobin-Yvon LabRam HR800 spectrometer (Horiba Co.) combined with a dedicated confocal microscope with motorized objective lens with short depth of focus that allows measurement of films with thicknesses of ~ 10 nm [HKB+15; HMF+14]. The samples were illuminated with a He-Ne laser with wavelength 632.8 nm, and the scattered light was collected from the sample surface with a 100x objective. The experiments were performed in backscattering geometry along the crystallographic c-axis.

3.1.4 Results and discussion

Figure 3.1 shows unpolarized Raman spectra of our LSCO films with Sr concentrations $x = 0.16, 0.25, 0.35$ and 0.5 . The spectra are vertically shifted for clarity. All Raman spectra have overall similar shapes in spite of the wide variation of x , and are consistent with previous reports on bulk samples [BGG+87; Sug89; WPW+88]. The strongest doping dependence is observed for the mode at $\sim 220 \text{ cm}^{-1}$ and the mode at $\sim 600 \text{ cm}^{-1}$: both peaks increase in intensity as the Sr concentration increases. The other phonons: at $\sim 150 \text{ cm}^{-1}$, $\sim 320 \text{ cm}^{-1}$, $\sim 360 \text{ cm}^{-1}$, and $\sim 450 \text{ cm}^{-1}$ are only weakly doping dependent. The peak at $\sim 220 \text{ cm}^{-1}$ has been assigned as the A_{1g} phonon mode that involves the even motion of the La/Sr atoms [BGG+87; Sug89; WPW+88] bonded to the apical oxygens O(2). Thus the change of the amplitude of this peak with Sr doping level can be interpreted either as a consequence of increasing Sr concentration or the formation of oxygen vacancies in the apical position. The amplitude change is even more dramatic

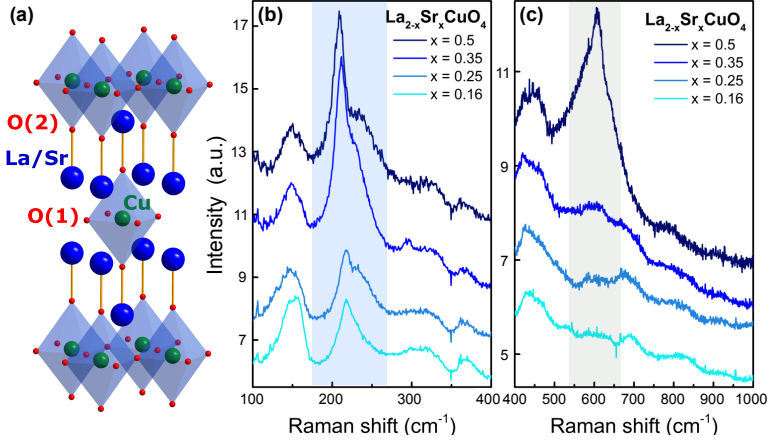


Figure 3.1: (a) The lattice structure for LSCO with tetragonal symmetry. (b), (c) Unpolarized Raman spectra from LSCO thin films with different doping levels. Spectra from $x = 0.25, 0.35, 0.5$ are shifted in the y direction 1, 1.4, 2.8 units for better visibility.

for the high energy mode at $\sim 600 \text{ cm}^{-1}$ presented in Fig. 3.1(c). This broad peak is present over the whole range of x and its spectral weight increases with x . This particular mode has not been systematically studied in LSCO and its origin and assignment remain controversial. In Refs. [SST+03; Sug89] an analogous high energy mode was observed in overdoped LSCO samples and assigned to oxygen vibrations, because the high-energy of the mode suggests a small atomic mass.

Interestingly, a similar broad peak located in the same energy range was observed in a number of Raman studies on different materials with similar crystal structure, such as LaSrAlO_4 [HCI+97] and electron-doped cuprates with T' structure [HLC+91]. Although the origin of this peak has not been conclusively established, previous studies suggest a connection with the presence of defects for this phonon mode with A_{1g} symmetry and they point out that it has a larger contribution with light polarized along the z axis. Here we use the same notation for this phonon mode as A_{1g}^* mode following Ref. [HLC+91]. The evolution of the peak at $\sim 600 \text{ cm}^{-1}$ with Sr concentration

possibly supports the hypothesis of a defect-induced origin of the A_{1g} mode. As this peak partially overlaps with the peak at 700 cm^{-1} which is essentially constant over the whole doping range, we plot the integrated area of the A_{1g}^* peak as a function of Sr concentration in Fig. 3.2(a). Taking into account the defect chemistry analysis [MP91] on the LSCO compound the enhancement of spectral weight is consistent with the presence of more oxygen vacancies. In order to further clarify the symmetry and origin of the phonon mode at $\sim 600\text{ cm}^{-1}$ in LSCO thin films, Raman spectra with ZZ polarization should be measured. Unfortunately the planar sample geometry of thin films makes it extremely challenging to collect the Raman signal from the out-of-plane z component.

We have overcome this challenge by measuring Raman spectra on tilted samples as described in Figure 3.2(b). We positioned LSCO ($x = 0.35$) on wedges with different angles θ . In this configuration we could pick up a partial contribution from the z direction that increases with the angular deviation from the original standard $z(YY)z$ geometry (in Porto's notation). The result from the angular-dependent measurements is presented Fig. 3.2(c), where a striking difference between XX and YY polarized spectra is clearly seen at $\theta = 70^\circ$ at $\sim 600\text{ cm}^{-1}$. The phonon mode at $\sim 600\text{ cm}^{-1}$ has a larger z component than the A_{1g} phonon mode at $\sim 220\text{ cm}^{-1}$. This observation is consistent with the above-cited previous studies on similar compounds. Along the lines of Ref. [HLC+91] we can assign this anisotropic phonon mode A_{1g}^* to the vibration of the apical oxygens at the vertices of the octahedral oxygen network surrounding the copper ions. Hence the spectral weights of A_{1g} and A_{1g}^* phonon modes in Raman spectra can be used as selective and sensitive markers to judge the local modifications of the crystal structure caused by formation of oxygen vacancies in the LSCO epitaxial thin films. In the following text, we focus on these markers to evaluate the tunability of oxygen concentration via low-temperature annealing under vacuum.

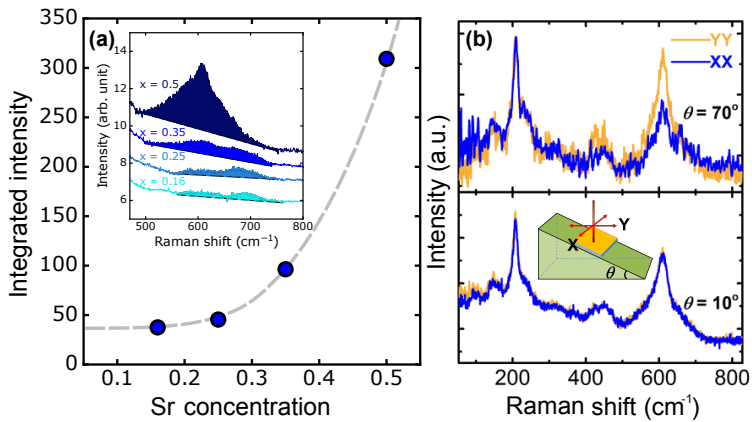


Figure 3.2: Analysis on the peak at $\sim 600 \text{ cm}^{-1}$. (a) Integrated intensity as a function of Sr concentration. The gray dashed line is a guide for the eye. (b) Comparison between spectra from 10° and 70° . the spectra are scaled to match the intensity of the peak at 220 cm^{-1} . Inset: Experimental setup for the angle dependence measurement. Yellow surface is the thin-film sample.

Table 3.1: The summary of mutual inductance measurements and XRD of LSCO thin films. The $T_{c,middle}$ is defined as the temperature where the imaginary part of the mutual inductance is maximized. This $T_{c,middle}$ is consistent with previous reports on the phase diagram of LSCO thin films grown by oxide MBE.

Nominal doping	Treatment	$T_{c,onset}$ (K)	$T_{c,middle}$ (K)	c (Å)
$x=0.16$	as grown	40	37	13.277
	1st annealed at 280 °C for 30 mins in vacuum	40	34	-
	2nd annealed at 280 °C for 30 mins in vacuum	26	< 4.2	13.259
	ozone annealed at 630 °C for 1 hrs in Ozone	39	34	13.289
$x=0.25$	as grown	31	25	13.24
	1st annealed at 280 °C for 20 mins in vacuum	30	24	13.24
	2nd annealed at 280 °C for 40 mins in vacuum	28	21	13.252
	ozone annealed at 630 °C for 1 hrs in Ozone	30	25	13.297
$x=0.35$	as grown	15	10	13.29
	1st annealed at 280 °C for 30 mins in vacuum	17	13	13.277
	2nd annealed at 280 °C for 240 mins in vacuum	< 4.2	< 4.2	13.265
	ozone annealed at 630 °C for 1 hrs in Ozone	15	10	13.285

Using a series of vacuum annealing processes we could vary the concentration of oxygen vacancies in our films. After each annealing process the superconducting transition temperature T_c , the diamagnetic response and XRD were measured. In Table 3.1 we summarize samples, details of the annealing process, superconducting transition temperatures and c -axis lattice constants as obtained from the XRD measurements. We studied three LSCO samples with different Sr doping levels $x = 0.16$ (optimum doping), 0.25 and 0.35 (overdoped). In Tab. I two superconducting transition temperatures are listed: $T_{c,onset}$ is the temperature at which the real and imaginary parts of mutual inductance start to change due to the diamagnetic screening, whereas $T_{c,middle}$ corresponds to the temperature where the imaginary part of the mutual inductance is maximized. Vacuum annealing processes reduce T_c in all samples. Only in the case of overdoped LSCO with $x = 0.35$ the first vacuum annealing slightly increased T_c due to the compensation of extra holes by electrons from $V_O^{\bullet\bullet}$. Nonetheless, a second vacuum annealing process suppressed T_c underreaching the T_c of the optimum doped sample. This already indicates that the lattice distortions induced by $V_O^{\bullet\bullet}$ play an important role in determining T_c together with carrier concentration in the CuO_2 planes. T_c was recovered by annealing in ozone as shown in Table 3.1 for the optimum doped LSCO film. The reversibility of T_c suggests that the formation of oxygen vacancies in high-quality LSCO films is also reversible. Notably, while T_c was remarkably suppressed after a second annealing in vacuum, the reduction of the c -lattice constant was only moderate.

In order to clearly demonstrate that these peaks stems from oxygen deficiency, we looked at the Raman modes $\sim 220 \text{ cm}^{-1}$, and $\sim 600 \text{ cm}^{-1}$ after each vacuum annealing that can modify the concentration of oxygen ions in the thin films. The unpolarized Raman spectra for three LSCO films $x = 0.16, 0.25$ and 0.35 measured after consecutive annealing processes are presented in Figure 3.3(a)-3.3(c), respectively. For clarity the spectra are vertically shifted. For comparison we plot also the spectrum obtained from the bare LaSrAlO_4 substrate (gray line) that contributes to the overall Raman signal from the samples. As mentioned above the strongest doping dependence of the spectral weights in the as-grown LSCO films was observed at \sim

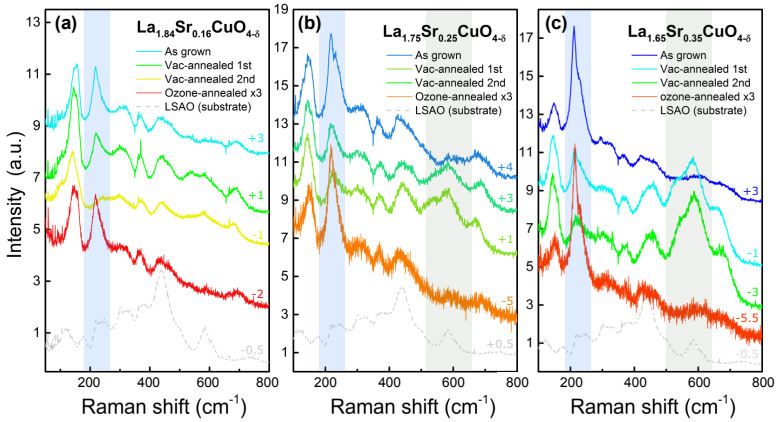


Figure 3.3: Raman spectra from annealed samples with different Sr concentrations: (a) $x=0.16$, (b) $x=0.25$, (c) $x=0.35$. Spectra are shifted in the y direction for better visibility. The numbers above spectra are the amounts of shifts in arbitrary units.

220 cm^{-1} (blue-shaded area), and $\sim 600 \text{ cm}^{-1}$ (gray-shaded). Subsequent annealing of LSCO films in vacuum at 280°C has a dramatic effect on both modes in all three samples.

The spectral weight of the mode at $\sim 220 \text{ cm}^{-1}$ is progressively suppressed with each vacuum annealing due to the increase in $V_{\text{O}}^{\bullet\bullet}$ at the apical site that, in turn, affects the motion of La/Sr atoms. Annealing in ozone recovers this peak to the initial value for all three doping concentrations, as shown in Fig. 3.3. On the other hand the spectral weight of the A_{1g}^* phonon mode at $\sim 600 \text{ cm}^{-1}$ gradually increases after the vacuum annealing processes, differently from the in-plane modes at $\sim 320 \text{ cm}^{-1}$ and $\sim 370 \text{ cm}^{-1}$ which do not vary with doping and thermal treatment. Our findings thus imply a selective generation of oxygen vacancies at the apex of the octahedron, O(2) in Fig. 3.1(a). This is supported by the changes of the apical-related modes at ~ 220 and $\sim 600 \text{ cm}^{-1}$ and by the fact that the other planar modes remain unchanged.

3.1.5 Conclusion

In conclusion, our study has provided insights into the defect chemistry of high-quality LSCO epitaxial films grown by ozone-assisted MBE: (i) the amount of oxygen vacancies $V_{\text{O}}^{\bullet\bullet}$ increases strongly as a function of Sr doping even in samples grown under highly oxidizing environment; (ii) the oxygen vacancies can be selectively introduced at the apical position of CuO_6 octahedron by low-temperature annealing in vacuum; (iii) confocal Raman microscopy is an appropriate tool to investigate oxygen defects in thin epitaxial oxide films, complementary to other techniques such as positron annihilation spectroscopy [GCH+10].

Moreover the increasing tendency to form $V_{\text{O}}^{\bullet\bullet}$ in high quality LSCO thin films as x increases highlights an important source of disorder that one needs to consider in interpreting the physical properties of transition metal oxides. We used a prototypical layered transition metal oxide LSCO compounds as a form of thin film to take an advantage of an effect of oxygen annealing. Furthermore the higher tendency of overdoped samples to accommodate $V_{\text{O}}^{\bullet\bullet}$ suggests to focus on the relatively cleaner underdoped regime to study the intrinsic properties of the superconducting LSCO. We used the prototypical layered transition metal oxide LSCO to investigate the effect of annealing in different oxygen environments on the defect concentration. The higher tendency of overdoped samples to accommodate $V_{\text{O}}^{\bullet\bullet}$ calls for further investigations of the influence of disorder on the superconducting properties in this regime of the phase diagram [BHWB16; LDB17b]. Finally the selective generation of apical oxygen vacancies could provide an *in situ* tool to tune the electronic structure of LSCO without major disruption of the CuO_2 plane [WAN+16].

3.2 Electronic and vibrational signatures of ruthenium vacancies in SRO thin films

3.2.1 Abstract

The synthesis of stoichiometric Sr_2RuO_4 thin films has been a challenge because of the high volatility of ruthenium oxide precursors, which gives rise to ruthenium vacancies in the films. Ru vacancies greatly affect the transport properties and electronic phase behavior of Sr_2RuO_4 , but their direct detection is difficult due to their atomic dimensions and low concentration. We applied polarized x-ray absorption spectroscopy at the oxygen K edge and confocal Raman spectroscopy to Sr_2RuO_4 thin films synthesized under different conditions. The results show that these methods can serve as sensitive probes of the electronic and vibrational properties of Ru vacancies, respectively. The intensities of the vacancy-related spectroscopic features extracted from these measurements are well correlated with the transport properties of the films. The methodology introduced here can thus help to understand and control the stoichiometry and transport properties in films of Sr_2RuO_4 and other ruthenates.

3.2.2 Introduction

Ruthenium oxides have long served as model compounds for the influence of spin-orbit interactions on the electronic properties of strongly correlated electron systems. The layered compound Sr_2RuO_4 has attracted particular attention because it exhibits textbook Fermi liquid behavior as well as an unconventional superconducting state whose microscopic description continues to be strongly debated [MJD+96; MSHM17; PLC+]. As the valence electrons reside in the nearly degenerate t_{2g} levels of the Ru ions in the tetragonal crystal field, externally imposed lattice distortions in the form of uniaxial [BGM+18; SZB+17] or biaxial strain [BAM+16; HCR+16] have been shown to profoundly affect the phase behavior and physical properties. In particular, recent angle-resolved photoelectron spectroscopy studies performed *in-situ* on Sr_2RuO_4 thin films demonstrated that the Fermi surface is

very sensitive to epitaxial strain [BAM+16; HCR+16].

Since its in-plane lattice parameters ($a=b=3.87\text{\AA}$) are similar to other ternary transition metal oxides that exhibit novel physical properties, Sr_2RuO_4 can be readily integrated into all-oxide thin film devices. Compared to most functional transition metal oxides, which are insulators, several ruthenates including Sr_2RuO_4 and its cubic perovskite analogue SrRuO_3 exhibit good metallic properties, which make them suitable as electrode materials for oxide electronics [KKS+12]. In several recent studies, for example, SrRuO_3 is used as a standard electrode for ferroelectric tunnel junctions [GB14]. Sr_2RuO_4 , on the other hand, has high thermal stability even up to 1000°C , which makes it an appealing candidate for a bottom electrode that must withstand the high growth temperatures of oxides deposited on top of it [TL17]. In addition, SrRuO_3 - Sr_2RuO_4 heterostructures have recently been used to explore fundamental properties of the superconducting state in Sr_2RuO_4 [ALI+16; CKLT18; MBS18].

Despite the fundamental interest and potential applications, the growth of high quality ruthenate thin films has proven to be very challenging due to the nature of ruthenium and its oxides [CMV+16; KUT+10; MKAS17; NLR+18; NRS+18; TL17; UIW+17]. In fact, the high volatility of ruthenium oxides ($\text{RuO}_{x=2,3,4}$) leads to ruthenium deficiency, as shown in numerous reports [DCK+04; NLR+18; NRS+18; SBDD15; SBG+16; SKV+07]. The ruthenium deficiency increases the resistivity and reduces the Curie temperature of SrRuO_3 and is detrimental to superconductivity in Sr_2RuO_4 . In extreme cases, SrRuO_3 and Sr_2RuO_4 even show semiconducting behavior at low temperatures [CMV+16; DCK+04]. Superconductivity in Sr_2RuO_4 is extremely sensitive to defects, such as nonmagnetic impurities and lattice imperfections and thus it requires high quality samples [MHT+98; MMM99]. In order to overcome the volatility of ruthenium oxides, some of us have recently used an adsorption-controlled growth technique to synthesize ruthenate thin films showing superconductivity and unprecedentedly high residual resistivity ratios, defined as the ratio of the resistivities at 300 and 4K [NLR+18; NRS+18]. Related results have also been reported by other groups where the growth of Sr_2RuO_4 films was carried out by means of molecular beam

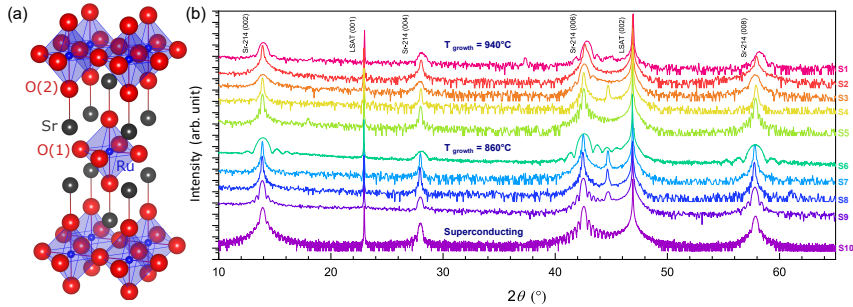


Figure 3.4: (a) The lattice structure of Sr₂RuO₄ with tetragonal symmetry. (b) XRD θ - 2θ scans of thin films. The sharp peak between Sr-214 (006) and LSAT (002) is the so-called hybrid reflection from combined diffraction of the film and substrate [DSC+18]. The y-axis is logarithmic and the curves are shifted in the y direction for better visibility.

epitaxy [MKAS17; UIW+17].

Nevertheless, a method to directly detect the ruthenium vacancies is still lacking due to their atomic dimensions and low concentration. Until now, the most common approach is based on using the residual resistivity that increases when defects are introduced. However, this method can only provide indirect evidence of Ru vacancies, and different factors (such as microstructural defects) can also contribute to the residual resistivity. To directly and specifically detect the ruthenium vacancies, a characterization tool that is sensitive to the local crystalline environment is required.

Here we report a combination of spectroscopic methods to directly identify ruthenium vacancies in Sr₂RuO₄. Specifically, we utilized X-ray absorption spectroscopy (XAS) and Raman spectroscopy to investigate thin films grown by the adsorption-controlled growth technique using either reactive sputtering or molecular-beam epitaxy (MBE). These complementary spectroscopic methods provide information on the modified hybridization between ruthenium and oxygen orbitals and on the local lattice distortions induced by ruthenium deficiencies, respectively. The spectroscopic signatures of ruthenium vacancies discussed in this work can thus serve as a guiding tool for

the growth of ruthenate thin films with controlled stoichiometry, which will benefit both fundamental studies and oxide electronics applications.

3.2.3 Experimental details

Thin films were grown on $(\text{LaAlO}_3)_{0.3}\text{-(SrAl}_{0.5}\text{Ta}_{0.5}\text{O}_3)_{0.7}$ (LSAT) (001) single-crystalline substrates (CrysTec GmbH) using either a reactive sputtering system developed at the Max Planck Institute for Solid State Research or an oxide MBE system at Cornell University. For reactive sputtering, argon and oxygen gas were supplied via a mass flow controller. The pressures P_{O_2} and P_{total} were 50 and 100 mTorr, respectively. Substrates were glued with a platinum paste to pure nickel blocks and heated with an infrared laser. The substrate temperature was monitored using a radiative pyrometer using the emissivity of $\epsilon_{\text{LSAT}}=0.92$. The structural quality of the films was confirmed by high-resolution X-ray diffraction (XRD) with a Cu K- α source ($\lambda \sim 1.5406$ Å) and by transmission electron microscopy. The growth parameters for the oxide MBE films have been presented elsewhere [NRS+18]. All the samples investigated in this study are listed in table 3.2.

Table 3.2: List of samples. The samples are listed in order of their residual resistivity ratios (see Fig. 5.3). Samples labeled “metal-insulating” show a resistivity minimum as a function of temperature (Fig. 2). The thicknesses were calculated using Laue fringes in XRD θ - 2θ scans.

Sample	Transport	T_{growth} (°C)	d (nm)	Technique
S1	Insulating	940	16	Sputtering
S2	Metal-insulating	940	48	Sputtering
S3	Metal-insulating	940	16	Sputtering
S4	Metal-insulating	940	50	Sputtering
S5	Metal-insulating	940	42	Sputtering
S6	Metal-insulating	860	11	Sputtering
S7	Metal-insulating	860	62	Sputtering
S8	Metal-insulating	860	67	Sputtering
S9	Metallic	860	26	Sputtering
S10	Superconducting	860	28	MBE

The electric transport measurements were carried out using a Physical Property Measurement System (Quantum Design Co.). To implement the van der Pauw geometry, Ag/Au metallic contacts were deposited with a sputtering on four corners of square shaped samples (5 mm \times 5 mm). The values of resistivity at room temperature (300 K) are 48255.5, 1126.4, 651.1, 640.9, 457.1, 245.4, 189.3, 171.0, 211.7 $\mu\Omega\cdot\text{cm}$ in *S1-S9*, respectively.

The Raman spectra were measured with a Jobin-Yvon LabRam HR800 spectrometer (Horiba Co.) combined with a dedicated confocal microscope with the 100 \times long working distance objective lens. The short depth of focus allows measurements of films with thicknesses of \sim 10 nm. The samples were illuminated with a He-Ne laser with wavelength 632.8 nm (red), and the scattered light was collected from the sample surface with a 100 \times objective. The experiments were performed in backscattering geometry with (*a,b*)-axis polarized light propagating along the crystallographic *c*-axis, which is denoted as $z(XX)\bar{z}$ in Porto's notation.

The XAS measurements were carried out at the O K-edge at the BL29-BOREAS beamline at the ALBA synchrotron light source (Barcelona, Spain) [BNC+16]. The spectra were measured in total electron yield (TEY) mode under ultrahigh vacuum conditions (1.5×10^{-10} Torr).

For scanning transmission electron microscopy (STEM), we prepared representative cross-sectional electron transparent specimens by employing the standard specimen preparation procedure including mechanical grinding, tripod wedge polishing, and argon ion milling. After the specimens were thinned down to \sim 10 μm by tripod polishing, argon ion beam milling, for which a precision ion polishing system (PIPS II, Model 695) was used at low temperature, was carried out until reaching electron transparency. For all STEM analyses, a probe-aberration-corrected JEOL JEM-ARM200F equipped with a cold field-emission electron source, a probe Cs-corrector (DCOR, CEOS GmbH) and a large solid-angle JEOL Centurio SDD-type energy-dispersive X-ray spectroscopy (EDXS) detector was used. The collection angle range for high-angle annular dark-field (HAADF) images was 75-310 mrad. To decrease the noise level, the images were processed with a principal component analysis routine.

3.2.4 Results and discussion

Since ruthenium deficiency in Sr_2RuO_4 (SRO) thin films is strongly dependent on the growth conditions, the adsorption-controlled growth that employs a large flux of ruthenium is an appropriate way to control the stoichiometry [NRS+18]. For adsorption-controlled growth of oxides, an oxidation agent is required to evaporate excessive ruthenium as some form of RuO_x (g) and to fully oxidize the films. For this purpose, we used concentrated (distilled) ozone in oxide MBE and an oxygen plasma in reactive sputtering. We sputtered SRO thin films with different concentrations of ruthenium defects by tuning two growth parameters, namely the deposition temperature and the ratio between ablations of stoichiometric SRO and ruthenium metal targets. We kept the oxygen partial pressure of the chamber constant during growths and rapid cooling processes to avoid variations in oxygen content. In order to obtain the insulating sample *S1* with the highest concentration of ruthenium vacancies, we prepared the sample 940°C using only the SRO target, exploiting the fact that more ruthenium vacancies are generated at higher temperatures.

We investigated the structure of all SRO films using XRD. Figure 3.4 (b) shows the 00L reflections from LSAT and SRO observed in θ - 2θ scans which demonstrate that the films were oriented along the c axis without parasitic phases. All curves show Laue fringes, which indicates smooth surfaces and interfaces. Reflections from different samples show nearly identical peak positions with only minor variations, except for the sample *S1* that has a smaller c lattice parameter due to the excessive ruthenium deficiency.

Although the XRD curves only display minor differences, the transport properties vary substantially, ranging from insulating to metallic and finally to superconducting behavior (Fig.3.5). The resistance curves were normalized to the resistance at 320 K to highlight the differences in the low-temperature properties. One sample, *S1*, exhibits a completely insulating behavior that has not been observed before except for exfoliated nano-sized single crystals [NMT17]. This is consistent with the expectation of high ruthenium deficiency in samples grown with extreme growth parameters.

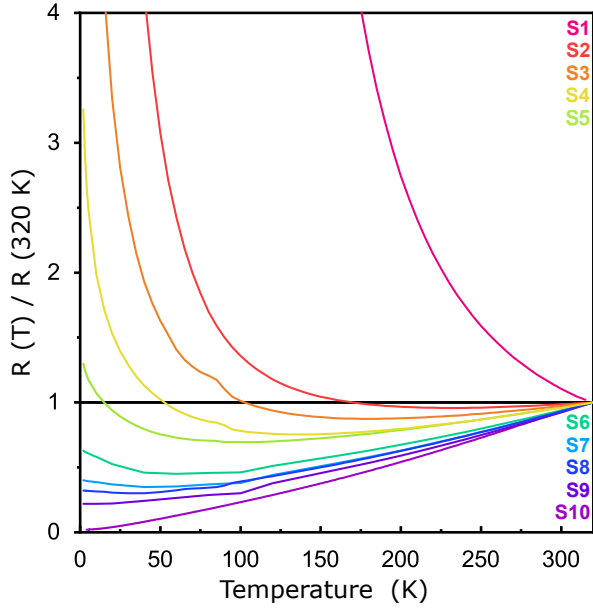


Figure 3.5: Normalized resistance curves. The kink at 80 K in some of the curves is an instrumental artefact.

The samples grown at 940 °C (*S1,2,3,4,5*) have higher normalized resistances than the samples grown at 860 °C (*S6,7,8,9*), which suggests that the higher growth temperature favors the formation of defects. The MBE-grown sample *S10* has a very low residual resistivity and is superconducting at $T_{c,midpoint} = 0.67$ K.

We collected STEM-HAADF images to investigate if and how details of the structure could result in different transport properties. Two representative samples, *S9* and *S5*, that were grown at different temperatures were examined (Fig. 3.6). Although the two samples show very different transport properties, the STEM images are strikingly similar. Both samples show perfect epitaxial qualities demonstrated by the absence of parasitic phases and structural defects over hundreds of nanometers. The high magnification HAADF images show the ideal K_2NiF_4 structure, consistent with the hypoth-

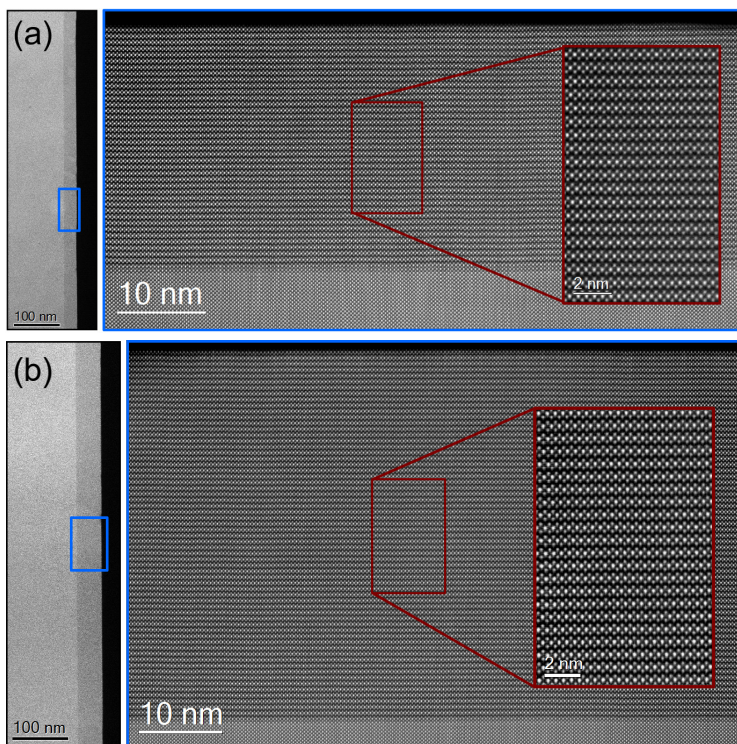


Figure 3.6: HAADF images for (a) *S9* and (b) *S5* samples. The blue and red squares indicate the magnified regions. The brighter spots are from ruthenium atoms and the other spots are from strontium atoms.

esis that the different transport properties arise from atomic-scale defects. The seemingly ideal structures of both fully metallic and metal-insulating samples imply that the insulating behavior does not stem from parasitic phases such as $\text{Sr}_3\text{Ru}_2\text{O}_7$ or SrRuO_3 .

Atomic-scale point defects can be studied by core level spectroscopy thanks to its sensitivity to the bonding environment of an atom. Metal vacancies in metal oxides affect the chemical properties of the materials by reducing the number of metal-oxygen bonds, and raising the oxidation state as the

number of oxygen atoms per metal increases. The higher oxidation state and the reduced number of bonds reduce the hybridization of the metal ion with the surrounding ligands. In SRO, ruthenium is hybridized with oxygen ions in a $[\text{RuO}_6]^{4-}$ complex, and this is reflected in O K-edge X-ray absorption spectra as pre-edge peaks [MKK+06; PNP+07; SCB+96]. There are two inequivalent oxygens in SRO: a planar oxygen labeled as O(1), and an apical oxygen labeled as O(2) (Fig. 3.4(a) and inset to Fig. 3.7(b)). XAS with linearly polarized light can resolve the difference between O(1) and O(2) thanks to the angle-dependence of the signal, as X-ray absorption occurs selectively in orbitals that lie parallel to the electric-field vector of the incoming x-rays.

We carried out linearly polarized XAS measurements near the O K-edge in TEY mode on four of our films at room temperature (Fig. 3.7). The c axis of the samples is perpendicular to the surface, so that the spectra are more sensitive to the planar O(1) at normal incidence, $\theta_i = 90^\circ$, and pick up substantial contributions from the O(2) as θ_i approaches grazing incidence, towards $\theta_i = 0^\circ$ (Figure. 3.7(a)). However, instead of changing the incident angle, we fixed it at 30° and controlled the polarization of the incident x-rays. In this configuration, the vertical polarization (σ -pol) is always parallel to the Ru-O(1) bond, and the horizontal polarization (π -pol) picks up contributions from both Ru-O(1) and Ru-O(2) bonds. Given the 30° angle from Ru-O(2), the signal from O(2) is dominant. The advantage of this configuration is that we can minimize variations of the footprint area of the X-ray beam, by keeping the incident angle fixed during the measurements.

Four samples with different transport properties were chosen for the measurements. The metallic sample *S9* shows spectra consistent with the previously reported spectra of single crystals, thereby confirming a good sample quality [MKK+06; SCB+96]. On the other hand, the less conducting samples *S6* and *S5* exhibit spectra with suppressed pre-peak spectral weight. Especially the spectral weight between 529 eV and 533 eV is progressively suppressed in measurements with π -polarization. On the other hand, the peak at 529 eV and 534 eV in the σ -polarized spectra shows a smaller suppression. The spectra from the insulating sample *S1* reveal a somewhat

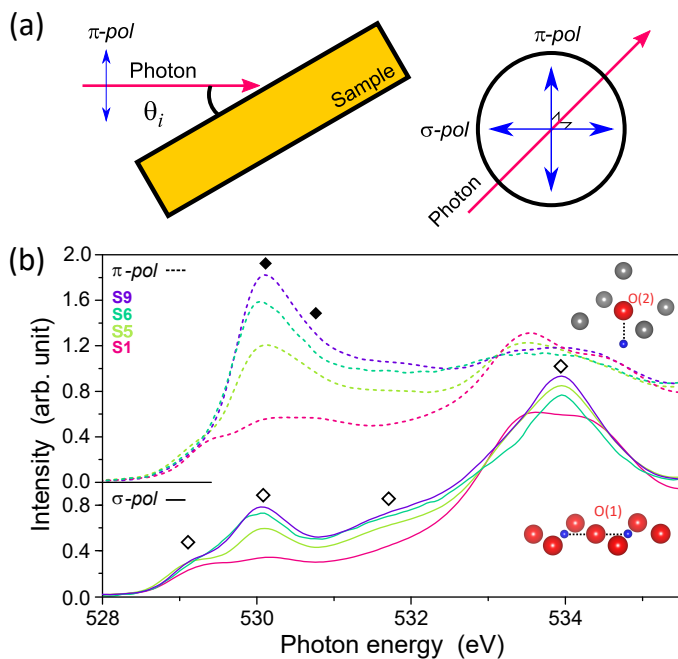


Figure 3.7: (a) Schematic diagram of the XAS measurement geometry. (b) X-ray absorption near O K-edge spectra. The full and empty diamond shapes indicate peaks from O(2) and O(1), respectively. The insets show the bonding configuration of O(1) and O(2) with Ru. The blue spheres are ruthenium atoms and the grey spheres are strontium atoms consistent with Fig. 3.4(a).

different shape from the other three samples due to the high concentration of ruthenium vacancies and its insulating behavior at room temperature, and also show greatly suppressed spectral weight at the pre-edge.

The change in spectral weight in the pre-edge structure can be interpreted as a signature of the ruthenium vacancies due to the above-mentioned reduced number of bonds and diminished hybridization. In particular, the stronger suppression of the out-of-plane component is remarkable and can be explained by a different number of ruthenium atoms in proximity to O(1) and O(2). As depicted in the inset of Fig. 3.7(b), the O(1) has two bonds

with neighboring ruthenium atoms in the xy plane, whereas O(2) has only one bond with Ru in the z -direction. The apical oxygen is therefore more sensitive to the presence of ruthenium vacancies.

Now we shift our attention to the local lattice distortion produced by the ruthenium vacancies. The absence of a ruthenium atom not only generates a void, but also distorts the lattice around the vacancy site, which results in lower local lattice symmetry. Raman spectroscopy is a suitable tool to study the change in local symmetries in crystals, because the Raman-activity of a phonon mode can be determined by a group-theoretical analysis of the lattice. SRO has a simple lattice structure with tetragonal symmetry, and the Ru and O(1) atoms are located in centrosymmetric positions. Due to the high symmetry, only four Raman modes ($2A_{1g} + 2E_g$) are expected from group theory [IPL+05].

The recent development of confocal Raman spectroscopy, based on an optical microscope with motorized objective lens and a confocal hole to reject substrate contributions, has provided new information on thin films down to thicknesses of a few nanometers, including the strain dependence of charge ordering phenomena, thickness dependent lattice structures, and oxygen vacancies [HMF+14; KCL+17]. We used a confocal micro-Raman setup to examine the local structural change in ruthenium deficient SRO thin films, where the signal from the thin film can be extracted using a depth-resolved measurement [HMF+14]. The thin film shape restricted the measurement to the $z(XX)\bar{z}$ geometry, in which the propagation of light is parallel to the surface normal, and the polarization of the light is parallel to the a axis of the lattice. In this geometry we could study phonon modes with $A_{1g} + B_{1g}$ symmetry, including the two A_{1g} phonon modes at 200 cm^{-1} and 545 cm^{-1} that are related to the vibration of Sr and O(2) in the z direction [IPL+05; SNM+01].

In Figure 3.8, we present substrate-subtracted Raman spectra acquired at room temperature for all investigated samples. The spectra were normalized to the peak at 545 cm^{-1} , and shifted along the y -axis for the sake of readability. The metallic and superconducting samples, *S9* and *S10*, show two sharp peaks from A_{1g} phonon modes, as observed in single crystals [IPL+05;

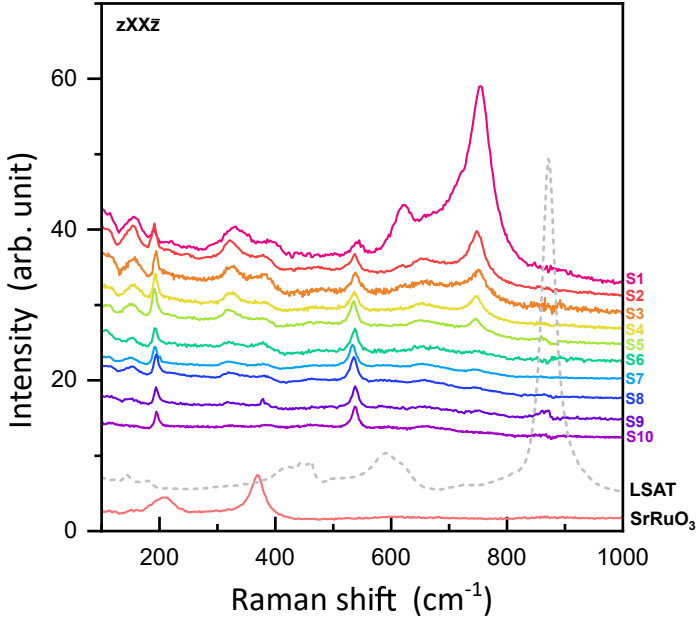


Figure 3.8: Polarized Raman spectra acquired at room temperature. The gray dashed curve is the LSAT substrate signal that was subtracted out in the analysis.

[SNM+01]. In less metallic samples, additional peaks appear in two energy windows: between 300 and 400 cm^{-1} , and between 600 and 800 cm^{-1} . The spectra from the substrate and SrRuO_3 are plotted in Fig. 3.8 to demonstrate that the additional features are neither originating from the substrate nor from impurity phases. The spectral weight of the additional features grows as the samples become more insulating, thereby revealing a strong correlation between the Raman spectra and the transport properties. As a consequence we can safely assign the new peaks to Raman-active phonon modes originating from the locally reduced symmetry induced by ruthenium vacancies.

In order to investigate the nature of the new features, magnified spectra are displayed in Fig. 3.9. The energies and spectral shapes of the new

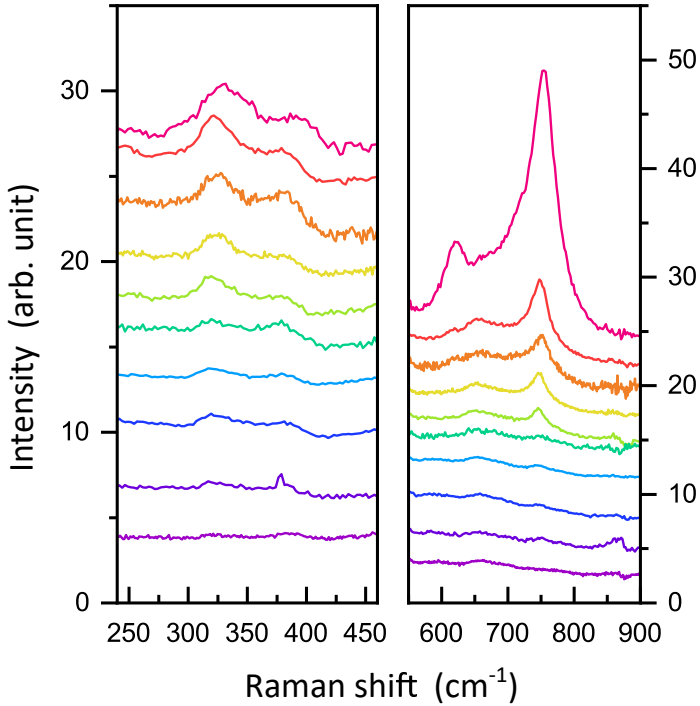


Figure 3.9: Detailed view of the Raman features attributed to Ru vacancies in Fig. 3.8.

features suggest that peaks at higher energy (E), $600 \text{ cm}^{-1} < E < 800 \text{ cm}^{-1}$, are overtones of the phonon modes at lower energy, $300 \text{ cm}^{-1} < E < 400 \text{ cm}^{-1}$. Specifically, the former peaks are seen at exactly twice the energies of the latter peaks, as expected for second-order overtone modes in the harmonic approximation. Moreover, the intensities of all new peaks grow proportionately in less conducting samples, which points to a common underlying origin. Ruthenium vacancies thus generate at least two phonon modes in the range $300 \text{ cm}^{-1} < E < 400 \text{ cm}^{-1}$, and their overtones are visible in the spectra as well. A possible origin of the additional peaks is the mixing of Raman and infrared (IR) active modes due to the reduced local symmetry,

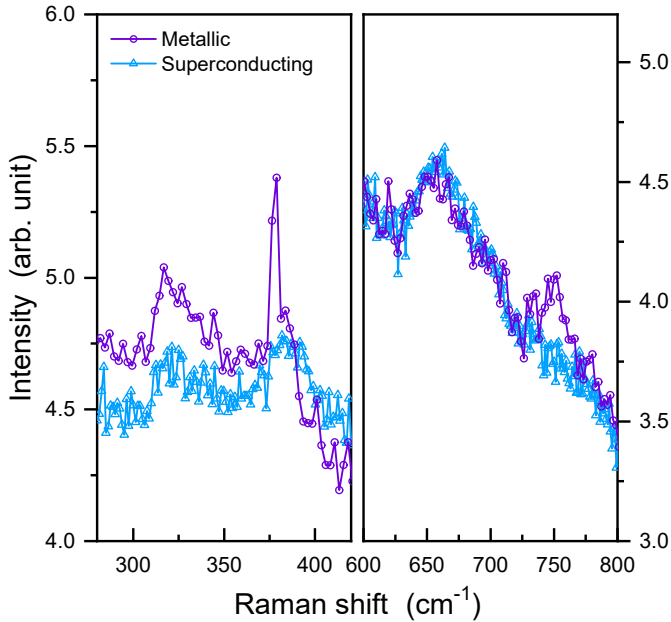


Figure 3.10: Detailed view of the spectral ranges exhibiting signatures of Ru vacancies in the Raman spectra of the metallic sample *S9* and the superconducting sample *S10*.

in which the IR-active modes can appear in the Raman spectra. Indeed, two IR active modes were observed between 300 and 400 cm^{-1} by inelastic neutron scattering [BRS+07].

In addition, when looking closely at the samples *S9* and *S10* showing metallic transport properties, one can observe faint but visible peaks at the same energies, which indicate a small concentration of Ru vacancies (Fig. 3.10). This suggests that even the best Sr_2RuO_4 thin-film samples incorporate a small number of point defects during the high temperature growth process in high vacuum. We also note small but distinct differences in the spectra of the metallic and superconducting samples: the peak at 375 cm^{-1} and its overtone at 750 cm^{-1} are visible in the spectra of sample *S9*,

but not in those of *SIO*.

3.2.5 Conclusion

In conclusion, our study has provided two spectroscopic signatures of ruthenium vacancies in SRO thin films that are not detectable with other state-of-art techniques, such as STEM and high resolution XRD. The ruthenium deficiency of the films was tuned by varying the growth temperature as well as growth technique. The resulting films exhibit widely different transport properties, ranging from insulating all the way to superconducting behavior. In ruthenium deficient SRO, the O K-edge XAS exhibits a considerable suppression of the spectral weight in the pre-peak structures stemming from Ru-O hybridization. We also used confocal micro-Raman spectroscopy to characterize additional phonon modes arising from point defects, following related observations on bulk materials [ABI+99; LRS+98] and copper oxide thin films [KCL+17]. Our spectroscopic results call for further quantitative analyses on ruthenium vacancies in SRO thin films using techniques like the Rutherford backscattering measurement, which can calibrate the correlation between the spectroscopic features and the density of ruthenium vacancies. We expect that our results will be helpful in guiding the preparation of ruthenate thin films for fundamental physics and applications in oxide electronics.

TAILORING MAGNETIC PROPERTIES VIA DEFECT CONTROL

This chapter presents publication manuscripts that are published.
They are reprinted with the licenses from publishers.

(1) Gideok Kim *et al.*, *Physical Review Materials* **3**, 084420 (2019) [[KSH+19a](#)]

(2) Gideok Kim *et al.*, *submitted* (2020)

4.1 Tunable perpendicular exchange bias in oxide heterostructures

4.1.1 Abstract

The exchange bias effect is an essential component of magnetic memory and spintronic devices. Whereas recent research has shown that anisotropies perpendicular to the device plane provide superior stability against thermal noise, it has proven remarkably difficult to realize perpendicular exchange bias in thin-film structures. Here we demonstrate a strong perpendicular exchange bias effect in heterostructures of the quasi-two-dimensional canted antiferromagnet La_2CuO_4 and ferromagnetic $(\text{La,Sr})\text{MnO}_3$ synthesized by ozone-assisted molecular beam epitaxy. The magnitude of this effect can be controlled via the doping level of the cuprate layers. Canted antiferromagnetism of layered oxides is thus a new and potentially powerful source of uniaxial anisotropy in magnetic devices.

4.1.2 Introduction

Exchange bias arises at the interface between ferromagnets and antiferromagnets, and manifests itself as a shift of the magnetic hysteresis loop in the direction opposite to the applied cooling field. Exchange-bias structures serve diverse functions in magnetic memory and spintronic devices and are of topical interest in both fundamental and applied research [ZK16]. In most cases, the exchange bias is observed when the field is applied parallel to the interface. However, recent research has focused on systems with a bias direction perpendicular to the interface, because they are less susceptible to thermal noise and particularly well suited for a large class of spintronic devices [DC17; LSR+13; MTPF01; RAR+12; ZGDM17; ZK16]. Most of these systems utilize ferromagnets with easy axes perpendicular to the interface – an uncommon situation that requires elaborate strategies to manipulate the magneto-crystalline anisotropy. Some such strategies take advantage of interfacial anisotropies in ultrathin ferromagnetic films [LSR+13; MTPF01; ZGDM17]; others use ferrimagnets including rare-earth species with large

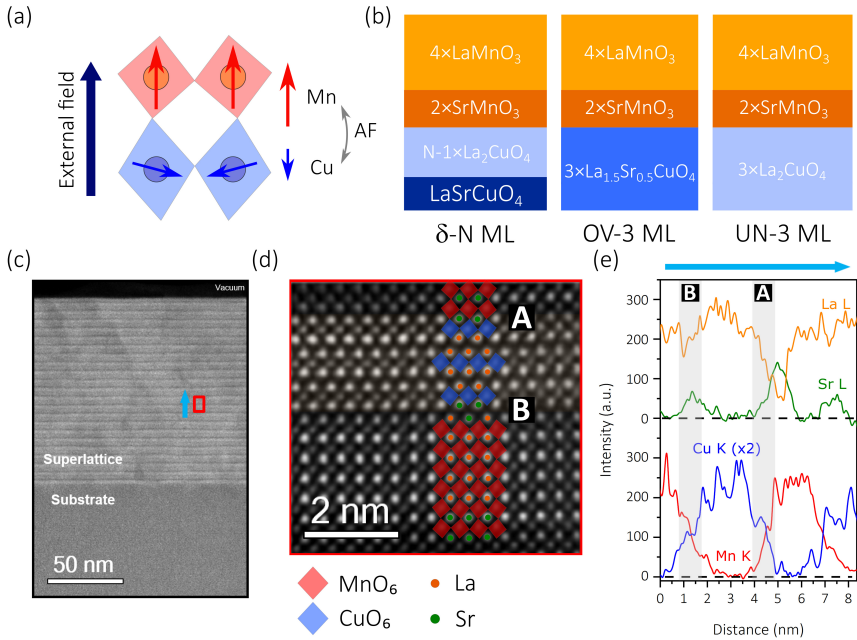


Figure 4.1: Lattice structure and chemical profile of the cuprate/manganate superlattices. (a) Schematic diagram for the out-of-plane antiferromagnetic coupling between Cu and Mn. The arrows indicate the local magnetic moments at the interface (left) and the net moments in the direction of the external field (right). (b) Supercell composition of the superlattices. (c) Low magnification STEM-HAADF image of δ -3 ML. The red box and the blue arrow indicate regions covered by panels (d) and (e), respectively. (d) High-magnification STEM-HAADF image of δ -3 ML. (e) EDXS depth profile of δ -3 ML.

single-ion anisotropies [RAR+12]. However, a simpler and more robust strategy based on the intrinsic properties of the components is desirable to design versatile devices.

Recent advances in metal-oxide heterostructures offer new perspectives for electronic devices based on collective quantum phenomena such as unconventional magnetism, multiferroicity, and superconductivity [BM14; BVB11;

CFH+07; HIK+12; YLO+10]. In particular, exchange-bias structures based on ferromagnetic manganates of composition $\text{La}_{1-y}\text{Sr}_y\text{MnO}_3$ ($0.1 \leq y \leq 0.5$) and different metal-oxide antiferromagnets have been reported [FZJ+16; GZS+12; WCY+10]. $\text{La}_{1-y}\text{Sr}_y\text{MnO}_3$ (LSMO) is a soft ferromagnet, and in thin-film form, it generally orders with magnetization direction in the substrate plane. It was recently shown, however, that perpendicular exchange bias can be induced in nanocomposite films of $\text{La}_{0.7}\text{Sr}_{0.3}\text{MnO}_3$ and antiferromagnetic LaFeO_3 with active interfaces perpendicular to the substrate plane [FZJ+16].

Here we report perpendicular exchange bias in a different oxide heterostructure system with a conventional layer architecture that does not require elaborate synthesis conditions. Instead of manipulating the easy axis of the ferromagnet, the perpendicular anisotropy in our system is generated by canted moments in the quasi-two-dimensional antiferromagnet La_2CuO_4 (LCO) that are exchange-coupled to the ferromagnetic magnetization of $\text{La}_{1-y}\text{Sr}_y\text{MnO}_3$ (Figure 4.1(a)). We also show that the magnitude of the exchange bias can be tuned via the doping level of LCO.

4.1.3 Experimental details

Superlattices were grown on LaSrAlO_4 (LSAO) (001) single-crystalline substrates (Crystal GmbH) by using the ozone-assisted ALL-MBE system (DCA Instruments). The growths were monitored by using *in situ* reflection high energy electron diffraction (RHEED). The film quality was confirmed by high-resolution x-ray diffraction and transmission electron microscopy. The full compositions of the samples are shown in table 4.1. The total film thickness varies among the samples, however its impact on the interfacial exchange interaction that induces the exchange-bias observed in our study is insignificant.

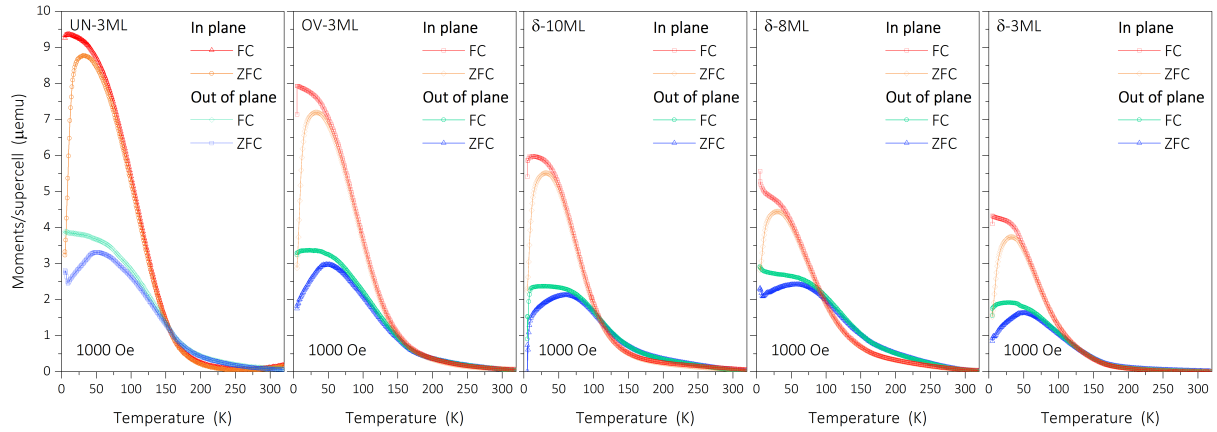


Figure 4.2: Temperature dependent magnetization curves. The data were taken in field-cooled (FC) and zero-field-cooled (ZFC) modes with a 1000 Oe field applied parallel and perpendicular to the heterostructure plane, respectively. The signal from the substrate was subtracted after the measurement, and the resulting magnetic moment was normalized by the number of supercells.

Table 4.1: List of superlattices. The number of layers is counted in units of one CuO_2 layer in $\text{La}_{2-x}\text{Sr}_x\text{CuO}_4$ (LSCO) ($\sim 6.6 \text{ \AA}$) and pseudo-cubic unitcell of manganates (One manganese atom per cell, $\sim 3.9 \text{ \AA}$).

Sample	Composition	Substrate
δ -2ML	$9 \times [1 \times \text{LSCO}(x=1) + 1 \times \text{LCO} + 2 \times \text{SMO} + 4 \times \text{LMO}]$	LSAO (001)
δ -3ML	$22 \times [1 \times \text{LSCO}(x=1) + 2 \times \text{LCO} + 2 \times \text{SMO} + 4 \times \text{LMO}]$	LSAO (001)
δ -5ML	$10 \times [1 \times \text{LSCO}(x=1) + 4 \times \text{LCO} + 2 \times \text{SMO} + 4 \times \text{LMO}]$	LSAO (001)
δ -8ML	$22 \times [1 \times \text{LSCO}(x=1) + 7 \times \text{LCO} + 2 \times \text{SMO} + 4 \times \text{LMO}]$	LSAO (001)
δ -10ML	$22 \times [1 \times \text{LSCO}(x=1) + 9 \times \text{LCO} + 2 \times \text{SMO} + 4 \times \text{LMO}]$	LSAO (001)
UN-3ML	$9 \times [3 \times \text{LCO} + 2 \times \text{SMO} + 4 \times \text{LMO}]$	LSAO (001)
OV-3ML	$9 \times [3 \times \text{LSCO}(x=0.5) + 2 \times \text{SMO} + 4 \times \text{LMO}]$	LSAO (001)
LMO/SMO	$10 \times [2 \times \text{SMO} + 4 \times \text{LMO}]$	STO (001)

For scanning transmission electron microscopy (STEM), we prepared representative cross-sectional electron transparent specimens by employing the standard specimen preparation procedure including mechanical grinding, tripod wedge polishing, and argon ion milling. After the specimens were thinned down to $\sim 10 \mu\text{m}$ by tripod polishing, argon ion beam milling, for which a precision ion polishing system (PIPS II, Model 695) was used at low temperature, was carried out until reaching electron transparency. For all STEM analyses, a probe-aberration-corrected JEOL JEM-ARM200F equipped with a cold field-emission electron source, a probe Cs-corrector (DCOR, CEOS GmbH), a large solid-angle JEOL Centurio SDD-type energy-dispersive X-ray spectroscopy (EDXS) detector was used. STEM image and EDXS analyses were performed at probe semi-convergence angles of 20 mrad and 28 mrad, resulting in probe sizes of 0.8 and 1.0 , respectively. The collection angle range for high-angle annular dark-field (HAADF) images was 75-310 mrad and in order to decrease the noise level, the images were processed with a principal component analysis routine.

We utilized SQUID magnetometry, polarized neutron reflectometry (PNR) and X-ray magnetic circular dichroism (XMCD) for magnetic property measurements. The magnetization curves were measured using a MPMS3 magnetometer (Quantum Design Co.) with VSM mode. The PNR experiments were conducted at the angle-dispersive reflectometer NREX (neutron wavelength 0.428 nm) at FRM-II, Garching, Germany. An external magnetic field was applied parallel to the sample surface, normal to the scattering plane. XMCD experiments were performed at the BESSY II undulator beamline UE46-PGM1. The spectra were collected using both total-electron-yield and fluorescence-yield modes simultaneously. The XMCD signal is defined as $(I_+ - I_-) / (I_+ + I_-)$.

4.1.4 Results and discussion

Cuprate-manganate superlattices have been extensively investigated as a platform for interfacial reconstructions and proximity effects, for the interplay between ferromagnetism and unconventional superconductivity, and for

superconducting spintronics [BVB11]. To study the exchange-bias effect, we chose superlattices based on LCO and LaMnO₃ (LMO) because their doping levels can be accurately controlled, and because they are well suited for epitaxial integration. We used ozone-assisted layer-by-layer molecular beam epitaxy to deposit a series of Sr-doped LCO-LMO superlattices with a heterogeneous doping technique. All superlattices were prepared with identical ferromagnetic layers, 2×SrMnO₃ + 4×LaMnO₃ to reduce the Sr redistribution into the cuprate layers, and LCO layers with various densities of mobile holes, as summarized in Figure 4.1(b) [BMV+08]. In “ δ -doped” samples (δ -N ML in Figure 4.1(b)), individual monolayers of highly overdoped LSCO supply holes to N monolayers of undoped LCO [BLG+15]. Because of the chemical-potential difference between cuprates and manganates, interfacial charge transfer reduces the hole content in the cuprate layers such that the average doping level of these samples is in the “underdoped” regime close to the insulating antiferromagnet LCO, where superconductivity is absent or severely degraded. Indeed, mutual inductance measurements on δ -N ML samples show no sign of a superconducting transition (although signatures of filamentary superconductivity with $T_c \sim 20$ K were observed in resistivity measurements). For comparison, we also synthesized superlattices based on three consecutive monolayers of undoped LCO (UN-3ML) and highly overdoped, non-superconducting La_{1.5}Sr_{0.5}CuO₄ (OV-3ML), respectively.

Scanning transmission electron microscope high-angle annular dark-field (HAADF) images show alternating K₂NiF₄-type and perovskite structures with the intended periodicity (Figure 4.1(c), (d)). We observed two types of interfaces: interface A with direct Cu-O-Mn bonding that is responsible for the interfacial magnetic interaction between Cu and Mn moments, and interface B with an extra (La,Sr)-O layer that mediates the charge redistribution [CFS+06; UDS+14; WGW+18]. The STEM energy-dispersive x-ray spectroscopy line scans show short-ranged intermixing between copper and manganese at the interfaces, which extends over less than 1 nm (Figure 4.1(e)).

The onset of the ferromagnetic transition in magnetization measurements revealed Curie temperatures of ~ 170 K for all samples, consistent with prior

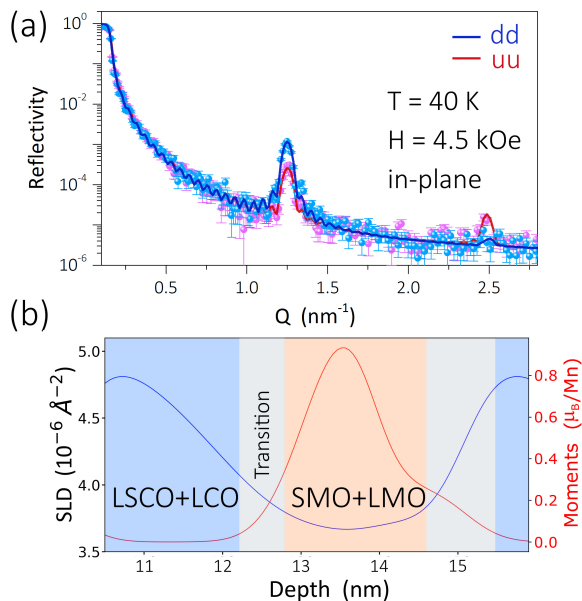


Figure 4.3: Polarized neutron reflectometry on the δ -3 ML sample. (a) Polarized neutron reflectivity curves measured with up-spin, u , and down-spin, d , neutrons at 40 K. (b) Nuclear (left axis) and magnetic (right axis) SLD depth profiles.

work on $\text{SrMnO}_3/\text{LaMnO}_3$ superlattices (Figure 4.2) [MSV+08]. Interestingly the saturation magnetization per ferromagnetic layer, $2 \times \text{SrMnO}_3 + 4 \times \text{LaMnO}_3$, varies with different types of cuprate spacers; the structure with LCO layers shows the largest magnetic moments, and chemical substitution in the LCO layers reduces the magnetization. The depth-resolved profile of the in-plane magnetic moment obtained from PNR agrees with the low magnetization in the δ -3ML sample, where the magnetic moment reaches up to $0.8 \mu_B$, that is, less than half of the value $\sim 2 \mu_B$ in optimally doped LSMO thin films (Figure 4.3) [KVK+12; YZT+15]. The origin of the reduced magnetism can be attributed to an interface effect, because the nominal compositions of the ferromagnetic layers are identical. The largely suppressed

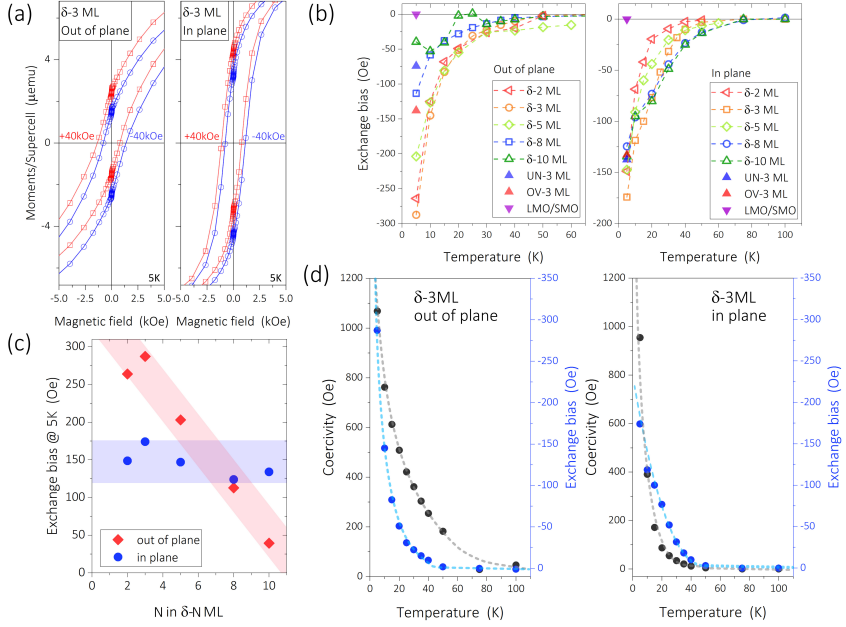


Figure 4.4: Exchange bias and coercivity. (a) Hysteresis loops measured at 5 K showing the exchange bias effect in the δ -3ML superlattice. Full curves are presented in the supplementary information. (b) Temperature dependence of H_{EB} for fields applied out of (left panel) and in (right panel) the heterostructure plane. (c) Dependence of H_{EB} on the thickness of the δ -doped cuprate layers. (d) Temperature dependence of H_{EB} and H_C in the δ -3ML sample. The external field was applied in (100)_{LSAO} and (001)_{LSAO} direction for in-plane and out-of-plane measurements respectively.

magnetization at the interface also supports the interface-derived nature of the effect (Fig. 4.3). At the interface, both epitaxial strain and charge transfer can influence the magnetic moment in LSMO [TSNE00; YGA+12]. In our case, epitaxial strain cannot be the major factor because the in plane lattice parameters of the LCO-based spacers are similar especially among samples with the same spacer thicknesses, namely δ -3ML, UN-3ML and OV-3ML. On the other hand, the strong dependence on the effective doping

level of the cuprate layers indicates that charge transfer plays the major role, where holes move from the cuprate to the manganate layers to match the chemical potential difference and reduce the magnetic moments [SBC+19].

Magnetic hysteresis loops were measured after field cooling in a static magnetic field of 40 kOe. Representative curves from sample δ -3ML clearly exhibit the characteristic exchange-bias shift along the magnetic field axis for both in-plane and out-of-plane applied fields (Figure 4.4(a)). To quantify the effect, the size of the exchange bias (H_{EB}) and the coercivity (H_C) are defined following the convention $H_{EB} = (H_{C+} + H_{C-})/2$ and $H_C = (H_{C+} - H_{C-})/2$, where H_{C+} and H_{C-} are defined as the positive and the negative H-intercepts of the M-H hysteresis loop, respectively. We found that all LCO-LMO superlattices exhibit nonzero values of H_{EB} at 5K, and that H_{EB} shows a strong temperature dependence that sets on below 50 K (Figure 4.4(b)). Notably, a superlattice without the cuprate (LMO/SMO) displays no signature of exchange bias, highlighting the crucial role of the interface between the cuprate and the manganite layers ¹.

We now focus on the difference between the evolution of H_{EB} for in-plane and out-of-plane directions (Figure 4.4(c)). The out-of-plane exchange bias, $H_{EB,OP}$, displays a strong dependence on composition, whereas the in-plane effect, $H_{EB,IP}$, shows at most a weak composition dependence. δ -N ML samples exhibit substantial anisotropies, with $H_{EB,OP} > H_{EB,IP}$. The anisotropy decreases continuously with increasing N (and hence decreasing doping level). Both the UN-3ML and the OV-3ML samples exhibit only small anisotropies. These findings suggest that the origins of the out-of-plane and in-plane exchange bias effects are distinct, and that the doping level selectively influences the effect along the surface normal direction.

Figure 4.4(d) demonstrates a related anisotropy in the coercivity, H_C , which reflects the strength of the magnetic domain-wall pinning. For in-plane magnetic fields, $H_{C,IP}$ increases markedly upon cooling below 50 K,

¹Additional evidence for the presence and robustness of exchange bias in our superlattices is presented in the supplementary materials: hysteresis curves with a wider range (Fig. S1), the presence of exchange bias after several cycles of magnetization (Fig. S2), and exchange-biased hysteresis loop measured with PNR which is less susceptible to extrinsic effects than SQUID-VSM (Fig. S3)

parallel to the onset of $H_{EB,IP}$, which is consistent with common EB systems [PAK+16]. In contrast, $H_{C,OP}$ begins to increase at much higher temperatures ($T > 100$ K), indicating an additional pinning mechanism. The unexpected pinning in the out of plane direction could also be inferred from the temperature dependent magnetization curves (Figure 4.2), where the FC curves bifurcate from the ZFC curves at higher temperatures in OP than IP suggesting enhancement of coercive field and magnetic frustration. We could find the origin of the unexpected enhancement of $H_{C,OP}$ at higher temperatures from the magnetic coupling of the ferromagnetic layer to antiferromagnetic interface layer [SUN05], which was reported by prior studies on cuprate/manganate heterostructures [CFS+06; LGP+14; UDS+14].

Since neither bulk LSMO nor thin-film structures composed solely of manganates exhibit the exchange bias effect, it must be ascribed to the interaction between Mn and Cu magnetic moments across the interface (Figure 4.1(a)). Interfacial exchange interactions in cuprate-manganate heterostructures have been the subject of prior work with XMCD, an element-specific probe that addresses Mn and Cu moments separately [CFS+06; UDS+14]. Prior XMCD measurements revealed a polarization of the Cu spins, which sets on gradually below the Curie temperature because the antiferromagnetic Cu-Mn interaction is weaker than the ferromagnetic Mn-Mn coupling. Following our observation of a highly anisotropic exchange bias and coercivity, we have carried out Cu- and Mn-XMCD experiments on the δ -3ML sample that shows the largest anisotropy (Figure 4.5). For magnetic field applied perpendicular to the substrate, the Cu-XMCD data show that the Cu spins are oriented opposite to the field for low H and switch to a parallel orientation for $H < 4.5$ kOe (Figure 4.5(a)), reflecting antiferromagnetic Cu-Mn interactions of moderate strength in agreement with prior work [CFS+06; LGP+14; UDS+14]. Experiments in which a magnetic field of 50 kOe was applied in different directions with respect to the substrate plane demonstrate the out-of-plane character of the magnetic moments at the Cu site (Fig. 4.5(b)). The Mn-XMCD spectra in the inset of Fig. 4.5(b) show that the Mn magnetic moments at $H = 50$ kOe are at most weakly dependent on the magnetic field direction, as expected in view of

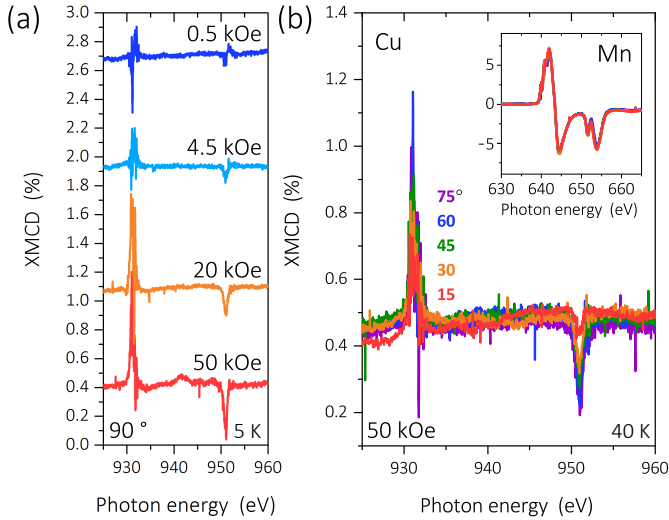


Figure 4.5: XMCD measurements on the δ -3ML superlattice in total-electron-yield mode. The current to the ground was measured as a function of incident photon energy across the Cu and Mn $L_{3,2}$ absorption edges for left- and right-circularly polarized x-rays. The magnetization of the probed sublattice is proportional to the amplitude of the XMCD signal. (a) Magnetic field dependence of the Cu-XMCD at 5 K. The magnetic field was applied perpendicular to the substrate plane. (b) Cu-XMCD spectra at 40 K in a magnetic field of 50 kOe applied at different angles to the substrate plane (see the legend). The inset shows Mn-XMCD spectra that are angle-independent.

the weak spin-space anisotropy of LMO.

These findings suggest that the large perpendicular exchange bias and the enhanced out-of-plane coercivity originate in the perpendicular magnetization of the cuprate layers, which is exchange-coupled to the ferromagnetic magnetization of the manganese layers via interfacial interactions. A canted magnetization has indeed been observed in the CuO_2 sheets of antiferromagnetic bulk LCO [KBB+92; KBT+88; RUP+06]. This effect arises from a cooperative tilt rotation of the CuO_6 octahedra in the crystal structure,

which creates an inversion-asymmetric Cu-O-Cu exchange bond and actuates a Dzyaloshinskii-Moriya interaction between the Cu spins. The canted antiferromagnetism in LCO is highly sensitive to the dopant concentration. In undoped LCO, the direction of the canted moment alternates between CuO_2 layers, and a net canted magnetization perpendicular to the antiferromagnetic layers only appears at a metamagnetic transition in magnetic fields exceeding 10 T (100 kOe) [RUP+06]. The high magnetic field required to reverse the direction of the canted moment is thus presumably responsible for the weak perpendicular exchange bias in the UN-3ML superlattice. The modest magnetic fields used for our experiments were not sufficiently strong to reverse canted moment directions during field cooling, so as to produce interfacial spin arrangements favorable for the perpendicular exchange bias. In doped LCO, hole doping induces a spin glass phase with short-range antiferromagnetic order and rapidly reduces the magnetic field scale for the metamagnetic transition, allowing our field cooling procedures to effectively exchange-bias the magnetic layers. In overdoped bulk LCO, the magnetic short-range order and the canted magnetization vanish entirely [KBB+92]. The onset temperature of spin-glass correlations is comparable to the onset of the perpendicular exchange bias in our superlattices (50 K). The anomalous exchange bias can thus be attributed to interfacial moments in the spin glass, in analogy to previously reported exchange bias effects in bilayers and core/shell nanoparticles composed of ferromagnets and spin glasses [AAM+07; PAK+16]. The phase behavior of bulk LCO thus provides a natural explanation for the maximal $H_{EB,OP}$ in the δ -3 ML sample with underdoped LCO layers, the decrease of the anomalous perpendicular exchange bias with increasing doping (Fig. 4.4(c)), and its absence in the OV-3 ML sample.

4.1.5 Conclusion

In conclusion, we have shown that quasi-two-dimensional canted antiferromagnetism is a potent source of perpendicular exchange bias in metal-oxide heterostructures. The Dzyaloshinskii-Moriya interaction responsible for the

perpendicular magnetic moments is rooted in the bulk crystal structure and is therefore more robust than magnetic anisotropies generated solely by the interfacial inversion asymmetry. Quasi-two-dimensional antiferromagnets are quite common in metal-oxides and can be readily integrated into conventional multilayer structures, without the need to create elaborate composite architectures. Finally, we have shown that the magnitude of the perpendicular exchange bias can be systematically tuned by adjusting the doping level of the antiferromagnet through an atomically engineered δ -doping scheme. Canted antiferromagnetism of layered oxides is thus a new and potentially powerful source of uniaxial anisotropy, and opens up new perspectives for spin-electronic devices that take advantage of collective quantum phenomena such as superconductivity and multiferroicity.

4.2 Inhomogeneous ferromagnetism mimics signatures of the topological Hall effect in SrRuO₃ films

4.2.1 Abstract

Topological transport phenomena in magnetic materials are a major topic of current condensed matter research. One of the most widely studied phenomena is the “topological Hall effect” (THE), which is generated via spin-orbit interactions between conduction electrons and topological spin textures such as skyrmions. We report a comprehensive set of Hall-effect and magnetization measurements on epitaxial films of the prototypical ferromagnetic metal SrRuO₃ whose magnetic and transport properties were systematically modulated by varying the concentration of Ru vacancies. We observe Hall-effect anomalies that closely resemble signatures of the THE, but a quantitative analysis demonstrates that they result from inhomogeneities in the ferromagnetic magnetization caused by a non-random distribution of Ru vacancies. As such inhomogeneities are difficult to avoid and are rarely characterized independently, our results call into question the identification of topological spin textures in numerous prior transport studies of quantum materials, heterostructures, and devices. Firm conclusions regarding the

presence of such textures must meet stringent conditions such as probes that couple directly to the non-collinear magnetization on the atomic scale.

4.2.2 Main text

Ferromagnetic and nearly ferromagnetic metals are archetypal platforms for the investigation of topological phenomena in quantum materials. The “anomalous Hall effect” (AHE) in a metallic ferromagnet is proportional to the ferromagnetic magnetization, with a coefficient that depends on the Berry phase curvature in momentum space and thus contains information on the topological properties of its band structure [Hal04; NSO+10]. More recently, an additional contribution (termed “topological Hall effect”, THE) was discovered in nearly ferromagnetic metals with superstructures of real-space topological defects, namely skyrmions [NPB+09; RBP06]. This contribution arises when conduction electrons accumulate a Berry phase upon traversing the skyrmion lattice, and manifests itself as a sharp enhancement of the Hall signal as the skyrmion-lattice phase is entered by varying the temperature or the external field.

The AHE was initially discovered and explored in bulk ferromagnets, but has become a standard diagnostic of ferromagnetism in device structures where direct measurements of the magnetization are impractical. Likewise the THE, which was originally established in bulk compounds with skyrmion-lattice phases that had been extensively characterized by neutron diffraction, has recently been widely used as a fingerprint of skyrmions in thin films and heterostructures where direct measurements of the non-collinear magnetization could not be performed [BSH+19; GWX+19; LST+20; MAB+19; MOY+16; OMO+18; QLL+19; SKC+20; VWS+19; WDL+19; WFK+18; ZBEL19; ZDB+20]. Information about topological spin textures in such systems is important in view of the emerging use of skyrmions in data processing and storage devices (“skyrmionics”) [BCE+20]. However, the indirect identification of topological structures based on THE experiments has been called into question, because sharp enhancements of the Hall effect in specific regimes of temperature and magnetic field can also arise from

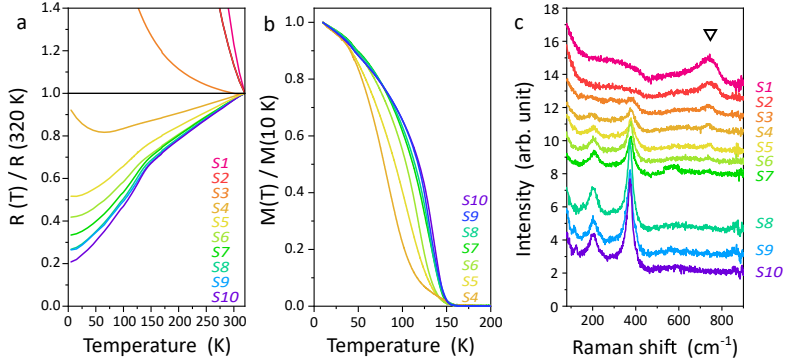


Figure 4.6: **Physical properties of SrRuO₃ films with varying Ru vacancy concentration.** **a**, Normalized resistance curves. **b**, Normalized field-cooled magnetization measurement at 0.01 T. Magnetization curves of Sample S1-3 are not plotted here due to the absence of ferromagnetic moments. The raw data without normalization are presented in the Supplemental Material. **c**, Polarized Raman spectra with $zXXz$ configuration. The triangle indicates the Raman-active mode induced by Ru vacancies.

different mechanisms, including electronic inhomogeneity due to variations in materials composition and superposition of Hall signals from different materials and interfaces in heterostructures [Ger18; KMKS18; KMS20].

With this motivation, we have carried out a comprehensive set of measurements of the Hall effect and magnetization in epitaxial films of a single model material, the ferromagnetic metal SrRuO₃ (SRO). The AHE of bulk SRO is positive below its Curie temperature $T_C = 165$ K, but exhibits a sign reversal upon cooling below $T_S \sim 120$ K [KKS+12]. This behavior can be attributed to the confluence of an intrinsic contribution from the Berry curvature of the band dispersions and an extrinsic contribution due to spin-orbit scattering from defects. In thin-film form, SRO is widely employed as a metallic electrode in oxide electronics and as a ferromagnetic component of spintronic devices [KKS+12]. Due to inversion-symmetry breaking at interfaces and/or interfacial exchange interactions, the magnetic structure of SRO can become non-collinear in thin-film structures [KVK+12], and theoretical work has

led to the prediction of topological defects and defect superstructures in this situation [KN17; MDO19]. Hall-effect measurements both on SRO films and on heterostructures comprising SRO layers have indeed uncovered sharp enhancements of the Hall signal akin to those of classical skyrmion-lattice compounds, which were interpreted as evidence for skyrmions generated by Dzyalonskii-Moriya interactions at the substrate interface and/or competing exchange interactions at interfaces with other magnetic materials [MOY+16; OMO+18].

Recently, however, an alternative interpretation was proposed based on the superposition of different AHE signals due to spatial inhomogeneity [KMKS18; KMS20]. Whereas a model based on this hypothesis yielded a good description of transport data on ultrathin SRO films, a thorough assessment of this scenario requires information on the ferromagnetic magnetization which controls the magnitude of the AHE. We performed our measurements on thick films where interfacial effects are negligible and where the ferromagnetic order parameter and its inhomogeneity could be quantitatively characterized by magnetometry. An elementary model of the AHE based on this information yields a quantitative description of the Hall-effect maxima purely based on inhomogeneous ferromagnetism.

We used reactive sputtering to grow epitaxial SRO films on (100)-oriented LSAT substrates (see Methods for details and Supplemental Materials for structural characterization). Due to the high volatility of ruthenium oxides, SRO films grown from stoichiometric targets contain Ru vacancies that are known to reduce the electrical conductivity and the Curie temperature [BHA+19; DCK+04; KKS+12; NLR+18; SBDD15; SKV+07]. We modified the density of Ru vacancies and the physical properties by adding Ru metal to the target and by varying the growth temperature. Following recent work on Sr_2RuO_4 films [KSH+19b], we monitored the intensity of a Raman-active mode attributable to Ru vacancies and found that it is inversely related to the RRR, indicating that Ru vacancies are the major source of scattering of the conduction electrons (Fig. 4.6c).

Figure 4.6a shows the temperature (T) dependence of the longitudinal electrical resistance, R_{xx} , of the samples prepared in this way. The residual

resistance ratio (RRR), $R_{xx}(T = 320K)/R_{xx}(T \rightarrow 0)$, reflects the density of Ru vacancies. The samples were labeled S1 – 10, with higher numbers indicating higher RRRs. Samples S1 – 3 show semiconductor-like electrical transport with diverging R_{xx} as $T \rightarrow 0$. Structural analysis shows that metallic samples with low and moderate Ru vacancy densities only exhibit the SRO phase, whereas electron microscopy data on insulating samples with higher vacancy content show possible evidence of secondary phase formation (see Supplement).

In Figure 4.7, we present the Hall resistance, R_{xy} , as a function of external magnetic field, H , for the metallic samples. R_{xy} comprises two major contributions: the AHE, which is proportional to the ferromagnetic magnetization and thus follows its hysteresis loop [NSO+10], and the ordinary Hall effect, which is responsible for the linear dependence of $R_{xy}(H)$ persisting above the coercive field H_C . The sign of the anomalous Hall resistance ($R_{xy,AHE}$) can be identified from the direction of jumps in the ascending branches of the hysteresis loops. In agreement with the literature, the AHE of nearly stoichiometric samples is positive (negative) for T larger (smaller) than $T_S \sim 110$ K, respectively. Our synthesis method allowed us to vary T_S over an exceptionally wide range (inset to Fig. 4.7e). $R_{xy,AHE}$ and R_{xx} of all samples (including the ones with severely degraded RRR and T_S) can be collapsed onto a single scaling plot (Fig. 4.7e), which indicates the dominance of the intrinsic (extrinsic) contributions to the AHE at low (high) temperatures [HKK+13; HSS+11]. In the metallic sample with the lowest RRR, S4, the impurity contribution with positive $R_{xy,AHE}$ prevails at all temperatures so that $R_{xy,AHE}$ does not change sign at all.

The hysteresis loops of $R_{xy,AHE}$ in all metallic samples (except S4) exhibit maxima for $H \sim H_C$ and $T \sim T_S$ (Fig. 4.7a-d). Related anomalies of the Hall signal have previously been reported for SRO films, SRO heterostructures, and heterostructures of different compounds, and have been widely attributed to the topological Hall effect [BSH+19; GWX+19; LST+20; MAB+19; MOY+16; OMO+18; QLL+19; SKC+20; WFK+18; ZBEL19; ZDB+20]. In our samples, however, the amplitude and temperature range of these maxima exhibit an extreme variation with defect concentration. In the

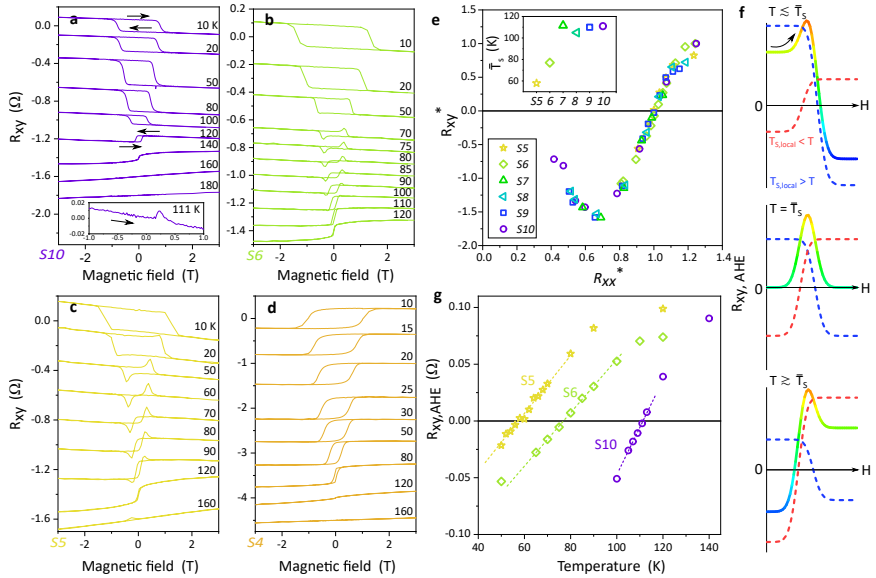


Figure 4.7: Summary of Hall measurements. **a-d**, Hall resistance curves. Curves are shifted in the y -direction for better visibility. The numbers in plots indicate the measurement temperatures in Kelvin. The black arrows indicate the direction of magnetic field ramp. The Hall measurements on the other samples are presented in the Supplemental Material. The inset to **a** shows the magnified view of the ascending branch. **e**, Scaling behavior of the anomalous Hall resistance. The inset shows the sample dependence of T_S . Here, R_{xy}^* is $R_{xy,AHE}(T)$ normalized by its maximum value, and $R_{xx}^* = R_{xx}(T)/R_{xx}(T_S)$ [HSS+11]. **g**, Temperature dependence of $R_{xy,AHE}$. Dashed lines are the results of linear fit. **f**, Schematic diagram describing the composite AHE that mimics the THE.

most stoichiometric sample S10, the maxima are subtle and observable only over a range of a few K, analogous to the THE in skyrmion-lattice compounds such as MnSi [NPB+09]. In our sample S5 with a high Ru vacancy content, on the other hand, the maxima are much more pronounced and extend over a temperature range of more than 70 K.

This finding is difficult to reconcile with the THE model and instead sup-

ports a scenario that attributes the Hall-effect maxima to inhomogeneous ferromagnetism generated by unavoidable inhomogeneities in the distribution of Ru vacancies. In this scenario, the maxima arise for temperatures in the vicinity of the macroscopically averaged \bar{T}_S , when the current traverses regions with positive and negative $R_{xy,AHE}$ and different coercive fields. As an example, we consider the ascending branch of the hysteresis curve at a temperature $T \gtrsim \bar{T}_S$ (Fig. 4.7f). In low magnetic fields, the saturated M is antiparallel to the external field, and the overall $R_{xy,AHE}$ signal is reduced through a partial cancellation of positive and negative contributions from regions with $T_S < T$ and $T_S > T$, respectively. Regions with lower T_S have higher defect densities and correspondingly lower H_C . As H increases, the magnetization of these regions is reversed when the local H_C is exceeded, while the magnetization of more stoichiometric domains with higher H_C and negative $R_{xy,AHE}$ remains antiparallel to H . In this way, the partial cancellation is lifted and the overall $R_{xy,AHE}$ is enhanced. When H exceeds H_C of the more stoichiometric regions, the macroscopically averaged AHE signal decreases again.

At the heart of this picture is the inhomogeneous distribution of the ferromagnetic order parameter and coercive field, which was not available in prior work because the magnetization of the thin SRO overlayers could not be separated from the diamagnetic contribution of the substrates. Indirect information about these quantities was obtained from the longitudinal magnetoresistance [KMKS18]. The $R_{xx}(T)$ traces of SRO indeed exhibit kinks at the ferromagnetic transition temperature T_C , and signatures of inhomogeneous broadening are observed in samples with lower RRR (Fig. 4.6a), but the degree of broadening is difficult to quantify because the strength of the kinks also decreases with increasing RRR. In the presence of external magnetic fields, these difficulties are further compounded by incomplete knowledge of the mechanisms underlying the longitudinal magnetoresistance and its relation to the magnetization. Moreover, since the films investigated in previous experiments were only 3-5 nm thick and the thickness was used to modulate the degree of inhomogeneity, the influence of the surface and the substrate interface could not be assessed.

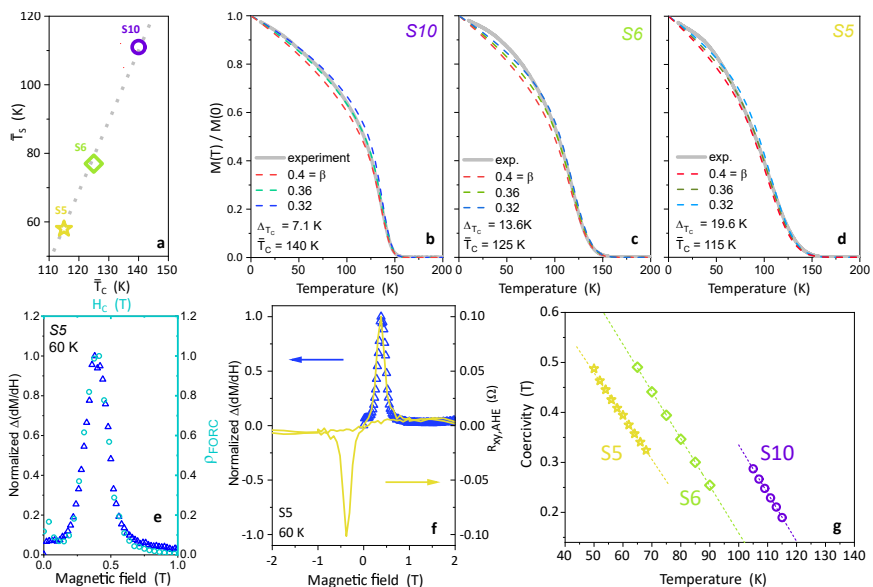


Figure 4.8: Summary of magnetometry measurements. **a**, Correlation between T_S and T_C . The line is a guide to the eye. **b-d**, $M(T, H \rightarrow 0)$ and modeled curves. The curves were computed using Gaussian averages with the parameters in the legends (see text). β is the critical exponent in the power law, $(1 - T/T_C)^\beta$. **e**, Comparison between the FORC distribution ρ_{FORC} (see Methods) and the derivative of the magnetic hysteresis curve of sample S5 at $T = 60$ K. Both were normalized to unity for comparison. **f**, Comparison between the distribution of H_C and the maximum in AHE. **g**, Coercivity obtained from Gaussian fits the magnetometry measurements. Dashed lines are results of linear fits.

To address this challenge, we grew our films with thicknesses of 25-30 nm to enable accurate measurements of the ferromagnetic magnetization $M(T, H)$ – a thermodynamic quantity that contains all of the information required for a definitive test of the inhomogeneity model. The Curie temperature T_C measured by magnetometry decreases with increasing Ru vacancy content, in lockstep with the temperature at which the AHE changes sign (Fig. 4.8a). This indicates that scattering of conduction electrons from

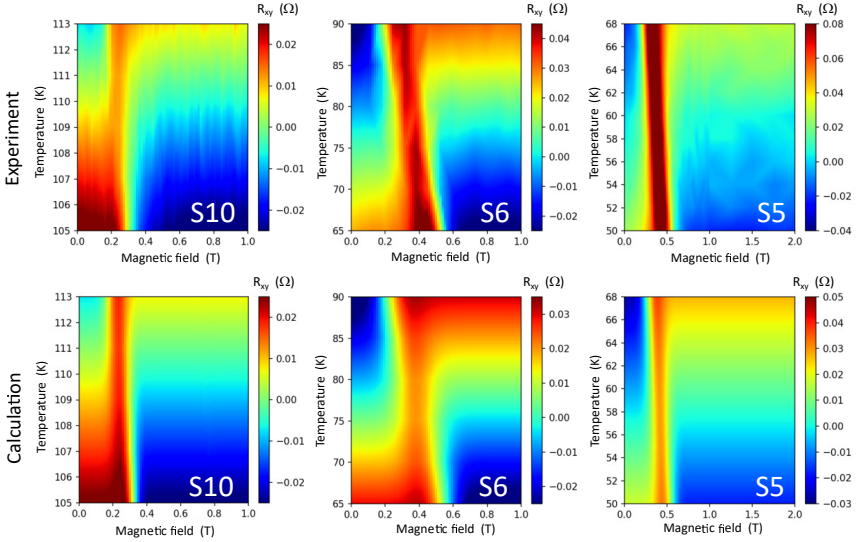


Figure 4.9: **Impact of inhomogeneity on the Anomalous Hall Effect.** Comparison between the experimental and calculated anomalous Hall resistance curves in the ascending branches of the hysteresis loops of samples S10, S6, and S5.

defects introduced by Ru vacancies is the major source of degradation of ferromagnetic order, as expected for an itinerant-electron ferromagnet such as SRO. The T -dependent ferromagnetic order parameter shows unmistakable manifestations of rounding due to an inhomogeneous spread of Curie temperatures (Fig. 4.6b). The degree of broadening can be accurately quantified by fitting $M(T, H \rightarrow 0)$ to a power law folded with a Gaussian T_C -distribution, and the results are presented in Fig. 4.8b-d. (As expected, deviations from the power law are apparent at low T , but choosing different functional forms of $M(T)$ does not change the result significantly.) The width of this distribution, ΔT_C , increases rapidly with defect concentration, in close analogy to the temperature range of the Hall-effect maxima and in qualitative agreement with the inhomogeneity scenario for the Hall-effect maxima.

According to this picture, the magnetic-field range of the Hall-effect maxima is determined by the distribution of coercive fields, ΔH_C , across a given sample (see supplement). Following standard practice, we have extracted ΔH_C from minor hysteresis loops with varying reversal fields. Figure 4.8e shows the outcome of this “first-order reversal curve (FORC)” analysis for a representative sample, along with the field derivative of $M(H)$. The quantitative agreement between both profiles (Fig. 4.8e) confirms that the broadening of the hysteresis curves indeed originates from an inhomogeneous H_C distribution. In Fig. 4.8f we also compare the width of this distribution to the width of the Hall-effect maxima measured on the same sample at the same temperature. The excellent agreement provides further strong support for the inhomogeneity scenario.

The comprehensive set of magnetization data enabled us to devise a quantitative phenomenological model for the Hall-effect maxima based purely on the conventional understanding of the AHE. Whereas we have obtained most of the essential information from our $M(T, H)$ measurements, the distribution of T_S is a transport quantity that cannot be directly extracted from the magnetization measurements. However, our observation that scattering from Ru vacancies depresses the macroscopically averaged \bar{T}_S and \bar{T}_C at nearly identical rates implies that $\Delta T_S \sim \Delta T_C$ (Fig. 4.8a). We can thus write

$$\bar{R}_{xy,AHE}(H; T) = \langle A(T_S; T) \cdot M(H, H_C; T) \rangle_{T_S, H_C}$$

where $\langle \dots \rangle_{T_S, H_C}$ is a bivariate Gaussian average over T_S and H_C (see Methods for details). In computing these averages, we take advantage of the observations that $\bar{A} = \alpha_A(T - \bar{T}_S)$ (Fig. 4.7g) and $\bar{H}_C = \alpha_C T - \beta_C$ (Fig. 4.8g) in the relevant range of temperatures, with coefficients that vary only weakly between samples with comparable \bar{T}_C , and make the straightforward assumption that these relations also hold for regions with different T_S and T_C traversed by the Hall current in any given sample.

Figure 4.9 shows the outcome of this analysis for three representative samples with widely varying amplitude and temperature range of the Hall-effect maxima. The agreement between the measured and calculated $R_{xy,AHE}$ is

excellent, which is remarkable because all parameters were fixed by independent magnetization measurements. Interestingly *S4*, the most inhomogeneous among the ferromagnetic metallic samples, does not exhibit Hall-effect maxima (Fig. 4.7d) – again in agreement with the inhomogeneity scenario which relies on the superposition of AHE contributions with different signs.

We thus conclude that the Hall-effect maxima in our SRO films originate from inhomogeneous ferromagnetism. Since inhomogeneity due to deviations from stoichiometry – including particularly Ru vacancies – is unavoidable in thin-film deposition of SRO and other ruthenates, we suggest that this scenario should be adopted as the default interpretation of Hall-effect maxima in SRO films and heterostructures, and that prior claims of the THE in such structures should be revisited.

Our results on a well-characterized model compound show in an exemplary fashion how Hall-effect maxima can arise from the superposition of positive and negative AHE signals in conjunction with inhomogeneous ferromagnetism. Whereas the presence of two contributions to the AHE with opposite signs is rare for a single phase-pure compound, there are multiple routes towards related situations in heterostructures, multilayers, and composites of different materials and stoichiometries. For instance, AHE contributions of opposite sign can arise through anti-parallel alignment of the magnetization directions of two ferromagnets in a heterostructure, even if the signs of the AHE in the individual compounds are identical. This situation was recently described in heterostructures of elemental ferromagnets [XZL+10], but deserves careful consideration also for more complex systems where multiple spin systems with non-collinear alignment often arise due to interfacial effects. The sign of the AHE can also change as a function of composition, as recently demonstrated for binary ferromagnetic alloys [SJZ+16]. This route towards coexisting positive and negative AHE contributions is particularly relevant for complex oxides – including manganates – where compositional variations and associated phase separation are widely observed and difficult to avoid [MYD99]. In oxide heterostructures, such variations generically occur as a consequence of charge transfer at interfaces.

In view of these findings and considerations, we suggest that the widely

practiced identification of topological spin textures based on Hall-effect maxima is untenable. We note that magnetic force microscopy measurements showing a patchy domain structure, which are often cited in support of the skyrmion interpretation, can be equally well described as small ferromagnetic domains [MAB+19; VWS+19; WFK+18]. Discriminating between both pictures requires detailed information about non-collinearity of the magnetization on the atomic scale. Experimental methods that are capable of probing the magnetization in thin-film structures with sufficient sensitivity and resolution include Lorentz microscopy [YLO+10], coherent x-ray scattering [LBZ+19], and diamond quantum sensors [DCS+18].

4.2.3 Methods

Sample preparation and characterization

Thin films were grown on $(\text{LaAlO}_3)_{0.3}$ - $(\text{SrAl}_{0.5}\text{Ta}_{0.5}\text{O}_3)_{0.7}$ (LSAT) (001) single-crystalline substrates (CrysTec GmbH) using either a reactive sputtering system developed at the Max Planck Institute for Solid State Research. For reactive sputtering, argon and oxygen gas were supplied via a mass flow controller. The pressures P_{O_2} and P_{total} were 50 and 100 mTorr, respectively. Substrates were glued with a platinum paste to pure nickel blocks and heated with an infrared laser. The substrate temperature was monitored using a radiative pyrometer using the emissivity of $\epsilon_{\text{LSAT}}=0.92$. The structural quality of the films was confirmed by high-resolution X-ray diffraction (XRD) with a Cu K- α source ($\lambda \sim 1.5406 \text{ \AA}$) and by transmission electron microscopy. All the samples investigated in this study are listed in table 4.2.

Confocal Raman spectroscopy

The Raman spectra were measured with a Jobin-Yvon LabRam HR800 spectrometer (Horiba Co.) combined with a dedicated confocal microscope. The short depth of focus allows measurements of films with thicknesses of ~ 10 nm. The samples were illuminated with a He-Ne laser with wavelength 632.8 nm (red), and the scattered light was collected from the sample surface with a $100\times$ long working distance objective lens. The experiments were performed in backscattering geometry with (a,b) -axis polarized light

Table 4.2: List of samples. The samples are listed in order of their residual resistivity ratios. A sample labeled as weakly metallic shows a resistivity minimum as a function of temperature. Sr214 and Ru stand for pressed polycrystalline Sr_2RuO_4 and Ru metal targets, respectively. The last column indicates whether the ground state is paramagnetic (PM) or ferromagnetic (FM).

Sample	Transport	T_{growth} (°C)	Target	Magn.
S1	Insulating	440	Sr214	PM
S2	Insulating	440	Sr214+Ru	PM
S3	Insulating	530	Sr214	PM
S4	Weakly metallic	600	Sr214	FM
S5	Metallic	530	Sr214+Ru	FM
S6	Metallic	600	Sr214+Ru	FM
S7	Metallic	700	Sr214	FM
S8	Metallic	700	Sr214 + Ru	FM
S9	Metallic	770	Sr214	FM
S10	Metallic	770	Sr214+Ru	FM

propagating along the crystallographic c -axis, which is denoted as $z(XX)\bar{z}$ in Porto's notation. SRO has a space group $Pnma$ that has a lower symmetry than the simple perovskite structure ($Pm\bar{3}m$). As a result of low crystal symmetry, SRO has 24 Raman-active phonon modes, $7A_g + 5B_{1g} + 7B_{2g} + 5B_{3g}$, according to the group theory analysis. The measurement was restricted by the experimental setup and the shape of thin film samples to the $z(XX)\bar{z}$ geometry, in which the propagation of light is parallel to the surface normal, and the polarization of the light is parallel to the Ru-O bonding direction. In this geometry we could study phonon modes with $A_{1g} + B_{1g}$ symmetry.

Electrical transport measurement

The electric resistance and Hall measurements were carried out using a Physical Property Measurement System Quantum Design Co.). To implement the van der Pauw geometry, Pt metallic contacts were sputtered on four corners of square shaped samples (5 mm \times 5 mm).

Magnetization measurements

We utilized SQUID magnetometry to measure the magnetic properties. The magnetization curves were measured using a Magnetic Property Measurement System (MPMS, Quantum Design Co.) in the VSM mode.

The first order reversal curves were measured using a MPMS in the DC mode. The ρ_{FORC} was calculated using the following standard FORC formula:

$$\rho_{FORC}(H, H_r) = -\frac{1}{2} \frac{\partial^2 M_{FORC}}{\partial H \partial H_r}$$

The details of magnetic phase distribution analyses are presented in the Supplemental Material.

Modeling of the anomalous Hall effect

We averaged the AHE over regions with different T_S and H_C as follows:

$$R_{xy,AHE}(H; T) = \int \int \alpha_A(T - T_S)[2F_{step}(H - H_C) - 1] g(T_S, H_C) dT_S dH_C$$

where F_{step} is the Heaviside step function, g is the bivariate Gaussian function

$$g(T_S, H_C) = \frac{1}{2\pi \Delta_{T_S} \Delta_{H_C} \sqrt{(1 - \rho^2)}} \exp\left[-\frac{1}{2(1 - \rho^2)} \times \left(\frac{(T_S - \bar{T}_S)^2}{\Delta_{T_S}^2} + \frac{(H_C - \bar{H}_C)^2}{\Delta_{H_C}^2} - \frac{2\rho(T_S - \bar{T}_S)(H_C - \bar{H}_C)}{\Delta_{T_S} \Delta_{H_C}}\right)\right]$$

and the correlation coefficient ρ is fixed to 0.75 in all calculations due to the strong correlation between H_C and T_S . The T -linear dependence of AHE and H_C near \bar{T}_S (Fig. 4.7g, 4.8g) simplifies the calculation. All coefficients used here are summarized in the Supplemental Material.

CHAPTER 5

OVERCOMING THE SOLUBILITY LIMIT VIA EPITAXIAL STABILIZATION

This chapter presents a publication manuscript in preparation.

(1) Gideok Kim *et al.*, *in preparation* (2020)

5.1 Persistent superconductivity in highly overdoped cuprates via minimizing the dopant-host radii mismatch

5.1.1 Abstract

One of the greatest challenges in studies of cuprate superconductors is the separation of chemical complications from the intrinsic physical properties on synthetic compounds. The dopant-host radii mismatch (DHRM) is a topical subject among various chemical complications, because of its influence on the superconducting properties such as the transition temperature and the superfluid density in the overdoped regime. Here we introduce a system with minimized DHRM: Ca-doped La_2CuO_4 thin films, the synthesis of which has been prohibited by the limited solubility in bulk materials. We overcame the solubility limit via epitaxial stabilization in a reactive environment, and report the physical properties of the heavily overdoped cuprates. We observed that the lattice and electronic structures monotonically evolve upon doping up to $x = 0.5$, and surprisingly, superconductivity persists in the heavily overdoped regime.

5.1.2 Introduction

The quantum phase behavior of layered copper oxides has shaped current research on strongly correlated materials. The cuprate phase diagram hosts physical phenomena such as high-temperature superconductivity, the pseudogap, and charge-density waves [KKN+15] and shows that superconductivity evolves out of an antiferromagnetic insulator as the parent compound is doped with holes [CMCM08]. The transition temperature (T_c) increases upon doping in the *underdoped* regime, reaches a maximum at the optimal doping ($p \sim 0.16$), and decreases upon further doping in the *overdoped* regime, thus forming the so-called superconducting dome. The underdoped side of the phase diagram is crowded with various spin- and charge-orders, which are reflections of strong magnetic and Coulomb correlations [KKN+15]. In contrast, the overdoped side exhibits Fermi-liquid-like behavior that coexists with persistent spin-fluctuation [DDS+13; LMP+13;

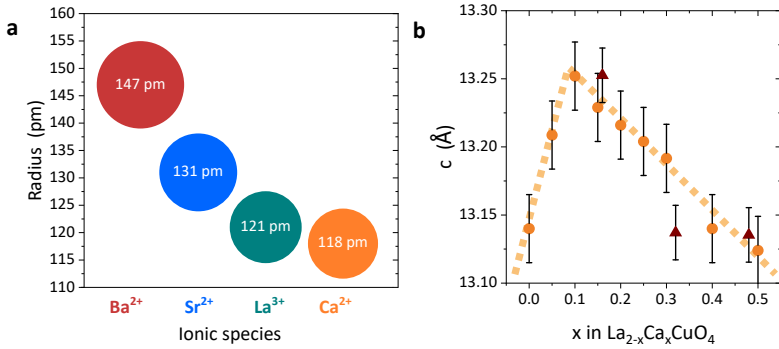


Figure 5.1: **Influence of cation-substitution to the lattice.** **a**, Comparison of ionic radii of alkaline-earth cations that are commonly used to substitute La^{3+} for hole doping. **b**, Doping dependence of the c-lattice parameter. Circles and triangles indicate thin and thick films, respectively. The dashed lines are guides to the eye.

MLP+17], a reminiscence of the static antiferromagnetic order. However the origin of the diminishing T_c upon doping is still controversial. The suppression of superconductivity in overdoped cuprates was commonly explained by the gradual weakening of magnetic correlations upon doping [Sca12; WZY+04], which are closely related to the superconducting mechanism [DHB+09; KKN+15; Sca12; VDG20]. On the other hand, recent observations of magnetic excitations that persist even in highly overdoped non-superconducting $La_{2-x}Sr_xCuO_4$ (LSCO) thin films and $Tl_2Ba_2CuO_{6+\delta}$ crystals with greatly suppressed T_c are at odds with such explanations [DDS+13; LMP+13; WIK+15]. Theoretical research based on the two-dimensional Hubbard model, the simplest generic model for the superconducting cuprates, predicts the persistence of superconductivity up to doping levels well beyond the experimentally reported superconducting dome [RKS10].

However, the presence of collective fluctuations that mediate Cooper pairing does not guarantee superconductivity, because other factors such as lattice distortions and impurities can break the superconducting Cooper-pairs. This is apparent from conventional superconductivity, which is extremely

susceptible to magnetic impurities although the electron-phonon interaction that is responsible for conventional superconductivity is robust against small concentration of impurities [Tin04]. In studies of overdoped cuprates, doped La_2CuO_4 (LCO) including particularly LSCO have been widely investigated due to the simplicity of their cation-chemistry and the wide accessible doping-range in contrast to the other cuprates that are doped by varying the oxygen contents[BHWB16; DDS+13; WBHB17]. However, doped LSCO belongs to a more disordered group among the cuprate superconductors because the dopants are located right above the CuO_2 planes [ABGH09; LDB17a]. Despite attempts to circumvent disorder-related issues in LSCO in ultra-clean thin films grown by oxide-molecular-beam epitaxy, the dopant-host radii mismatch (DHRM) between Sr^{2+} and La^{3+} cannot be avoided by improving the purity or crystallinity [BAL+11; BDY+11; BHWB16; DDS+13; LDB17a; LMBH18; LÖM+19; WBHB17] (see Fig. 5.1a). Since T_c in doped LCO is known to be sensitive to disorder induced by the DHRM [AKM98], it is essential to minimize the DHRM to exclude extrinsic effects introduced by chemical complications. From this point of view Ca is the best dopant to minimize the DHRM (see Fig. 5.1a), however the solubility of Ca is limited to concentrations lower than 0.12 in bulk samples [MSX+92; TYM+94]. This limitation has impeded the investigation of overdoped and even optimally doped compounds.

We report the synthesis of $\text{La}_{2-x}\text{Ca}_x\text{CuO}_4$ (LCCO) thin films with a wide doping-range via epitaxial stabilization, which allowed us to confirm the presence of superconductivity in the heavily overdoped regime (≤ 0.5), in which magnetic correlations have been found to persist [DDS+13; WIK+15]. The influence of random lattice distortions induced by dopants in LCO has been a source of controversy since the discovery of high temperature superconductivity, including particularly the overdoped regime where many unexpected results were observed, such as the suppression of superfluid density [BHWB16; LDB17a; LMBH18; LÖM+19; MHBA19], and the saturation of the spectral weight transfer to the Zhang-Rice singlet (ZRS) band [MDB10; PHS+09]. Our data on LCCO films provide new insight into the influence of the DHRM on these results and introduce a new system to study

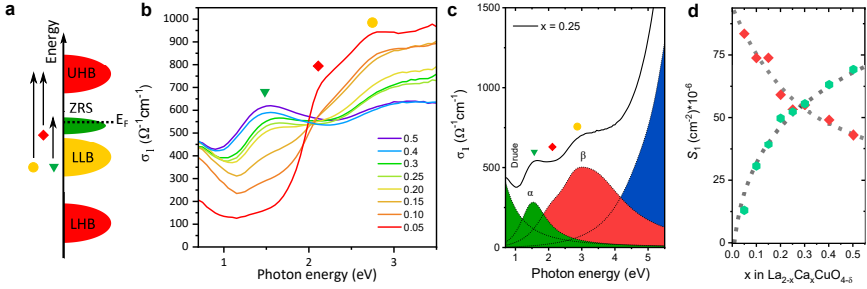


Figure 5.2: **Optical spectra and spectral weight analysis.** **a**, A schematic diagram of the band structure of LCCO. The arrows signify the optical transitions. Here LHB, LLB, ZRS and UHB stand for the lower Hubbard band, the low-lying band, the Zhang-Rice singlet and the upper Hubbard band, respectively. Symbols signify the inter-band optical transitions. **b**, The real part of optical conductivity at room temperature, σ_1 , of thin films. The symbols correspond to optical transitions described in **a**. **c**, An example of spectral weight analysis based on Lorentzian fitting. **d**, The doping-evolution of spectral weight. The dashed lines are guides to the eye.

the whole phase diagram of the cuprates.

5.1.3 Results

Sample growth. The solubility of dopants into LCO has been limited to low concentrations in bulk samples: The solubility limit of Sr is the highest among group II elements, $x = 0.24 \sim 0.3$, where the end of the superconducting dome is also commonly reported. It has been extended by epitaxial stabilization using ozone-assisted MBE [DDS+13; KCL+17; STNM00], where prior studies showed extension of the superconducting dome up to $x \sim 0.35$. We synthesized samples with thicknesses of 10 unit-cell ($t_{film} \sim 13.2$ nm) using the ozone-assisted MBE, and prepared thicker films, $t_{film} \sim 132$ nm, as bulk-like samples (see Methods for details). We determined the solubility of Ca in epitaxially stabilized LCCO films as between 0 and 0.5 via examining the evolution of the c -lattice constant upon doping (Fig. 5.1b). Considering that the in-plane lattice parameter is pinned by the substrate ($a = b = 3.765$ Å),

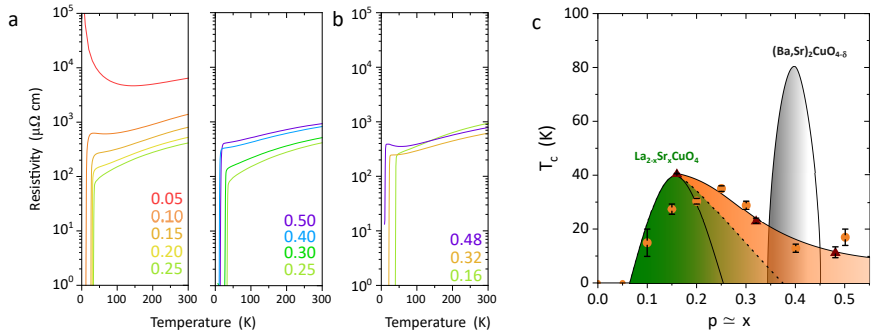


Figure 5.3: **Resistivity measurements.** **a**, Resistivity curves of LCCO films with $t_{film} \sim 13.2$ nm. The numbers in the plots indicate the concentrations of dopants. **b**, Resistivity curves of LCCO films with $t_{film} \sim 132$ nm. **c**, The summary of doping-dependent T_c . Circles and triangles specify T_c s of films with $t_{film} \sim 13.2$ nm and ~ 132 nm, respectively. The T_c was estimated as the half of the resistivity drop, and the error bars indicate the widths of the transitions. The green-shaded area enveloped by a solid line indicates the phase diagram of bulk LSCO. The dashed line shows the superconducting regions of LSCO thin films from the literature [DDS+13; KCL+17; STNM00]. The gray-shaded area corresponds to the phase diagram of $(\text{Ba,Sr})_2\text{CuO}_{4-\delta}$ inferred from the literature [Sca19].

the out-of-plane lattice parameter, c , of homogeneous LCCO should systematically evolve upon doping assuming no structural phase transition [STNM00]. The c -parameter of LCCO thin films follows a monotonic doping dependence in $0.15 < x < 0.5$, evidencing the formation of homogeneous solid solution (Note that the non-monotonic behavior for low x in Fig. 5.1 is due to a phase transition between orthorhombic and tetragonal structures.). On the other hand, samples with $x \geq 0.6$, exhibit a sharp increase in c , and significantly broadened Bragg peaks due to decomposition.

Optical spectroscopy. The electronic structure of hole-doped LCO is governed by the alignment between the oxygen p -bands and the upper Hubbard band (UHB), which makes the parent compound a charge transfer (CT) insulator [ZSA85]. Upon doping, a hole in the oxygen network is hybridized with an electron at the Cu site forming the ZRS band [ZR88], which is

the basis for single-band models, and the predominant O-2p character of ZRS has been confirmed with O K-edge X-ray absorption spectroscopy (XAS) [CSM+91]. XAS and resonant inelastic X-ray scattering (RIXS) that are sensitive to the ZRS band demonstrated that the spectral weight of the ZRS grows rapidly upon moderate hole-doping [CSM+91; CTK+92; EKZ+11; PHS+09].

We carried out optical spectroscopy at room temperature to examine the electronic structure of LCCO thin films with unprecedentedly high concentrations of dopants, because the energy-scale of all relevant bands is in the range of visible light, especially the CT gap and the ZRS band [UIT+91; WHK10] (see Fig. 5.2a). We utilized spectroscopic ellipsometry to obtain the optical spectra presented in Fig. 5.2 b, which show a monotonic doping-dependence: the CT gap is strongly suppressed, and the spectral weight below 2 eV grows, which is clearly demonstrated by the isosbestic point at 2 eV. The systematic change upon doping supports the formation of homogeneous solid solutions in LCCO with $x \leq 0.5$. In contrast, samples with $x \geq 0.6$ exhibit a collapse of optical spectra (not shown here). In order to quantify the doping-evolution of optical spectra, we analyzed the doping-dependence of the spectral weight (see Fig. 5.2c): Low energy features are the α and Drude peaks that correspond to the spectral weight of the ZRS band [EKZ+11], and high energy features, β , are due to inter-band transitions to the UHB [CMCM08; UIT+91; WHK10]. Upon doping, the ZRS components grow and β decays proportional to the doping level as presented in Fig. 5.2d showing remarkable agreement with previous XAS and RIXS results in the low doping range, $x \leq 0.2$ [CSM+91; CTK+92; EKZ+11; PHS+09]. However we did not confirm the previously reported saturation of the ZRS band [MDB10; PHS+09]. Instead we observed the continuation of the spectral weight transfer to the ZRS band up to the the solubility limit. This trend matches well with predictions based on model CT systems [EMS91; MES93]. This is the first experimental confirmation of the doping-dependent spectral weight transfer in the overdoped regime, which has been controversial [PHS+09]. Furthermore, close agreement of our experimental data on the doping-dependent electronic structure in LCCO

with model calculations reinforces the effectiveness of our strategy to adopt Ca as dopants.

Resistivity measurements. The systematic evolution of the lattice and electronic structures motivated us to examine the superconducting properties of the heavily overdoped cuprates with minimized cation-induced disorder. Temperature-dependent resistivity, $\rho(T)$, curves are presented in Fig. 5.3 a and b. The resistivity at 300 K, $\rho(300K)$, evolves systematically: it decreases until $x = 0.25$, and increases after that, which is consistent with studies on LSCO [MHBA19; STNM00; TIU+89]. The sharp drops at low temperatures demonstrate the presence of superconductivity in samples with $x > 0.05$. In the light of previous work, it is surprising that the superconductivity persists in the highly overdoped samples, $x = 0.5$, which is twice the doping concentration where the superconducting dome ends in bulk samples (see Fig. 5.3c). It is common for MBE-grown LSCO films to exhibit an extended superconducting dome as marked with a dashed line in the phase diagram[DDS+13; KCL+17; STNM00], and we could extend the range further by adopting better-matching dopants.

The maximum T_c of LCCO thin film is 40 K in the bulk-like LCCO samples with $x = 0.16$, which to our knowledge has not been achieved with Ca doping. The high T_c and the sharp superconducting transition of our bulk-like film verify our good control over the stoichiometry, and the effectiveness of epitaxial stabilization. The T_c s of 10 u.c. and 100 u.c. thick films fall into the same trend in the highly overdoped regime, suggesting that the extended phase diagram does not originate from the interface between substrates and films, but is an intrinsic effect of overdoped LCCO thin films. However, there is some mismatch in the lightly doped regime, where the bulk-like sample shows a higher transition temperature. The discrepancy can be attributed to epitaxy-induced effects [CBG+94], the charge-density wave stabilized by the substrates [BFS+18], and/or the strain effect [STNM00].

Discussion

Our results demonstrate the presence of superconductivity in heavily overdoped LCCO thin films, and suggest that cation-induced disorder plays an

important role in determining the end of the superconducting dome. The importance of the DHRM for superconductivity was discussed in previous work, where the influence of the average and the standard deviation of the DHRM was clearly shown based on optimally doped samples with different combinations of cation species [AKM98]. Our strategy of adopting Ca as a dopant is consistent with the logic of Attfield *et al.* [AKM98], who predicted that the effect of the DHRM should be prominent in compounds with higher concentrations of dopants.

High temperature superconductivity in highly overdoped cuprates is an active topic of research. In particular $(\text{Ba,Sr})_2\text{CuO}_{4-\delta}$, which has a similar structure as LCO, exhibits superconductivity with high $T_c \sim 80$ K despite its extremely high hole concentration $p \sim 0.4$, seemingly forming a superconducting region isolated from the superconducting dome of LSCO (see Fig. 5.3c) [GKN+16; GLY+09; LBZ+19; Sca19]. Our LCCO films connect the two separately studied regions and thus suggest a simpler picture. The phase diagram of LCCO resembles that of iron-based superconductors, especially with compounds known as Ba-122 such as $\text{Ba}_{1-x}\text{K}_x\text{Fe}_2\text{As}_2$ and $\text{BaFe}_{2-x}\text{Co}_x\text{As}_2$, where the superconducting dome displays a long tail, or even continues until the other end-member of the phase diagram [FCS14; PG10; WL11]. Considering that iron-based and cuprate superconductors share many traits such as the two-dimensional structure and the antiferromagnetism of the parent compound, it is not surprising that they exhibit a similar range of cation-doping for superconductivity. Indeed the two-dimensional single band Hubbard model also predicts superconductivity over most of the phase diagram, although the pairing symmetry may change from the $d(x^2 - y^2)$ symmetry at low doping [RKS10].

Recently, the dopant-induced disorder has received attention due to the discovery of the anomalous suppression of superfluid density in the overdoped LSCO thin films [BHWB16; MHBA19], which raises questions about possible un-condensed carriers in the superconducting state. A series of studies adopted the theory of dirty d -wave superconductivity to explain the surprising observation with a model that includes the influence of cation-induced disorder. The model successfully replicated the data, and further

suggested that superconductivity may persist in the highly overdoped regime if one can reduce the cation-induced disorder [LDB17a; LMBH18; LÖM+19]. We argue that the persistence of superconductivity in our LCCO thin films is the realization of such a system. Our results thus support the disorder-based interpretation of the suppression of superfluid density in the overdoped regime. Indeed, the normal state conductivity of LSCO thin films that showed suppressed superfluid density continuously decreases in concert with T_c [MHBA19], which is consistent with our observation on LCCO films, and also with the theoretical analyses based on dirty d -wave superconductivity [LMBH18].

Lastly, our observation is consistent with recent RIXS measurements that established the puzzling continuation of magnetic excitations in highly overdoped non-superconducting LSCO thin films [DDS+13], because the study hints that the most prominent pair-mediating interaction survives in the regime we investigated here. We assert here again that the presence of a pair-mediating interaction is a necessary but not a sufficient condition, and one needs to minimize the chemical effects such as DHRM and octahedral distortions to actuate the pairing interaction and form superconducting pairs. Regardless of the specific microscopic mechanism, improving the DHRM is an effective way to study the intrinsic physical properties of the cuprates and other transition metal oxides. We therefore suggest that epitaxially stabilized LCCO can serve as a model system.

5.1.4 Methods

Thin film growth and characterization Thin films were grown on LaSrAlO_4 (001) single-crystalline substrates (Crystec GmbH) by using an ozone-assisted ALL-MBE system (DCA Instruments). The growth was monitored by using in situ reflection high energy electron diffraction (RHEED). During growth the substrate temperature was kept at 630 °C according to the radiative pyrometer and the pressure was $\sim 1 \times 10^{-5}$ Torr. The effusion cells were calibrated before every growth to obtain the accurate composition of the films. c lattice parameters were measured by high-resolution x-ray diffraction using

a Cu-K α source and a high resolution diffractometer (Bruker, GmbH).

Optical spectroscopy Optical spectroscopy was performed at room temperature using a variable-angle spectroscopic ellipsometer (Woollam, Co.) in the photon energy range 0.7-6.5 eV at an incident angle of 70 degrees.

Electrical transport measurement The electric transport measurements were done using a Physical Property Measurement System (Quantum Design, Inc.) with a van der Pauw geometry. Ag/Au metallic contacts were deposited on the four corners of square shaped samples before measurements.

BIBLIOGRAPHY

- [AAM+07] M. Ali, P. Adie, C. H. Marrows, D. Greig, B. J. Hickey, R. L. Stamps. In: *Nat. Mater.* 6 (2007), p. 70 (cit. on p. 74).
- [ABGH09] H. Alloul, J. Bobroff, M. Gabay, P. J. Hirschfeld. In: *Rev. Mod. Phys.* 81 (1 Jan. 2009), pp. 45–108 (cit. on p. 92).
- [ABI+99] B. Ammundsen, G. R. Burns, M. S. Islam, H. Kanoh, J. Rozière. In: *J. Phys. Chem. B* 103.25 (1999), pp. 5175–5180 (cit. on p. 59).
- [AKM98] J. P. Attfield, A. L. Kharlanov, J. A. McAllister. In: *Nature* 394 (1998), p. 157 (cit. on pp. 92, 97).
- [ALI+16] M. S. Anwar, S. R. Lee, R. Ishiguro, Y. Sugimoto, Y. Tano, S. J. Kang, Y. J. Shin, S. Yonezawa, D. Manske, H. Takayanagi, T. W. Noh, Y. Maeno. In: *Nat. Commun.* 7 (2016), p. 13220 (cit. on p. 46).
- [ARS+05] P. Abbamonte, A. Rusydi, S. Smadici, G. D. Gu, G. A. Sawatzky, D. L. Feng. In: *Nature Physics* 1 (3 Dec. 2005), p. 155 (cit. on p. 27).
- [BAL+11] L. S. Bilbro, R. V. Aguilar, G. Logvenov, O. Pelleg, I. Božović, N. P. Armitage. In: *Nat. Phys.* 7 (2011), p. 298 (cit. on pp. 35, 92).
- [BAM+16] B. Burganov, C. Adamo, A. Mulder, M. Uchida, P. D. C. King, J. W. Harter, D. E. Shai, A. S. Gibbs, A. P. Mackenzie, R. Uecker, M. Bruetzam, M. R. Beasley, C. J. Fennie, D. G. Schlom, K. M. Shen. In: *Phys. Rev. Lett.* 116 (19 May 2016), p. 197003 (cit. on pp. 45, 46).

- [BCE+20] C. Back, V. Cros, H. Ebert, K. Everschor-Sitte, A. Fert, M. Garst, M. Tianping, S. Mankovsky, T. L. Monchesky, M. Mostovoy, N. Nagaosa, S. S. P. Parkin, C. Pfleiderer, N. Reyren, A. Rosch, Y. Taguchi, Y. Tokura, K. von Bergmann, J. Zang. In: *arXiv:2001.00026* (2020) (cit. on p. 76).
- [BDY+11] A. T. Bollinger, G. Dubuis, J. Yoon, D. Pavuna, J. Misewich, I. Božović. In: *Nature* 472 (Apr. 2011), p. 458 (cit. on p. 92).
- [Ber84] G. Bergmann. In: *Physics Reports* 107.1 (1984), pp. 1–58 (cit. on p. 21).
- [BFS+18] M. Bluschke, A. Frano, E. Schierle, D. Putzky, F. Ghorbani, R. Ortiz, H. Suzuki, G. Christiani, G. Logvenov, E. Weschke, R. J. Birgeneau, E. H. da Silva Neto, M. Minola, S. Blanco-Canosa, B. Keimer. In: *Nat. Comms.* 9 (July 2018), p. 2978 (cit. on p. 96).
- [BGG+87] T. Brun, M. Grimsditch, K. E. Gray, R. Bhadra, V. Maroni, C. ...-K. Loong. In: *Phys. Rev. B* 35 (1987), p. 8837 (cit. on p. 37).
- [BGM+18] M. E. Barber, A. S. Gibbs, Y. Maeno, A. P. Mackenzie, C. W. Hicks. In: *Phys. Rev. Lett.* 120 (7 Feb. 2018), p. 076602 (cit. on p. 45).
- [BHA+19] H. Boschker, T. Harada, T. Asaba, R. Ashoori, A. V. Boris, H. Hilgenkamp, C. R. Hughes, M. E. Holtz, L. Li, D. A. Muller, H. Nair, P. Reith, X. Renshaw Wang, D. G. Schlom, A. Soukiassian, J. Mannhart. In: *Phys. Rev. X* 9 (1 2019), p. 011027 (cit. on p. 78).
- [BHWB16] I. Božović, X. He, J. Wu, A. T. Bollinger. In: *Nature* 536 (2016), p. 309 (cit. on pp. 35, 36, 44, 92, 97).
- [BLG+15] F. Baiutti, G. Logvenov, G. Gregori, G. Cristiani, Y. Wang, W. Sigle, P. A. van Aken, J. Maier. In: *Nat. Comm.* 6 (2015), p. 8586 (cit. on pp. 36, 68).
- [BM14] A. Bhattacharya, S. J. May. In: *Annu. Rev. Mater. Res.* 44 (2014), p. 65 (cit. on p. 63).
- [BMV+08] A. Bhattacharya, S. J. May, S. G. E. te Velthuis, M. Warusawithana, X. Zhai, B. Jiang, J.-M. Zuo, M. R. Fitzsimmons, S. D. Bader, J. N. Eckstein. In: *Phys. Rev. Lett.* 100 (25 June 2008), p. 257203 (cit. on p. 68).

- [BNC+16] A. Barla, J. Nicolás, D. Cocco, S. M. Valvidares, J. Herrero-Martín, P. Gargiani, J. Moldes, C. Ruget, E. Pellegrin, S. Ferrer. In: *Journal of Synchrotron Radiation* 23.6 (2016), pp. 1507–1517 (cit. on p. 49).
- [BRS+07] M. Braden, W. Reichardt, Y. Sidis, Z. Mao, Y. Maeno. In: *Phys. Rev. B* 76 (1 2007), p. 014505 (cit. on pp. 24, 58).
- [BSD+17] T. Berlijn, P. C. Snijders, O. Delaire, H.-D. Zhou, T. A. Maier, H.-B. Cao, S.-X. Chi, M. Matsuda, Y. Wang, M. R. Koehler, P. R. C. Kent, H. H. Weitering. In: *Phys. Rev. Lett.* 118 (7 Feb. 2017), p. 077201 (cit. on p. 24).
- [BSH+19] F. M. Bartram, S. Sorn, K. Hwangbo, S. Shen, F. Frontini, L. He, P. Yu, A. Paramekanti, L. Yang. In: *arXiv:1908.08974* (2019) (cit. on pp. 76, 79).
- [BVB11] M. Bibes, J. E. Villegas, A. Barthélémy. In: *Adv. Phys.* 60:1 (2011), p. 5 (cit. on pp. 63, 68).
- [CBG+94] M. Z. Cieplak, M. Berkowski, S. Guha, E. Cheng, A. S. Vagelos, D. J. Rabinowitz, B. Wu, I. E. Trofimov, P. Lindenfeld. In: *Applied Physics Letters* 65.26 (1994), pp. 3383–3385 (cit. on p. 96).
- [CFH+07] J. Chakhalian, J. W. Freeland, H.-U. Habermeier, G. Cristiani, G. Khaliullin, M. van Veenendaal, B. Keimer. In: *Science* 318 (2007), p. 1114 (cit. on p. 64).
- [CFS+06] J. Chakhalian, J. W. Freeland, G. Srajer, J. Stempfer, G. Khaliullin, J. C. Cezar, T. Charlton, R. Dalgliesh, C. Bernhard, G. Cristiani, H.-U. Habermeier, B. Keimer. In: *Nat. Phys.* 2 (2006), p. 244 (cit. on pp. 68, 72).
- [CGT+06] L. Childress, M. V. Gurudev Dutt, J. M. Taylor, A. S. Zibrov, F. Jelezko, J. Wrachtrup, P. R. Hemmer, M. D. Lukin. “Coherent Dynamics of Coupled Electron and Nuclear Spin Qubits in Diamond.” In: *Science* 314.5797 (2006), pp. 281–285 (cit. on p. 13).
- [CKLT18] S. B. Chung, S. K. Kim, K. H. Lee, Y. Tserkovnyak. In: *Phys. Rev. Lett.* 121 (16 2018), p. 167001 (cit. on p. 46).
- [CMCM08] A. Comanac, L. de’Medici, M. Capone, A. J. Millis. In: *Nat. Phys.* 4 (2008), p. 289 (cit. on pp. 90, 95).
- [CMV+16] J. Cao, D. Massarotti, M. E. Vickers, A. Kursumovic, A. D. Bernardo, J. W. A. Robinson, F. Tafuri, J. L. MacManus-Driscoll, M. G. Blamire. In: *Supercond. Sci. Technol.* 29.9 (July 2016), p. 095005 (cit. on p. 46).

- [CSM+91] C. T. Chen, F. Sette, Y. Ma, M. S. Hybertsen, E. B. Stechel, W. M. C. Foulkes, M. Schulter, S.-W. Cheong, A. S. Cooper, L. W. Rupp, B. Batlogg, Y. L. Soo, Z. H. Ming, A. Krol, Y. H. Kao. In: *Phys. Rev. Lett.* 66 (1 Jan. 1991), pp. 104–107 (cit. on pp. 27, 95).
- [CTK+92] C. T. Chen, L. H. Tjeng, J. Kwo, H. L. Kao, P. Rudolf, F. Sette, R. M. Fleming. In: *Phys. Rev. Lett.* 68 (16 Apr. 1992), pp. 2543–2546 (cit. on p. 95).
- [DC17] B. Dieny, M. Chshiev. In: *Rev. Mod. Phys.* 89 (2017), p. 025008 (cit. on p. 62).
- [DCK+04] B. Dabrowski, O. Chmaissem, P. W. Klamut, S. Kolesnik, M. Maxwell, J. Mais, Y. Ito, B. D. Armstrong, J. D. Jorgensen, S. Short. In: *Phys. Rev. B* 70 (1 July 2004), p. 014423 (cit. on pp. 46, 78).
- [DCS+18] Y. Dovzhenko, F. Casola, S. Schlotter, T. X. Zhou, F. Büttner, R. L. Walsworth, G. S. D. Beach, A. Yacoby. In: *Nat. Comm.* 9 (2018), p. 2712 (cit. on p. 86).
- [DDS+13] M. P. M. Dean, G. Dellea, R. S. Springell, F. Yakhov-Harris, K. Kummer, N. B. Brookes, X. Liu, Y.-J. Sun, J. Strle, T. Schmitt, L. Braicovich, G. Ghiringhelli, I. Božović, J. P. Hill. In: *Nat. Mater.* 12 (2013), p. 1019 (cit. on pp. 90–94, 96, 98).
- [DHB+09] T. Dahm, V. Hinkov, S. V. Borisenko, A. A. Kordyuk, V. B. Zabolotnyy, J. Fink, B. Büchner, D. J. Scalapino, W. Hanke, B. Keimer. In: *Nat. Phys.* 5 (2009), p. 217 (cit. on p. 91).
- [DSC+18] C. Dietl, S. K. Sinha, G. Christiani, Y. Khaydukov, T. Keller, D. Putzky, S. Ibrahimkuty, P. Wochner, G. Logvenov, P. A. van Aken, B. J. Kim, B. Keimer. In: *Appl. Phys. Lett.* 112.3 (2018), p. 031902 (cit. on p. 47).
- [EFLP61] A. Earnshaw, B. N. Figgis, J. Lewis, R. D. Peacock. In: *J. Chem. Soc.* (0 1961), pp. 3132–3138 (cit. on p. 24).
- [EKZ+11] D. S. Ellis, J. Kim, H. Zhang, J. P. Hill, G. Gu, S. Komiyama, Y. Ando, D. Casa, T. Gog, Y.-J. Kim. In: *Phys. Rev. B* 83 (7 Feb. 2011), p. 075120 (cit. on p. 95).
- [EMS91] H. Eskes, M. B. J. Meinders, G. A. Sawatzky. In: *Phys. Rev. Lett.* 67 (8 Aug. 1991), pp. 1035–1038 (cit. on p. 95).

- [Ert08] G. Ertl. “Reactions at Surfaces: From Atoms to Complexity (Nobel Lecture).” In: *Angewandte Chemie International Edition* 47.19 (2008), pp. 3524–3535 (cit. on p. 13).
- [FCS14] R. M. Fernandes, A. V. Chubukov, J. Schmalian. In: *Nat. Phys.* 10 (2014), p. 97 (cit. on p. 97).
- [FDF+15] C. G. Fatuzzo, M. Dantz, S. Fatale, P. Olalde-Velasco, N. E. Shaik, B. Dalla Piazza, S. Toth, J. Pellicciari, R. Fittipaldi, A. Vecchione, N. Kikugawa, J. S. Brooks, H. M. Rønnow, M. Grioni, C. Rüegg, T. Schmitt, J. Chang. In: *Phys. Rev. B* 91 (15 Apr. 2015), p. 155104 (cit. on p. 25).
- [Fuj07] H. Fujiwara. *Spectroscopic Ellipsometry*. John Wiley Sons, Ltd, 2007, pp. 81–146 (cit. on p. 28).
- [FZJ+16] M. Fan, W. Zhang, J. Jian, J. Huang, H. Wang. In: *APL Materials* 4 (2016), p. 076105 (cit. on p. 64).
- [GB14] V. Garcia, M. Bibes. In: *Nat. Commun.* 5 (2014), p. 4289 (cit. on p. 46).
- [GCH+10] A. Gentils, O. Copie, G. Herranz, F. Fortuna, M. Bibes, K. Bouzouhane, É. Jacquet, C. Carrétéro, M. Basleti ć, E. Tafra, A. Hamzi ć, A. Barthélémy. In: *Phys. Rev. B* 81 (14 Apr. 2010), p. 144109 (cit. on p. 44).
- [Ger18] A. Gerber. In: *Phys. Rev. B* 98 (21 2018), p. 214440 (cit. on p. 77).
- [Gin98] D. M. Ginsberg. *Physical Properties of High Temperature Superconductors I*. WORLD SCIENTIFIC, 1998 (cit. on p. 23).
- [GKN+16] A. Gauzzi, Y. Klein, M. Nisula, M. Karppinen, P. K. Biswas, H. Saadaoui, E. Morenzoni, P. Manuel, D. Khalyavin, M. Marezio, T. H. Geballe. In: *Phys. Rev. B* 94 (18 Nov. 2016), p. 180509 (cit. on p. 97).
- [GLY+09] W. B. Gao, Q. Q. Liu, L. X. Yang, Y. Yu, F. Y. Li, C. Q. Jin, S. Uchida. In: *Phys. Rev. B* 80 (9 Sept. 2009), p. 094523 (cit. on p. 97).
- [GSGK02] O. Y. Gorbenko, S. V. Samoilenov, I. E. Graboy, A. R. Kaul. In: *Chemistry of Materials* 14.10 (2002), pp. 4026–4043 (cit. on p. 19).
- [GWX+19] Y. Gu, Y.-W. Wei, K. Xu, H. Zhang, F. Wang, F. Li, M. S. Saleem, C.-Z. Chang, J. Sun, C. Song, J. Feng, X. Zhong, W. Liu, Z. Zhang, J. Zhu, F. Pan. In: *J. Phys. D: Appl. Phys.* 52.40 (2019), p. 404001 (cit. on pp. 76, 79).

- [GZS+12] M. Gibert, P. Zubko, R. Scherwitzl, J. Íñiguez, J.-M. Triscone. In: *Nat. Mater.* 11 (3 2012), pp. 195–198 (cit. on pp. 30, 64).
- [Hal04] F. D. M. Haldane. In: *Phys. Rev. Lett.* 93 (20 Nov. 2004), p. 206602 (cit. on p. 76).
- [HCI+97] V. G. Hadjiev, M. Cardona, I. Ivanov, V. Popov, M. Gyulmezov, M. N. Iliev, M. Berkowski. In: *J. Alloys Comp.* 251 (1997), pp. 7–10 (cit. on p. 38).
- [HCR+16] Y.-T. Hsu, W. Cho, A. F. Rebola, B. Burganov, C. Adamo, K. M. Shen, D. G. Schlom, C. J. Fennie, E.-A. Kim. In: *Phys. Rev. B* 94 (4 July 2016), p. 045118 (cit. on pp. 45, 46).
- [HET+08] M. W. Haverkort, I. S. Elfimov, L. H. Tjeng, G. A. Sawatzky, A. Damascelli. In: *Phys. Rev. Lett.* 101 (2 July 2008), p. 026406 (cit. on p. 25).
- [HIK+12] H. Y. Hwang, Y. Iwasa, M. Kawasaki, B. Keimer, N. Nagaosa, Y. Tokura. In: *Nat. Mater.* 11 (2012), p. 103 (cit. on p. 64).
- [HKB+15] M. Hepting, D. Kukuruznyak, E. Benckiser, M. L. Tacon, B. Keimer. In: *Physica C* 460 (2015), pp. 196–198 (cit. on p. 37).
- [HKK+13] N. Haham, M. Konczykowski, B. Kuiper, G. Koster, L. Klein. In: *Phys. Rev. B* 88 (21 2013), p. 214431 (cit. on p. 79).
- [HLC+91] E. T. Heyen, R. Liu, M. Cardona, S. Piñol, R. J. Melville, D. M. Paul, E. Morán, M. A. Alario-Franco. In: *Phys. Rev. B* 43 (1991), p. 2857 (cit. on pp. 38, 39).
- [HLG+00] Z. Hu, H. von Lips, M. S. Golden, J. Fink, G. Kaindl, F. M. F. de Groot, S. Ebbinghaus, A. Reller. In: *Phys. Rev. B* 61 (8 Feb. 2000), pp. 5262–5266 (cit. on p. 25).
- [HMF+14] M. Hepting, M. Minola, A. Frano, G. Cristiani, G. Logvenov, E. Schierle, M. Wu, M. Bluschke, E. Weschke, H.-U. Habermeier, E. Benckiser, M. Le Tacon, B. Keimer. In: *Phys. Rev. Lett.* 113 (22 Nov. 2014), p. 227206 (cit. on pp. 37, 55).
- [HSS+11] N. Haham, Y. Shperber, M. Schultz, N. Naftalis, E. Shimshoni, J. W. Reiner, L. Klein. In: *Phys. Rev. B* 84 (17 2011), p. 174439 (cit. on pp. 79, 80).
- [IPL+05] M. N. Iliev, V. N. Popov, A. P. Litvinchuk, M. V. Abrashev, J. Bäckström, Y. Y. Sun, R. L. Meng, C. W. Chu. In: *Physica B: Condensed Matter* 358 (2005), pp. 138–152 (cit. on pp. 24, 55).

- [IZHC97] M. N. Iliev, P. X. Zhang, H. .-U. Habermeier, M. Cardona. In: *J. Alloys Comp.* 251 (1997), pp. 99–102 (cit. on p. 36).
- [JKP+17] A. Jain, M. Krautloher, J. Porras, G. H. Ryu, D. P. Chen, D. L. Abernathy, J. T. Park, A. Ivanov, J. Chaloupka, G. Khaliullin, B. Keimer, B. J. Kim. In: *Nature Physics* 13 (7 July 2017), p. 633 (cit. on p. 24).
- [KAP+03] E. Kroumova, M. Aroyo, J. Perez-Mato, A. Kirov, C. Capillas, S. Ivantchev, H. Wondratschek. In: *Phase Transitions* 76.1-2 (2003), pp. 155–170 (cit. on p. 23).
- [KBB+92] B. Keimer, N. Belk, R. J. Birgeneau, A. Cassanho, C. Y. Chen, M. Greven, M. A. Kastner, A. Aharony, Y. Endoh, R. W. Erwin, G. Shirane. In: *Phys. Rev. B* 46 (21 Dec. 1992), p. 14034 (cit. on pp. 73, 74).
- [KBT+88] M. A. Kastner, R. J. Birgeneau, T. R. Thurston, P. J. Picone, H. P. Jenssen, D. R. Gabbe, M. Sato, K. Fukuda, S. Shamoto, Y. Endoh, K. Yamada, G. Shirane. In: *Phys. Rev. B* 38 (10 Oct. 1988), pp. 6636–6640 (cit. on p. 73).
- [KCL+17] G. Kim, G. Christiani, G. Logvenov, S. Choi, H.-H. Kim, M. Minola, B. Keimer. In: *Phys. Rev. Materials* 1 (5 Oct. 2017), p. 054801 (cit. on pp. 33, 55, 59, 93, 94, 96).
- [KKN+15] B. Keimer, S. A. Kivelson, M. R. Norman, S. Uchida, J. Zaanen. In: *Nature* 518 (2015), p. 179 (cit. on pp. 25, 34, 90, 91).
- [KKS+12] G. Koster, L. Klein, W. Siemons, G. Rijnders, J. S. Dodge, C.-B. Eom, D. H. A. Blank, M. R. Beasley. In: *Rev. Mod. Phys.* 84 (1 Mar. 2012), pp. 253–298 (cit. on pp. 46, 77, 78).
- [KM93] B. Kramer, A. MacKinnon. In: *Reports on Progress in Physics* 56.12 (Dec. 1993), pp. 1469–1564 (cit. on p. 21).
- [KMKS18] D. Kan, T. Moriyama, K. Kobayashi, Y. Shimakawa. In: *Phys. Rev. B* 98 (18 2018), p. 180408 (cit. on pp. 77, 78, 81).
- [KMS20] D. Kan, T. Moriyama, Y. Shimakawa. In: *Phys. Rev. B* 101 (1 Jan. 2020), p. 014448 (cit. on pp. 77, 78).
- [KN17] W. Koshibae, N. Nagaosa. In: *Sci. Rep.* 7 (Feb. 2017), p. 42645 (cit. on p. 78).
- [KNKO04] H.-D. Kim, H.-J. Noh, K. H. Kim, S.-J. Oh. In: *Phys. Rev. Lett.* 93 (12 Sept. 2004), p. 126404 (cit. on p. 24).

- [KSH+19a] G. Kim, Y. E. Suyolcu, J. Herrero-Martin, D. Putzky, H. P. Nair, J. P. Ruf, N. J. Schreiber, C. Dietl, G. Christiani, G. Logvenov, M. Minola, P. A. van Aken, K. M. Shen, D. G. Schlom, B. Keimer. In: *Phys. Rev. Materials* 3 (9 Sept. 2019), p. 094802 (cit. on pp. 33, 61).
- [KSH+19b] G. Kim, Y. E. Suyolcu, J. Herrero-Martin, D. Putzky, H. P. Nair, J. P. Ruf, N. J. Schreiber, C. Dietl, G. Christiani, G. Logvenov, M. Minola, P. A. van Aken, K. M. Shen, D. G. Schlom, B. Keimer. In: *Phys. Rev. Materials* 3 (9 Sept. 2019), p. 094802 (cit. on p. 78).
- [KUT+10] Y. Krockenberger, M. Uchida, K. S. Takahashi, M. Nakamura, M. Kawasaki, Y. Tokura. In: *Appl. Phys. Lett.* 97.8 (2010), p. 082502 (cit. on p. 46).
- [KV56] F. Kröger, H. Vink. In: ed. by F. Seitz, D. Turnbull. Vol. 3. Solid State Physics. Academic Press, 1956, pp. 307–435 (cit. on p. 18).
- [KVK+12] J.-H. Kim, I. Vrejoiu, Y. Khaydukov, T. Keller, J. Stahn, A. Rühm, D. K. Satapathy, V. Hinkov, B. Keimer. In: *Phys. Rev. B* 86 (18 Nov. 2012), 180402(R) (cit. on pp. 69, 77).
- [LBZ+19] W. Li, I. Bykova, S. Zhang, G. Yu, R. Tomasello, M. Carpentieri, Y. Liu, Y. Guang, J. Gräfe, M. Weigand, D. M. Burn, G. van der Laan, T. Hesjedal, Z. Yan, J. Feng, C. Wan, J. Wei, X. Wang, X. Zhang, H. Xu, C. Guo, H. Wei, G. Finocchio, X. Han, G. Schütz. In: *Adv. Mater.* 31.14 (2019), p. 1807683 (cit. on pp. 86, 97).
- [LDB17a] N. R. Lee-Hone, J. S. Dodge, D. M. Broun. In: *Phys. Rev. B* 96 (2 July 2017), p. 024501 (cit. on pp. 92, 98).
- [LDB17b] N. R. Lee-Hone, J. S. Dodge, D. M. Broun. In: *arXiv* 1704 (2017), p. 04803 (cit. on pp. 35, 44).
- [LGP+14] G. M. D. Luca, G. Ghiringhelli, C. A. Perroni, V. Vataudella, F. Chiarella, C. Cantoni, A. R. Lupini, N. B. Brookes, M. Huijben, G. Koster, G. Rijnders, M. Salluzzo. In: *Nat. Commun.* 5 (2014), p. 5626 (cit. on p. 72).
- [LLP06] D. Lampakis, E. Liarokapis, C. Panagopoulos. In: *Phys. Rev. B* 73 (2006), p. 174518 (cit. on p. 36).
- [LMBH18] N. R. Lee-Hone, V. Mishra, D. M. Broun, P. J. Hirschfeld. In: *Phys. Rev. B* 98 (5 Aug. 2018), p. 054506 (cit. on pp. 92, 98).

- [LMP+13] M. Le Tacon, M. Minola, D. C. Peets, M. Moretti Sala, S. Blanco-Canosa, V. Hinkov, R. Liang, D. A. Bonn, W. N. Hardy, C. T. Lin, T. Schmitt, L. Braicovich, G. Ghiringhelli, B. Keimer. In: *Phys. Rev. B* 88 (2 July 2013), p. 020501 (cit. on pp. 90, 91).
- [LÖM+19] N. R. Lee-Hone, H. U. Özdemir, V. Mishra, D. M. Broun, P. J. Hirschfeld. In: *arxiv:1902.08286* (2019) (cit. on pp. 92, 98).
- [LRS+98] W. Limmer, W. Ritter, R. Sauer, B. Mensching, C. Liu, B. Rauschenbach. In: *Appl. Phys. Lett.* 72.20 (1998), pp. 2589–2591 (cit. on p. 59).
- [LSB07] G. Logvenov, I. Sveklo, I. Božović. In: *Physica C: Superconductivity and its Applications* 460-462 (2007). Proceedings of the 8th International Conference on Materials and Mechanisms of Superconductivity and High Temperature Superconductors, pp. 416–419 (cit. on p. 19).
- [LSR+13] A. D. Lamirand, M. M. Soares, A. Y. Ramos, H. C. N. Tolentino, M. De Santis, J. C. Cezar, A. de Siervo, M. Jamet. In: *Phys. Rev. B* 88 (14 Oct. 2013), 140401(R) (cit. on p. 62).
- [LST+20] Z. Li, S. Shen, Z. Tian, K. Hwangbo, M. Wang, Y. Wang, F. M. Bartram, L. He, Y. Lyu, Y. Dong, G. Wan, H. Li, N. Lu, J. Zang, H. Zhou, E. Arenholz, Q. He, L. Yang, W. Luo, P. Yu. In: *Nat. Comm.* 11 (2020), p. 184 (cit. on pp. 76, 79).
- [MAB+19] K.-Y. Meng, A. S. Ahmed, M. Baćani, A.-O. Mandru, X. Zhao, N. Bagués, B. D. Esser, J. Flores, D. W. McComb, H. J. Hug, F. Yang. In: *Nano Lett.* 19.5 (2019), pp. 3169–3175 (cit. on pp. 76, 79, 86).
- [MBS18] A. O. Mufazalova, A. S. Belozarov, S. V. Streltsov. In: *Phys. Rev. B* 98 (13 2018), p. 134441 (cit. on p. 46).
- [MDB10] R. S. Markiewicz, T. Das, A. Bansil. In: *Phys. Rev. B* 82 (22 Dec. 2010), p. 224501 (cit. on pp. 92, 95).
- [MDO19] N. Mohanta, E. Dagotto, S. Okamoto. In: *Phys. Rev. B* 100 (6 Aug. 2019), p. 064429 (cit. on p. 78).
- [MES93] M. B. J. Meinders, H. Eskes, G. A. Sawatzky. In: *Phys. Rev. B* 48 (6 Aug. 1993), pp. 3916–3926 (cit. on p. 95).
- [MHBA19] F. Mahmood, X. He, I. Božović, N. P. Armitage. In: *Phys. Rev. Lett.* 122 (2 2019), p. 027003 (cit. on pp. 92, 96–98).

- [MHT+98] A. P. Mackenzie, R. K. W. Haselwimmer, A. W. Tyler, G. G. Lonzarich, Y. Mori, S. Nishizaki, Y. Maeno. In: *Phys. Rev. Lett.* 80 (1 Jan. 1998), pp. 161–164 (cit. on p. 46).
- [MJD+96] A. P. Mackenzie, S. R. Julian, A. J. Diver, G. J. McMullan, M. P. Ray, G. G. Lonzarich, Y. Maeno, S. Nishizaki, T. Fujita. In: *Phys. Rev. Lett.* 76 (20 1996), p. 3786 (cit. on p. 45).
- [MKAS17] P. B. Marshall, H. Kim, K. Ahadi, S. Stemmer. In: *APL Materials* 5.9 (2017), p. 096101 (cit. on pp. 46, 47).
- [MKK+06] S. J. Moon, M. W. Kim, K. W. Kim, Y. S. Lee, J.-Y. Kim, J.-H. Park, B. J. Kim, S.-J. Oh, S. Nakatsuji, Y. Maeno, I. Nagai, S. I. Ikeda, G. Cao, T. W. Noh. In: *Phys. Rev. B* 74 (11 2006), p. 113104 (cit. on pp. 25, 53).
- [MLP+17] M. Minola, Y. Lu, Y. Y. Peng, G. Dellea, H. Gretarsson, M. W. Haverkort, Y. Ding, X. Sun, X. J. Zhou, D. C. Peets, L. Chauviere, P. Dosanjh, D. A. Bonn, R. Liang, A. Damascelli, M. Dantz, X. Lu, T. Schmitt, L. Braicovich, G. Ghiringhelli, B. Keimer, M. Le Tacon. In: *Phys. Rev. Lett.* 119 (9 Aug. 2017), p. 097001 (cit. on p. 91).
- [MMM99] Z. Q. Mao, Y. Mori, Y. Maeno. In: *Phys. Rev. B* 60 (1 July 1999), pp. 610–614 (cit. on p. 46).
- [MOY+16] J. Matsuno, N. Ogawa, K. Yasuda, F. Kagawa, W. Koshibae, N. Nagaosa, Y. Tokura, M. Kawasaki. In: *Sci. Adv.* 2.7 (2016) (cit. on pp. 76, 78, 79).
- [MP91] J. Maier, G. Pfundtner. In: *Advanced Materials* 3.6 (1991), pp. 292–297 (cit. on pp. 18, 20, 35, 39).
- [MSHM17] A. P. Mackenzie, T. Scaffidi, C. W. Hicks, Y. Maeno. In: *npj Quantum Materials* 2 (2017), p. 40 (cit. on p. 45).
- [MSV+08] S. J. May, A. B. Shah, S. G. E. te Velthuis, M. R. Fitzsimmons, J. M. Zuo, X. Zhai, J. N. Eckstein, S. D. Bader, A. Bhattacharya. In: *Phys. Rev. B* 77 (17 May 2008), p. 174409 (cit. on p. 69).
- [MSX+92] A. R. Moodenbaugh, R. L. Sabatini, Y. Xu, J. Ochab, J. G. Huber. In: *Physica C* 198 (1992), p. 103 (cit. on pp. 19, 92).
- [MTPF01] S. Maat, K. Takano, S. S. P. Parkin, E. E. Fullerton. In: *Phys. Rev. Lett.* 87 (2001), p. 087202 (cit. on p. 62).

- [MYD99] A. Moreo, S. Yunoki, E. Dagotto. In: *Science* 283.5410 (1999), pp. 2034–2040 (cit. on p. 85).
- [NLR+18] H. P. Nair, Y. Liu, J. P. Ruf, N. J. Schreiber, S.-L. Shang, D. J. Baek, B. H. Goodge, L. F. Kourkoutis, Z.-K. Liu, K. M. Shen, D. G. Schlom. In: *APL Materials* 6.4 (2018), p. 046101 (cit. on pp. 21, 22, 46, 78).
- [NMT17] H. Nobukane, T. Matsuyama, S. Tanda. In: *Sci. Rep.* 7 (2017), p. 41291 (cit. on p. 50).
- [NPB+09] A. Neubauer, C. Pfleiderer, B. Binz, A. Rosch, R. Ritz, P. G. Niklowitz, P. Böni. In: *Phys. Rev. Lett.* 102 (18 2009), p. 186602 (cit. on pp. 76, 80).
- [NRS+18] H. P. Nair, J. P. Ruf, N. J. Schreiber, L. Miao, M. L. Grandon, D. J. Baek, B. H. Goodge, J. P. C. Ruff, L. F. Kourkoutis, K. M. Shen, D. G. Schlom. In: *APL Materials* 6.10 (2018), p. 101108 (cit. on pp. 21, 22, 30, 32, 46, 48, 50).
- [NSO+10] N. Nagaosa, J. Sinova, S. Onoda, A. H. MacDonald, N. P. Ong. In: *Rev. Mod. Phys.* 82 (2 May 2010), pp. 1539–1592 (cit. on pp. 76, 79).
- [OM00] J. Orenstein, A. J. Millis. In: *Science* 288 (2000), p. 468 (cit. on p. 34).
- [OMO+18] Y. Ohuchi, J. Matsuno, N. Ogawa, Y. Kozuka, M. Uchida, Y. Tokura, M. Kawasaki. In: *Nat. Comm.* 9 (2018), p. 213 (cit. on pp. 76, 78, 79).
- [PAK+16] M.-H. Phan, J. Alonso, H. Khurshid, P. Lampen-Kelley, S. Chandra, K. S. Repa, Z. Nematy, R. Das, Ó. Iglesias, H. Srikanth. In: *Nanomaterials* 6 (2016), p. 221 (cit. on pp. 72, 74).
- [PDM+16] Y. Y. Peng, G. Dellea, M. Minola, M. Conni, A. Amorese, D. D. Castro, G. M. D. Luca, K. Kummer, M. Salluzzo, X. Sun, X. J. Zhou, G. Balestrino, M. L. Tacon, B. Keimer, L. Braicovich, N. B. Brookes, G. Ghiringhelli. In: *arXiv* 1609 (2016), p. 05405 (cit. on p. 35).
- [PDS+01] E. Pavarini, I. Dasgupta, T. Saha-Dasgupta, O. Jepsen, O. K. Andersen. In: *Phys. Rev. Lett.* 87 (2001), p. 047003 (cit. on p. 36).
- [PG10] J. Paglione, R. L. Greene. In: *Nat. Phys.* 6 (2010), p. 645 (cit. on p. 97).
- [PHS+09] D. C. Peets, D. G. Hawthorn, K. M. Shen, Y.-J. Kim, D. S. Ellis, H. Zhang, S. Komiya, Y. Ando, G. A. Sawatzky, R. Liang, D. A. Bonn, W. N. Hardy. In: *Phys. Rev. Lett.* 103 (8 Aug. 2009), p. 087402 (cit. on pp. 27, 92, 95).

- [PLC+] A. Pustogow, Y. Luo, A. Chronister, Y.-S. Su, D. A. Sokolov, F. Jerzembek, A. P. Mackenzie, C. W. Hicks, N. Kikugawa, S. Raghu, E. D. Bauer, S. E. Brown. In: *arxiv:1904.00047 (2019)* () (cit. on p. 45).
- [PNP+07] Z. V. Pchelkina, I. A. Nekrasov, T. Pruschke, A. Sekiyama, S. Suga, V. I. Anisimov, D. Vollhardt. In: *Phys. Rev. B* 75 (3 Jan. 2007), p. 035122 (cit. on pp. 25, 53).
- [PPDE16] J. P. Podkaminer, J. J. Patzner, B. A. Davidson, C. B. Eom. In: *APL Materials* 4.8 (2016), p. 086111 (cit. on p. 30).
- [QLL+19] Q. Qin, L. Liu, W. Lin, X. Shu, Q. Xie, Z. Lim, C. Li, S. He, G. M. Chow, J. Chen. In: *Adv. Mater.* 31.8 (2019), p. 1807008 (cit. on pp. 76, 79).
- [RAR+12] F. Radu, A. Abrudan, I. Radu, D. Schmitz, H. Zabel. In: *Nat. Commun.* 3 (2012), p. 715 (cit. on pp. 62, 63).
- [RBP06] U. K. Rößler, A. N. Bogdanov, C. Pfleiderer. In: *Nature* 442 (2006), p. 797 (cit. on p. 76).
- [RBP81] D. L. Rousseau, R. P. Bauman, S. P. S. Porto. In: *Journal of Raman Spectroscopy* 10.1 (1981), pp. 253–290 (cit. on p. 23).
- [RKS10] S. Raghu, S. A. Kivelson, D. J. Scalapino. “Superconductivity in the repulsive Hubbard model: An asymptotically exact weak-coupling solution.” In: *Phys. Rev. B* 81 (22 June 2010), p. 224505 (cit. on pp. 91, 97).
- [RUP+06] M. Reehuis, C. Ulrich, K. Prokeš, A. Gozar, G. Blumberg, S. Komiya, Y. Ando, P. Pattison, B. Keimer. In: *Phys. Rev. B* 73 (14 Apr. 2006), p. 144513 (cit. on pp. 73, 74).
- [SBC+19] A. Seo, A. V. Boris, G. Cristiani, H.-U. Habermeier, B. Keimer. In: *Phys. Rev. B* 99 (6 Feb. 2019), p. 064501 (cit. on p. 71).
- [SBDD15] H. Schraknepper, C. Bäumer, R. Dittmann, R. A. De Souza. In: *Phys. Chem. Chem. Phys.* 17 (2 2015), pp. 1060–1069 (cit. on pp. 46, 78).
- [SBG+16] H. Schraknepper, C. Bäumer, F. Gunkel, R. Dittmann, R. A. De Souza. In: *APL Materials* 4.12 (2016), p. 126109 (cit. on pp. 22, 46).
- [Sca12] D. J. Scalapino. In: *Rev. Mod. Phys.* 84 (4 Oct. 2012), pp. 1383–1417 (cit. on p. 91).

- [Sca19] D. J. Scalapino. In: *Proceedings of the National Academy of Sciences* 116.25 (2019), pp. 12129–12130 (cit. on pp. 94, 97).
- [SCB+96] M. Schmidt, T. R. Cummins, M. Bürk, D. H. Lu, N. Nücker, S. Schuppler, F. Lichtenberg. In: *Phys. Rev. B* 53 (22 June 1996), R14761–R14764 (cit. on p. 53).
- [SGI+19] H. Suzuki, H. Gretarsson, H. Ishikawa, K. Ueda, Z. Yang, H. Liu, H. Kim, D. Kukusta, A. Yaresko, M. Minola, J. A. Sears, S. Francoual, H.-C. Wille, J. Nuss, H. Takagi, B. J. Kim, G. Khaliullin, H. Yavaş, B. Keimer. In: *Nature Materials* 18 (6 June 2019), p. 563 (cit. on p. 24).
- [SJZ+16] Z. Shi, H.-Y. Jiang, S.-M. Zhou, Y.-L. Hou, Q.-L. Ye, M. Su Si. In: *AIP Advances* 6.1 (2016), p. 015101 (cit. on p. 85).
- [SKC+20] B. Sohn, B. Kim, J. W. Choi, S. H. Chang, J. H. Han, C. Kim. In: *Curr. Appl. Phys.* 20.1 (2020), pp. 186–190 (cit. on pp. 76, 79).
- [SKV+07] W. Siemons, G. Koster, A. Vailionis, H. Yamamoto, D. H. A. Blank, M. R. Beasley. In: *Phys. Rev. B* 76 (7 Aug. 2007), p. 075126 (cit. on pp. 22, 46, 78).
- [SNM+01] S. Sakita, S. Nimori, Z. Q. Mao, Y. Maeno, N. Ogita, M. Udagawa. In: *Phys. Rev. B* 63 (13 Mar. 2001), p. 134520 (cit. on pp. 55, 56).
- [SRF+87] L. C. Smedskjaer, J. L. Routbort, B. K. Flandermeyer, S. J. Rothman, D. G. Legnini, J. E. Baker. In: *Phys. Rev. B* 36 (1987), p. 3903 (cit. on p. 35).
- [SST+03] S. Sugai, H. Suzuki, Y. Takayanagi, T. Hosokawa, N. Hayamizu. In: *Phys. Rev. B* 68 (2003), p. 184504 (cit. on p. 38).
- [STNM00] H. Sato, A. Tsukada, M. Naito, A. Matsuda. In: *Phys. Rev. B* 61 (18 2000), pp. 12447–12456 (cit. on pp. 35, 36, 93, 94, 96).
- [Sug89] S. Sugai. In: *Phys. Rev. B* 39 (1989), p. 4306 (cit. on pp. 37, 38).
- [SUK+10] H. Sakakibara, H. Usui, K. Kuroki, R. Arita, H. Aoki. In: *Phys. Rev. Lett.* 105 (2010), p. 057003 (cit. on p. 36).
- [SUN05] G. Scholten, K. D. Usadel, U. Nowak. In: *Phys. Rev. B* 71 (6 Feb. 2005), p. 064413 (cit. on p. 72).

- [SZB+17] A. Steppke, L. Zhao, M. E. Barber, T. Scaffidi, F. Jerzembeck, H. Rosner, A. S. Gibbs, Y. Maeno, S. H. Simon, A. P. Mackenzie, C. W. Hicks. In: *Science* 355 (2017) (cit. on p. 45).
- [Tin04] M. Tinkham. *Introduction to superconductivity, 2nd ed.* Dover, 2004 (cit. on p. 92).
- [TIU+89] H. Takagi, S. Ido, T. ansd Ishibashi, M. Uota, S. Uchida, Y. Tokura. In: *Phys. Rev. B* 40 (4 Aug. 1989), pp. 2254–2261 (cit. on p. 96).
- [TL17] R. Takahashi, M. Lippmaa. In: *ACS Appl. Mater. Interfaces* 9.25 (2017), pp. 21314–21321 (cit. on p. 46).
- [TSNE00] F. Tsui, M. C. Smoak, T. K. Nath, C. B. Eom. In: *Appl. Phys. Lett.* 76.17 (2000), pp. 2421–2423 (cit. on p. 70).
- [TTN+88] J. B. Torrance, Y. Tokura, A. I. Nazzal, A. Bezing, T. C. Huang, S. S. P. Parkin. In: *Phys. Rev. Lett.* 61 (9 Aug. 1988), pp. 1127–1130 (cit. on pp. 20, 35).
- [TYM+94] I. Tanaka, J. Yamamoto, Y. Mori, H. Tanabe, M. K. R. Khan, H. Kojima. In: *Physica C* 225 (1994), p. 185 (cit. on pp. 19, 92).
- [UDS+14] M. A. Uribe-Laverde, S. Das, K. Sen, I. Marozau, E. Perret, A. Alberca, J. Heidler, C. Piamonteze, M. Merz, P. Nagel, S. Schuppler, D. Munzar, C. Bernhard. In: *Phys. Rev. B* 90 (2014), p. 205135 (cit. on pp. 68, 72).
- [UIT+91] S. Uchida, T. Ido, H. Takagi, T. Arima, Y. Tokura, S. Tajima. In: *Phys. Rev. B* 43 (10 Apr. 1991), pp. 7942–7954 (cit. on p. 95).
- [UIW+17] M. Uchida, M. Ide, H. Watanabe, K. S. Takahashi, Y. Tokura, M. Kawasaki. In: *APL Materials* 5.10 (2017), p. 106108 (cit. on pp. 30, 46, 47).
- [VDG20] T. Valla, I. K. Drozdov, G. D. Gu. In: *Nat. Comms.* 11 (2020), p. 569 (cit. on p. 91).
- [VSR+14] I. I. Vlasov, A. A. Shiryayev, T. Rendler, S. Steinert, S.-Y. Lee, D. Antonov, M. Vörös, F. Jelezko, A. V. Fisenko, L. F. Semjonova, J. Biskupek, U. Kaiser, O. I. Lebedev, I. Sildos, P. R. Hemmer, V. I. Konov, A. Gali, J. Wrachtrup. In: *Nat. Nanotech.* 9 (2014), p. 54 (cit. on p. 13).

- [VWS+19] L. Vistoli, W. Wang, A. Sander, Q. Zhu, B. Casals, R. Cichelero, A. Barthélémy, S. Fusil, G. Herranz, S. Valencia, R. Abrudan, E. Weschke, K. Nakazawa, H. Kohno, J. Santamaria, W. Wu, V. Garcia, M. Bibes. In: *Nature Physics* 15 (1 2019), p. 67 (cit. on pp. 76, 86).
- [VZR+14] C. N. Veenstra, Z.-H. Zhu, M. Raichle, B. M. Ludbrook, A. Nicolaou, B. Slomski, G. Landolt, S. Kittaka, Y. Maeno, J. H. Dil, I. S. Elfimov, M. W. Haverkort, A. Damascelli. In: *Phys. Rev. Lett.* 112 (12 Mar. 2014), p. 127002 (cit. on p. 25).
- [WAN+16] H. I. Wei, C. Adamo, E. A. Nowadnick, E. B. Lochocki, S. Chattejee, J. P. Ruf, M. R. Beasley, D. G. Schlom, K. M. Shen. In: *Phys. Rev. Lett.* 117 (2016), p. 147002 (cit. on p. 44).
- [WBHB17] J. Wu, A. T. Bollinger, X. He, Božović. In: *Nature* 547 (July 2017), p. 432 (cit. on p. 92).
- [WCY+10] S. M. Wu, S. A. Cybart, P. Yu, M. D. Rossell, J. X. Zhang, R. Ramesh, R. C. Dynes. In: *Nat. Mater.* 9 (2010), p. 756 (cit. on p. 64).
- [WDL+19] W. Wang, M. W. Daniels, Z. Liao, Y. Zhao, J. Wang, G. Koster, G. Rijnders, C.-Z. Chang, D. Xiao, W. Wu. In: *Nat. Mater.* 18 (2019), p. 1054 (cit. on p. 76).
- [WFK+18] L. Wang, Q. Feng, Y. Kim, R. Kim, K. H. Lee, S. D. Pollard, Y. J. Shin, H. Zhou, W. Peng, D. Lee, W. Meng, H. Yang, J. H. Han, M. Kim, Q. Lu, T. W. Noh. In: *Nat. Mater.* 17 (2018), p. 1087 (cit. on pp. 76, 79, 86).
- [WGW+18] F. Wrobel, B. Geisler, Y. Wang, G. Christiani, G. Logvenov, M. Bluschke, E. Schierle, P. A. van Aken, B. Keimer, R. Pentcheva, E. Benckiser. In: *Phys. Rev. Mater.* 2 (2018), p. 035001 (cit. on p. 68).
- [WHK10] C. Weber, K. Haule, G. Kotliar. In: *Phys. Rev. B* 82 (12 Sept. 2010), p. 125107 (cit. on pp. 36, 95).
- [WIK+15] S. Wakimoto, K. Ishii, H. Kimura, M. Fujita, G. Dellea, K. Kummer, L. Braicovich, G. Ghiringhelli, L. M. Debeer-Schmitt, G. E. Granroth. In: *Phys. Rev. B* 91 (18 May 2015), p. 184513 (cit. on pp. 91, 92).
- [WL11] F. Wang, D.-H. Lee. In: *Science* 332.6026 (2011), pp. 200–204 (cit. on p. 97).
- [WPW+88] W. H. Weber, C. R. Peters, B. M. Wanklyn, C. Chen, B. E. Watts. In: *Solid State Comm.* 68 (1988), pp. 61–65 (cit. on p. 37).

- [WZY+04] S. Wakimoto, H. Zhang, K. Yamada, I. Swainson, H. Kim, R. J. Birgeneau. In: *Phys. Rev. Lett.* 92 (21 May 2004), p. 217004 (cit. on p. 91).
- [XZL+10] W. J. Xu, B. Zhang, Z. X. Liu, Z. Wang, W. Li, Z. B. Wu, R. H. Yu, X. X. Zhang. In: *EPL (Europhysics Letters)* 90.2 (Apr. 2010), p. 27004 (cit. on p. 85).
- [YGA+12] F. Yang, M. Gu, E. Arenholz, N. D. Browning, Y. Takamura. In: *J. Appl. Phys.* 111.1 (2012), p. 013911 (cit. on p. 70).
- [YLO+10] P. Yu, J.-S. Lee, S. Okamoto, M. D. Rossell, M. Huijben, C.-H. Yang, Q. He, J. X. Zhang, S. Y. Yang, M. J. Lee, Q. M. Ramasse, R. Erni, Y.-H. Chu, D. A. Arena, C.-C. Kao, L. W. Martin, R. Ramesh. In: *Phys. Rev. Lett.* 105 (2 July 2010), p. 027201 (cit. on pp. 64, 86).
- [YZT+15] W. Yuan, Y. Zhao, C. Tang, T. Su, Q. Song, J. Shi, W. Han. In: *Appl. Phys. Lett.* 107.2 (2015), p. 022404 (cit. on p. 69).
- [ZBEL19] M. Ziese, F. Bern, P. D. Esquinazi, I. Lindfors-Vrejoiu. In: *Phys. Status Solidi B*, 1900628 (2019) (cit. on pp. 76, 79).
- [ZDB+20] P. Zhang, A. Das, E. Barts, M. Azhar, K. Held, M. Mostovoy, T. Banerjee. In: *arXiv:2001.07039* (2020) (cit. on pp. 76, 79).
- [ZGDM17] P. Zilske, D. Graulich, M. Dunz, M. Meinert. In: *Appl. Phys. Lett.* 110 (2017), p. 192402 (cit. on p. 62).
- [ZK16] W. Zhang, K. M. Krishnan. In: *Mater. Sci. Eng. R* 105 (2016), p. 1 (cit. on p. 62).
- [ZR88] F. C. Zhang, T. M. Rice. In: *Phys. Rev. B* 37 (7 Mar. 1988), pp. 3759–3761 (cit. on pp. 27, 94).
- [ZSA85] J. Zaanen, G. A. Sawatzky, J. W. Allen. In: *Phys. Rev. Lett.* 55 (4 July 1985), pp. 418–421 (cit. on pp. 26, 94).
- [ZSR+19] Z. H. Zhu, J. Stremper, R. R. Rao, C. A. Occhialini, J. Pellicciari, Y. Choi, T. Kawaguchi, H. You, J. F. Mitchell, Y. Shao-Horn, R. Comin. In: *Phys. Rev. Lett.* 122 (1 Jan. 2019), p. 017202 (cit. on p. 24).

ACKNOWLEDGEMENTS

First of all, I want to thank my doctoral supervisor, Bernhard Keimer, who became my academic role model. Every interaction with him was a learning moment for me, and I appreciate his support and kindness. I would like to thank members of thin film technology group, Gennady Logvenov, Georg Christiani, Peter Specht, Birgit Lemke, Stephan Schmid, Benjamin Stuhlhofer, Yvonne Stuhlhofer, Petar Yordanov, and Hanns-Ulrich Habermeier for all the technical supports and being my second family. I couldn't survive PhD without their supports. In team MBE, Gennady, Georg and Peter, have taught me literally everyday as day-to-day advisors and also as good friends. Whenever I hit a wall, I could run to Gennady and get advises from him. Without Georg's design of the sputtering chamber and samples holders, this thesis would not have been possible. Peter taught me all about the MBE chamber and vacuum technology.

I thank all members of professor Keimer's department. I sincerely thank Daniel Putzky for many adventures we had attending conferences and for the many drivings for the group activities. I owe Padma Radhakrishnan countless discussions and English corrections. Ksenia Rabinovich made a great contribution to the spectroscopic ellipsometry measurements of LCCO samples. Thanks to the members of TB GmbH: Yury Khaydukov and Laura Guasco for fruitful collaborations, with whom I had many scientific and

non-scientific discussions during numerous beamtimes together. I thank Thomas Keller for the excellent beamline NREX at FRM-II, where I had many PNR beamtimes. I thank Christopher Dietl for all the discussions as a friendly office mate and a professional beamtime mate. Thanks to Katrin Fürsich for being helpful and kind in research and in daily matters, and to Martin Bluschke for teaching and helping me during my first XMCD beamtime at BESSY. I thank Alexander Boris and David Dawson, for many stimulating discussions about the optical responses of superconducting thin films. Matteo Minola gave me many scientific comments on my manuscripts and warm encouragement. I appreciate his patience with my writing. I thank Hun-Ho Kim for teaching me Raman spectroscopy, and Sungkyun Choi for giving me opportunity to do neutron diffraction experiments at ISIS neutron source. I thank Hakuto Suzuki, Hlynur Grettarson and Joel Bertinshaw for the kind explanations during the RIXS beamtime at DESY, Toshinao Loew, and Matthias Hepting for many fruitful discussions, Peter Wochner for his support during beamtimes at ANKA. Although I didn't have a chance to collaborate with some of the group members, I thank Eva Benckiser, Bum Joon Kim, Yi Lu, Timofei Larkin, Roberto Ortiz, Juan Porras, Heiko Trepka, Huimei Liu, Giniyat Khaliullin, Suguru Nakata, Maximilian Krautloher, Jorge Saucedo, Cissy Suen, Valentin Zimmermann, Davide Betto, Lichen Wang, Zichen Yang, Xiao Tong Shi, Hoon Kim, Rebecca Pons for providing the friendly and stimulating environment for research. I thank Sonja Balkema, Benjamin Bruha, Manfred Ohl, Armin Schulz and Michael Schulz for their administrative and technical supports.

I had great opportunities to have collaborations in and out of MPI. I want to thank Y. Eren Suyolcu, Yu-Mi Wu and Peter van Aken for many STEM images of my samples, which made many of my papers stronger. Eren made enormous contribution to my thesis with amazing images and numerous discussions. I would like to thank Kwanghyo Son for teaching me SQUID magnetometry of thin films. I had fruitful collaborations with Parmida Shabestari, Minjae Kim, Hao Chu, Stefan Kaiser and Domenico Paone, in which I could learn new techniques such as ultrafast spectroscopy and ODMR. I am grateful to Darrell Schlom at Cornell University for providing me

excellent MBE samples, and for inviting me to PARADIM workshop, where I found another opportunity to collaborate with his group. I thank J. Steve Dodge at Simon Fraser University for inviting me to his lab in Canada.

Last but not least, I would like to express my deepest gratitude to my family in Korea, who has given me unconditional love and support. I am indebted to my wife, Seonghye Cheon, for her love, patience and trust in me.